# BAND-EDGE OPTICAL PROPERTIES OF GaInNAs(Sb) AND THE RELATION TO ATOMIC STRUCTURE

A DISSERTATION
SUBMITTED TO THE DEPARTMENT OF MATERIALS SCIENCE AND ENGINEERING
AND THE COMMITTEE ON GRADUATE STUDIES
OF STANFORD UNIVERSITY
IN PARTIAL FULFILLMENT OF THE REQUIREMENTS
FOR THE DEGREE OF
DOCTOR OF PHILOSOPHY

Vincenzo Lordi

December 2004

I certify that I have read this dissertation and that, in my opinion, it is fully adequate in scope and quality as a dissertation for the degree of Doctor of Philosophy.

James S. Harris
(Principal Adviser)

I certify that I have read this dissertation and that, in my opinion, it is fully adequate in scope and quality as a dissertation for the degree of Doctor of Philosophy.

David A. B. Miller

I certify that I have read this dissertation and that, in my opinion, it is fully adequate in scope and quality as a dissertation for the degree of Doctor of Philosophy.

Mark L. Brongersma

Approved for the University Committee on Graduate Studies.

# Abstract

The GaInNAs(Sb) material system provides a promising solution for realizing low-cost lasers, detectors, and optical modulators operating in the telecommunications wavelength range of 1300–1600 nm, by fabricating these devices on GaAs substrates. These devices are important not only for addressing current bottlenecks in the "last mile" of optical fiber communication networks, but also for enabling optical interconnect technology to replace electrical lines limiting the future speed of microelectronics. The design of optical interconnects operating in the telecommunications wavelength range allows for low voltage operation as well as seamless integration with optical networking.

The addition of small concentrations ($< 2$ at%) of N to Ga(In)As to form semiconductor alloys with band gaps below that of GaAs is an anomalous characteristic, considering the larger band gap of the binary Group III-nitrides compared to the binary Group III-arsenides. The nature of this sharp band gap lowering and other interesting properties of the band-edge optical transitions, which are found to be dominated by N-related states, are elucidated using a combination of first principles calculations and various experiments. A relationship between variations in local atomic structure and the band-edge optical properties is developed.

Another unique characteristic of these materials is that the luminescent quality of the as-grown material is generally poor, although it is improved 20–100$\times$ by *ex situ* rapid thermal annealing. However, the improvement in luminescence intensity is

accompanied by an undesirable blueshift of the wavelength by up to 100 nm, which is unacceptable for reproducible control of the operating wavelength of devices using these materials in the active region. The mechanism of this blueshift is also shown to depend on the relationship between local atomic structure and changes in the band-edge optical states.

X-ray absorption, electroreflectance, and photoluminescence spectroscopies are used to study a series of transitions near the apparent band edge of GaInNAs(Sb) materials that correspond to different N nearest neighbor configurations. These band-edge states are found to be a dominant contribution to the band gap blueshift upon annealing. As-grown material contains a random distribution of bonds, which is dominated by N–Ga nearest neighbors, corresponding to a smaller band gap. Annealing shifts the distribution of bonds toward increased N–In nearest neighbors and a configuration with a larger band gap that is also more thermodynamically stable. The annealing-induced blueshift of the band gap saturates after the material has reached equilibrium, as expected, although the luminescent quality of the material can continue to be increased.

Additionally, the electroabsorption properties of GaInNAs(Sb) quantum wells (QWs) are measured by photocurrent to determine their suitability for use in optical modulators. Spectra taken at room temperature demonstrate very nice quantum confined Stark effect behavior, with sharp exciton peaks having full-width at half-maximum less than 25 meV. The peak absorption coefficient of fully annealed GaInNAsSb QWs was measured to be close to 35,000 $cm^{-1}$ at 1525 nm wavelength, a value higher than reported for competing materials, while annealed GaInNAs QWs showed peak absorption of $\sim$18,000 $cm^{-1}$ at 1250 nm. Analogous to the material's luminescent behavior, thermal annealing was found to increase the absorption coefficient of the QWs while blueshifting the band gap. The increase in absorption coefficient is mainly caused by increased oscillator strength of the band edge transition, related to

the atomic reconfiguration described above.

Furthermore, the measured electroabsorption characteristics indicate that optical modulators using GaInNAs(Sb) QWs can be fabricated throughout the 1300–1600 nm wavelength range with performance comparable or superior to current technology using competing materials grown on InP substrates. We predict device performance for an asymmetric Fabry-Perot reflection modulator using GaInNAs(Sb) QWs of up to 15–20 dB modulation ratio over a 15–20 nm optical bandwidth, using less than a 3 V swing. A design for such a modulator operating at 1550 nm is presented. GaInNAs(Sb)-based modulators have great potential to address the current bottlenecks in telecommunication and optical interconnect applications described above, by providing a low-cost, two-dimensionally arrayable solution.

# Acknowledgments

This dissertation would not be possible without the support, motivation, guidance, and encouragement of my research advisor Professor James Harris. His technical and scientific knowledge is impressive, and he possesses a remarkable sense of the technology choices that will be practical and useful. I am indebted to him not only for helping me to develop academically and scientifically, but also for providing real life advice as well as a connection to the rest of the scientific community.

I would also like to thank the members of my reading committee, Professors David Miller and Mark Brongersma, as well as the members of my oral defense committee, Professors Bruce Clemens and Kyeongjae (KJ) Cho. Their feedback was indispensable in getting my ideas focused and understanding the larger issues surrounding my work. Professor KJ Cho, who served as the Chair of my oral defense committee, also provided significant guidance for the computational portion of my dissertation. Deep appreciation is further due to Gail Chun-Creech, for providing administrative support.

Various students in the Harris group receive my gratitude for their contributions to my work. Homan Yuen, Seth Bank, Mark Wistey, and former students Vincent Gambin and Wonill Ha have made tremendous advancements in the MBE growth of GaInNAs(Sb) materials, and I thank them for providing high quality samples, as well as the opportunity for excellent discussions. Seth further contributed to some of the temperature-dependent photoluminescence experiments. I am grateful to Evan

Thrush, Rafael Aldaz, and Mike Wiemer for teaching me about GaAs device processing. Vijit Sabnis also contributed significant knowledge about device processing and device physics. Many excellent discussions with Glenn Solomon helped to fully crystallize various ideas in my mind and to discover how best to convey them. I also appreciate many helpful discussions with Lynford Goddard, who further introduced me to LabVIEW when I began writing the automation software for my measurement setups. Reflectivity measurements were performed with the help of David Jackrel. I would like to thank all of the members of the Harris group for making my time at Stanford enjoyable.

Many other contributors need to be acknowledged. Stephan Friedrich and Tobias Funk of the Advanced Light Source at Lawrence Berkeley National Lab were instrumental in obtaining the x-ray absorption data. Toshiyuki Takizawa, Kazuyuki Uno, Masako Yamada, Ichiro Tanaka, Tomoyo Uruga, and Satoshi Komiya provided complementary x-ray absorption data from SPring-8 in Japan. Professor Pierro Pianetta provided helpful suggestions and feedback regarding surface analysis techniques and interpretation of x-ray absorption data. I am also indebted to Sean Brennan of the Stanford Synchrotron Radiation Lab for helping with synchrotron x-ray diffraction experiments. Nan Yao of Princeton University provided guidance in studies using TEM and EELS (which are excluded from this dissertation), in addition to cultivating my research skills as my advisor while an undergraduate at Princeton.

I would like to thank the Fannie and John Hertz Foundation for providing me with a graduate Fellowship during my time at Stanford. As a Hertz Fellow, I was given the freedom to pursue research that excited me. Further research funding was provided by DARPA/ONR through the Optoelectronics Materials Center, and also by the MARCO program, the Stanford Photonics Research Center, and the Stanford Network Research Center. Supercomputing time at the San Diego Supercomputer Center and the Texas Advanced Computing Center was provided by a grant from the

National Partnership for Advanced Computational Infrastructure.

The most important person I would like to thank is my wife, Vanessa, who supported me without complaint throughout my work. She was especially gracious during the time spent writing this dissertation, which essentially took over my life for a while. She was instrumental in keeping me sane, providing laughter and inspiration, and simply making my life enjoyable. I thank my parents for encouraging me to follow my dreams and allowing me the opportunities to fulfill them. My sister, Rosa, provided much encouragement to me as well.

# Dedication

*This dissertation is dedicated to my lovely wife Vanessa.*

# Table of Contents

# List of Tables

# List of Figures

# Chapter 1

# Introduction

## 1.1 Motivation

The astonishing growth of the Internet and data transmission volume in recent years is resulting in increased bandwidth requirements for fiber-optic networks, especially at the metro-area (MAN), local-area (LAN) and storage area (SAN) levels. Despite the "bursting of the dot-com and telecommunications technology bubble" early in this decade, network traffic has increased unimpeded, approximately doubling every year since 1997 and continuing at a similar rate [1]. Current long-haul systems, using expensive optoelectronic components and (dense) wavelength division multiplexing [(D)WDM], appear to possess sufficient capacity to accommodate the increased aggregate traffic, and (expensive) solutions exist to extend that capability for most of the foreseeable future. Cost is not a significant factor for the long-haul market which requires in total only on the order of a few tens of thousand optoelectronic devices. However, the current throughput bottleneck of optical networks lies at the edges, in the so-called "last mile," where the high-speed long-haul line is divided into branches for each of the many individual subscribers (from entire buildings in a city to individual residences) [2–4]. To extend the high-speed capability of the long-haul network through the "last mile" requires tens to hundreds of millions of

high-performance optoelectronic devices, which not only are cost-effective to deploy but also are cost-effective to place in consumer products. The lack of such low-cost, high-speed components to address the needs of the MAN and LAN market currently limits the network throughput for the end user. In the best case, data rates on the order of 10 Mb/sec are obtainable, but more typical rates are ∼1–5 Mb/sec. By overcoming the "last mile" bottleneck with ubiquitous fiber optic networking at the MAN and LAN level, routine data rates of 1–10 Gb/sec or higher would be realized, and fuller utilization of the THz capability of long-haul fiber optic links would result. In such a scenario, end user throughput may more likely be limited by processor speed or perhaps the performance of individual optoelectronic components in the LAN, rather than the network bandwidth.

The presently available optoelectronic components used in the long-haul optical network, where cost is secondary to performance, are prohibitively expensive for use at the edges of the network for several reasons. The predominant semiconductor material used in those devices is InGaAsP, which is lattice matched to InP and has a band gap near the required operating wavelength of ∼1550 nm. This wavelength requirement is dictated by the transmission properties of optical fiber, which has minimum loss near 1550 nm. In general, taking into consideration the loss and dispersion characteristics of modern optical fiber and varying requirements of transmission distance for different applications, devices operating throughout the 1300–1600 nm wavelength range are desirable. Until recently, the InGaAsP material system was the only practical direct-gap semiconductor with the appropriate band gap. Several problems exist with this material system that lead to the high cost of devices. First of all, the use of InP substrates inflates the cost, because wafers are smaller (2–4× by area) and more expensive (2–5×) compared to GaAs substrates. In addition, device yield per wafer is generally lower due to the difficulty of device processing and the brittleness of the wafer. More significant, though, is the high temperature-sensitivity

of devices based on InGaAsP, due to a low conduction band offset with InP. Since tight wavelength stability is required for source lasers due to the use of wavelength division multiplexing (WDM) and dense WDM (DWDM), expensive thermoelectric cooling systems often dominate the cost of individual components. Furthermore, the lack of a convenient way to integrate highly reflecting mirror structures on InP and the need for high-power, chirp-free sources in the long-haul network lead to the use of edge-emitting lasers, as opposed to vertical-cavity lasers. Edge-emitting lasers are inherently more expensive than vertical-cavity lasers (VCSELs) due to nonideal fabrication and testing requirements. The physically large size of the edge-emitting laser results in fewer devices produced per wafer and increased material cost. Testing is expensive because each device needs to be cleaved and tested individually. A wafer-level automated testing scheme, as used in VCSEL production, is not feasible for edge-emitters. Finally, the packaging costs are high since precision fiber pig-tailing is required to couple the laser's small, asymmetric mode into the circular mode of optical fiber.

A new material system to compete with InGaAsP might overcome these limitations and lead to inexpensive components suitable for the high-volume, shorter distance LAN/MAN/SAN market, perhaps with somewhat relaxed technical requirements (coarse or no WDM, shorter transmission distance, lower speed). A material system that allows monolithic integration of multiple components on a single-chip would further reduce costs and increase performance in the "last mile" portion of the network.

Another technological area with an analogous bottleneck problem is microprocessing. State-of-the-art integrated circuits fabricated presently, and certainly over the next few years, suffer from a bottleneck due to relatively slow backend electrical interconnects, as well as chip-to-chip and board-to-board interconnects. While transistor scaling continues to follow Moore's Law, doubling the density (and increasing

the speed) approximately every 18 months, metal interconnects scale with an inverse performance relationship due to increased resistance with shrinking cross section and cannot follow the same aggressive trend. The critical factor is the RC delay introduced by the dense array of metal lines on the chip which increases approximately linearly as the size is reduced, if no other changes are made to reduce the resistivity or capacitance per unit length. In fact, line resistance has reached a sort of "end of the road" with the introduction of Cu metal and will only increase as cross-sections are made smaller. The capacitance between lines can only be reduced significantly through the use of low-$k$ dielectric materials, but these have limited potential since less than an order of magnitude reduction can be achieved by switching to an air dielectric, which is the limiting case. Without changing the interlayer dielectric material, the capacitance between lines will remain nearly constant with decreased spacing offset by reduced area. Judicious designs for routing the electrical interconnects can lessen the problem, but cannot really improve the situation. Thus, despite constant improvements in transistor performance, severe constraints are imposed on overall microprocessor speed by the delay times of the electrical lines connecting the transistors together. Another issue with dense electrical lines that limit the maximum operating speed is the strong frequency dependence of loss and cross-talk between the metal lines [5]. At the board level and above, line resistance is not an issue, since thick traces are used. However, the low impedance of these lines and their considerable capacitance results in the need for high drive currents, and consequently a large power requirement.

Employing optical interconnects, essentially very short segments of an optical network, as a replacement for some of the electrical interconnects in and between integrated circuits can remove the bottleneck, by introducing very fast, cross-talk-free links [5–7]. An additional advantage of using optics for interconnects is that very short pulses can be utilized (ps or shorter using mode-locked lasers) to deliver a very high degree of signal synchronization at high speeds and also remove skew from electrical

signals. Furthermore, optics fundamentally solves the problem of impedance matching between the high-impedance active devices in the circuit and the low-impedance electrical lines [5].

Optical interconnects may be introduced at a variety of length scales. The largest length scale, excluding the LAN, is board-to-board communication or communication on a backplane, where optics provides a power advantage. The next level would involve bringing optics onto and between individual chips on a board. At this shorter length scale, optics does not provide a clear power advantage if directly modulated lasers are employed. However, if the laser source is taken off-chip and arrays of low-power, reverse-biased optical modulators instead form the optical interconnect system, the power advantage of optics can be extended down to the sub-millimeter length scale [8, 9]. Ultimately, we can also imagine optical signals traveling between regions on an individual chip. At the chip level, we can envision the use of integrated optoelectronics (lasers, modulators, detectors, waveguides) that may be tightly integrated with the transistor layout. At this smallest level, overcoming the RC delays of electrical lines is paramount.

However, similar to the "last-mile" problem in communications networks, using optics for interconnect applications requires a massively large volume of devices costing a fraction of a cent, precluding the use of existing technology. Again, we find a need for a new material system that will enable these advances.

The choice of operating wavelength(s) for optical interconnects is less restrictive than for telecommunications, however, choosing longer wavelengths has an advantage since the operating voltage for devices generally scales with the band gap. To remain compatible with the CMOS supply voltage, which is approaching 1 V, the use of wavelengths longer than 1240 nm is suggested. Operating at 1550 nm might be convenient for eventually "bringing the network to the chip," in essence combining microprocessing and networking functions seamlessly through the optical network.

Such an integrated architecture would enable unprecedented capabilities for remote computing and remote sharing, and also open the door for large-scale, widespread distributed computing. A new paradigm in computing, where the network truly *is* the computer, would likely emerge.

Furthermore, the use of external optical modulators to switch a continuous-wave laser beam, as opposed to directly modulating lasers to create the optical signal, has advantages for both telecommunication and optical interconnect applications. For very high-speed optical communications systems, direct modulation of the laser source is often not feasible or practical due to issues with chirp and wavelength drift caused by the thermal effects of switching the laser on and off. The use of an external modulator which decouples the high-speed electrical circuit from the laser drive circuit drastically reduces chirp and essentially eliminates wavelength drift. For optical interconnects at an intermediate length scale, the advantage is in a low power requirement compared to driving an array of laser diodes.

## 1.2 Background on the GaInNAs(Sb) Material System

The GaInNAs(Sb) material system offers the potential to overcome many of the limitations of InGaAsP and enable the fabrication of low-cost optoelectronic components operating in the 1300–1600 nm wavelength region to address the bottlenecks in current optical networks and microprocessors discussed above [2, 3]. Ten years ago, there did not seem to be a semiconductor with an appropriate direct band gap, other than InGaAsP, that could be grown epitaxially, with high quality, on available substrates. This is illustrated in Fig. 1.1, where the alloy line of InGaAsP passes through the demarcated band gap region of interest and also is lattice matched to InP. However,

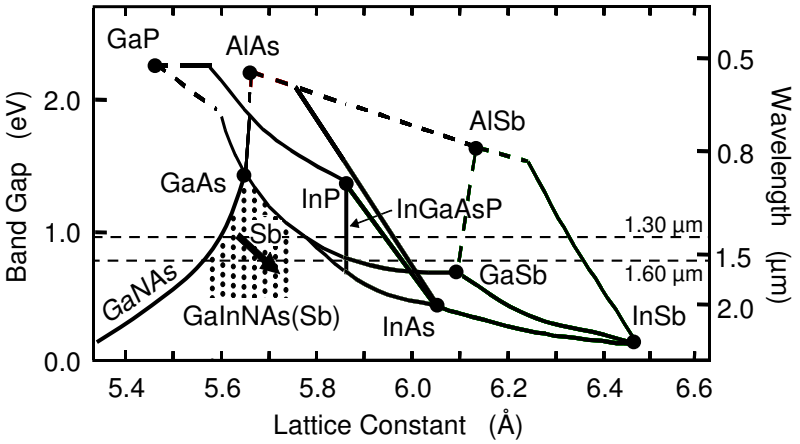


Figure 1.1: The working space of III-V semiconductors, plotted as band gap *vs.* lattice constant. Either InGaAs(P) on InP or GaInNAs(Sb) on GaAs are logical choices to achieve operation in the desired wavelength range of 1300–1600 nm. The shaded region indicates the working space for the GaInNAs(Sb) alloy.

in 1994, Kondow *et al.* discovered that adding small amounts of N to GaAs has the remarkable and completely unexpected effect of sharply lowering the band gap, despite the larger band gap of GaN compared to GaAs [10]. The further addition of In created an alloy ($Ga_{1-x}In_xN_yAs_{1-y}$) whose band gap and lattice constant could be varied nearly independently [11]. The band gap could be lowered monotonically while remaining (nearly) lattice matched to GaAs, since both N and In lower the band gap but have opposite effects on the lattice constant. This is also shown in Fig. 1.1.

Limits on the degrees of freedom of band gap and lattice constant in GaInNAs arise from the low solid solubility of N in the alloy and also a general degradation of material quality with the incorporation of greater amounts of N [12]. Achieving very long wavelengths up to 1600 nm requires excessive In content, which increases the lattice constant too much above that of the GaAs substrate, precluding high-quality epitaxy. In practice, the longest achievable wavelength with GaInNAs has been ∼1400 nm and many devices, particularly lasers, have been demonstrated operating around 1300 nm

[2, 13]. Typical compositions of $Ga_{1-x}In_xN_yAs_{1-y}$ to achieve these wavelengths and remain closely lattice matched to GaAs are $x \sim 0.2$–$0.4$ and $y \sim 0.01$–$0.03$.

Over the past few years, the incorporation of a few percent of Sb into the alloy (creating $Ga_{1-x}In_xN_yAs_{1-y-z}Sb_z$) has allowed further reduction of the band gap up to 1600 nm [14–18]. Evidence suggests that incorporation of Sb into the alloy also improves the optical quality of material at shorter wavelengths, perhaps by requiring less N [19]. Additionally, Sb has a surfactant effect during growth, suppressing phase segregation and surface roughening [20, 21]. This offsets the increased lattice mismatch introduced by the large Sb atom and has allowed the growth of high quality material on GaAs. Our group has demonstrated high-performance device characteristics using GaInNAsSb for wavelengths spanning the 1300–1600 nm range [14, 22–24].

The addition of In, N, or Sb to GaAs all reduce the band gap, but have different effects on the band structure, manifested in the very different band offsets with GaAs that result. Indium nearly equally effects the energies of the conduction band edge and valence band edge, with a 70% offset in the conduction band. In contrast, the effect of N is almost exclusively in lowering the conduction band edge, while Sb affects essentially only the valence band edge [25–27]. For usual compositions of GaInNAs near 1300 nm emission, the band discontinuity is typically ∼80% in the conduction band [28]. However, careful alloying of $Ga_{1-x}In_xN_yAs_{1-y-z}Sb_z$ allows some further degree of freedom in engineering the band offsets with GaAs, in addition to the band gap. (However, there may be evidence suggesting that in the quinary alloy, Sb does not affect the valence band as strongly as in GaAsSb [29].)

The advantages of the GaInNAs(Sb) material system over InGaAsP to address the issues discussed in Section 1.1 stem from its ability to be grown on GaAs substrates. At a basic level, GaAs substrates are available larger (2–4× by area) and for lower cost (2–5×) than InP substrates, and the reduced brittleness increases yield. This leads directly to almost one order of magnitude in potential savings for material costs,

however, that alone is insufficient to enable the required high volumes, which are over 4 orders of magnitude above current production of telecommunications devices. Further cost-effectiveness is gained by the better-developed processing technology on GaAs, which allows easier integration of high-speed electronics with photonic devices. The most significant advantage of working on a GaAs substrate, however, is the possibility of monolithic integration of highly-reflective distributed Bragg reflectors (DBRs) using lattice-matched AlGaAs, enabling the fabrication of low-cost vertical cavity lasers as well as resonant cavity detectors and modulators. Such devices, which operate normal to the wafer surface, are important for high-performance, scalable optical interconnects and inexpensive telecommunications lasers. They can be made extremely inexpensively due to their small size and simple testing. Furthermore, the vertical configuration of these devices promotes more uniform optical mode profiles that simplify input/output coupling, eliminate polarization sensitivity, and facilitate the construction of two-dimensional arrays. For optical interconnect applications, VCSELs are a good candidate for a direct-modulation implementation and should be able to achieve bandwidths up to 15 GHz, although electrical interconnects can probably remain competitive up to nearly those speeds. To push the performance limit of optical interconnects, an implementation using an external laser source and on-chip modulators can be used that also better addresses the power issue as discussed in Section 1.1.

In addition to the advantages of working on a GaAs substrate, inherent material advantages are expected for GaInNAs(Sb) devices over InGaAsP. Lower temperature sensitivity results from a large conduction band offset with the quantum well barrier material (GaAs or GaNAs) and a heavy electron effective mass, preventing electrons from being thermally excited out of the wells. A higher differential gain for lasing has also been measured. This thesis will expand on details of some of these advantages, and also demonstrate a very high band-edge absorption coefficient for these materials

due to the heavy electron effective mass.

Along with the intrinsic advantages of the GaInNAs(Sb) material system and the benefits of working on GaAs substrates come a range of difficulties as well. Fundamentally, the low solid solubility of N in the alloy due to the large size mismatch of the atoms, combined with a tendency to phase segregate at high temperatures, requires low-temperature, metastable growth. A good deal of art has been involved in optimizing the growth using either molecular beam epitaxy (MBE) or organometallic vapor phase epitaxy (OMVPE). (MBE has generally proven more successful in this regard, since OMVPE requires higher temperatures and lacks a good N precursor [30]. OMVPE also tends to introduce C and H impurities, which are detrimental to device performance.) In addition, the technologically-interesting compositions to achieve 1300–1600 nm wavelength require relatively large concentrations of N, In, and/or Sb and lead to significant lattice mismatch with the GaAs substrate (up to 2.5% compressive strain). The mismatch limits the total thickness of material that can be grown epitaxially to less than a few tens of nanometers in the best case. Strain compensation can assuage this limitation to some extent by growing quantum wells with tensiley-strained barriers. Also, the benefit of the surfactant properties of Sb in improving growth morphology has already been mentioned above; additional detail is found later in this thesis.

A critical issue plaguing GaInNAs(Sb) is the generally poor luminescence efficiency and broad emission linewidth of the as-grown material due to defects from the low-temperature growth. Thermal annealing (e.g., in a rapid thermal annealing oven with a $N_2$ ambient at 700–900°C for 30–180 sec) has been found to improve the luminescence intensity by a factor of 20–100, but is accompanied by an anomalous and undesired blueshift of the wavelength, typically by 50–100 nm [31, 32]. Understanding the origin and mechanism of this blueshift and potential strategies to control it comprise a large portion of this dissertation, in addition to generally understanding the

unique properties of this material system in relation to optoelectronic applications.

## 1.3 Outline and Organization of Thesis

In this dissertation, combined theoretical and experimental efforts are used to elucidate the role of N in the unique structure-processing-property relationships of the GaInNAs(Sb) material system. Understanding the intricacies of the atomic structure and bonding in this material system is important for both improving the material quality and controlling the properties relevant for fabrication of optoelectronic devices. The focus is on the nature of the band edge optical transitions, the relationship to atomic structure, and changes with thermal annealing. In the course of this pursuit, measurements of optical absorption from GaInNAs and GaInNAsSb quantum wells further demonstrate a particular promise of these materials for optical modulator devices operating in the 1300–1600 nm wavelength range — an application that perhaps has received less attention in the past than warranted.

Chapter 2 begins by describing the details of the experimental techniques employed. The specifics of the MBE growth procedure as well as the test device fabrication are included. A variety of techniques were used to probe the material properties. These include x-ray absorption spectroscopy to directly measure the atomic bonding in the material and various optical spectroscopies to study the band edge transitions (photoluminescence, photocurrent/absorption, electroreflectance, electroluminescence). Temperature-dependent measurements were also performed, and the apparatus used for this purpose is described.

Chapter 3 discusses theoretical calculations of the band structure of GaInNAs using density functional theory. A framework is developed to understand the role of N in the anomalous band gap bowing of the dilute-nitride arsenides and to quantify the sensitivity of the band-edge states (and band gap) to atomic structure, including

N nearest neighbor bonding and N clustering. The nature of the optical transitions is addressed from a theoretical point of view.

X-ray absorption results are presented in Chapter 4 that complement the calculations in Chapter 3 and also provide a direct measure of the atomic structure in as-grown and annealed material (vis-à-vis the N nearest neighbor bonding). Additional *ab initio* simulation results of the density of states are discussed in the context of the x-ray absorption data and understanding the relationship between atomic structure and the band gap shift with annealing. A general conclusion is reached that as-grown MBE GaInNAs contains a nearly random distribution of bonds, preferring N–Ga nearest neighbors, and that thermal annealing drives a transition toward thermodynamic equilibrium characterized by a high degree of N–In bonding and an associated larger band gap. Furthermore, a comparison between strain-relaxed thick-films and compressively strained thin-films shows that strain does not affect the bonding in GaInNAs nor the redistribution upon annealing.

Chapter 5 further quantifies the distribution of N nearest neighbors in the material during thermal annealing, using a combination of optical spectroscopies and drawing from the results of the XAS experiments and *ab initio* band structure calculations. Furthermore, experiments on GaInNAsSb show that the presence of Sb affects the spectrum of band-edge states, but not the dependence on atomic structure since Sb (a Group V element) does not influence the N–Ga/In bonding to first order. Particularly, as-grown MBE GaInNAsSb, like GaInNAs, contains a random distribution of nearest neighbor bonds (shown to be precise quantitatively) and that thermal annealing drives the material toward an equilibrium state with a high degree of N–In bonding and a larger band gap. An important implication of the findings is that sufficient annealing leads to an equilibrium state in which the band gap shift has saturated and remains constant, although further annealing can continue to improve luminescence.

In Chapter 6, measurements of optical absorption spectra of GaInNAs and

GaInNAsSb quantum wells using photocurrent are described. These results provide fundamental information on the strength of the optical transitions, and show an increase in the oscillator strength after thermal annealing related to the atomic rearrangement. The large increase in photoluminescence intensity observed after annealing is mostly attributable to the removal of nonradiative recombination centers introduced during the material growth and only slightly to this increase in oscillator strength, but the absorption spectrum is increased by nearly a factor of two from essentially this effect alone. Spectra taken with varying electric fields applied across the quantum wells demonstrate for the first time quantum confined Stark effect behavior of GaInNAs(Sb) over the 1300–1600 nm wavelength range, with the presence of sharp exciton resonances, even at room temperature. Much of the reason for the past neglect of modulator applications for GaInNAs had to do with the lack of high quality material which precluded the observation of strong excitons, in addition to the difficulty of achieving long wavelengths. The great potential for the fabrication of optical modulators using our GaInNAs(Sb) materials, for use in telecommunication and low-voltage optical interconnect applications to overcome the bottlenecks described in Section 1.1, is discussed in Chapter 6. Device performance comparable to the existing technology using InGaAs(P) on InP is expected, and a design for an asymmetric Fabry-Perot reflection modulator operating at 1550 nm using a GaInNAsSb active layer is presented.

# Chapter 2

# Experimental Details

This chapter presents details of the experimental techniques used for the various measurements discussed in this work, as well as some theory of the measurement physics. The details of computer simulations that also were an integral part of the studies performed are found in Chapter 3.

## 2.1 Molecular Beam Epitaxy (MBE)

### 2.1.1 Growth Details

Samples were grown using solid-source molecular beam epitaxy (MBE) in two interconnected ultra-high vacuum Varian Gen II chambers equipped with load locks [12, 14, 15, 33]. Typical base pressures of $\sim 10^{-10}$ Torr were achieved by using both cryo-pumps and ion pumps. Dimeric arsenic was supplied by a valved cracking cell, while mostly monomeric antimony was supplied by an unvalved cracking cell (both using 850°C cracking temperature). Nitrogen was supplied by a Semiconductor Vacuum Technology Associates (SVT) Model 4.5 radio frequency (rf) plasma cell fed by 99.999% pure $N_2$ from a cylinder. A purifier between the gas cylinder and the plasma cell was used to remove much of the residual oxygen impurity. The plasma cell was operated with 300 W of forward rf power and a $N_2$ flow rate of 0.5 sccm, and was

modified with an aperture containing 4 holes of diameter ∼250 $\mu$m. The nitrogen mole fraction in the epitaxial films was controlled by the total group III growth rate; the plasma conditions were not modified during growth [33]. Conventional effusion cells supplied Ga, In, Al, Si, and Be (the latter two serve as $n$- and $p$-type dopants, respectively). For Ga and In, SUMO cells were used.

Prior to growth, GaAs wafers were cleaned in a separate chamber by heating at 350°C for 1 h, and after inserting into the growth chamber, native oxide removal was performed at ∼590°C for 10 min under As overpressure. A 3000 Å buffer layer of GaAs was grown before growth of the desired epitaxy. GaAs and AlGaAs layers were grown at a substrate temperature of ∼600°C with 15× As beam equivalent pressure (BEP) overpressure, while AlAs layers were grown ∼30°C hotter. GaInNAs(Sb) quantum well (QW) layers were grown at 420–455°C with 20× As BEP overpressure, with Sb-containing layers generally being grown at the hotter end of the temperature range. GaNAs layers were grown at ∼455°C with 15× As BEP overpressure. Typical growth rates were ∼1.6 Å/sec for the QWs and ∼1 Å/sec for the other layers. Either $n$+ or semi-insulating GaAs substrates were used, depending on the sample requirements.

As mentioned above, the N composition is determined (inversely) by the total group III growth rate. Since our MBE chamber has only single Ga and In cells, the compositions of the In-containing QWs and non-In-containing GaNAs barriers were not independent. The N content in the QWs is automatically lower than in the barriers since the incorporation of In in the QWs increases the overall growth rate of those layers (by as much as 60%). In addition, the incorporation of Sb tends to enhance N incorporation by ∼50–100% with respect to material grown under identical conditions without Sb [34]. Compositions were determined using a combination of flux calibrations using RHEED, x-ray diffraction calibrated with nuclear reaction analysis in Rutherford backscattering, and photoluminescence.

Refinements of the growth process include the following. Plasma ignition and

stabilization was performed for 20 min prior to active layer growth to improve material quality. To protect the wafer during plasma ignition, an As cap is deposited on the wafer prior to ignition that getters much of the impurities resulting from the plasma transient. The As cap is removed by heating to 350–400°C following plasma stabilization and prior to continuing growth [35, 36]. A similar procedure is also used to protect the wafer during transfer between the two MBE chambers, which are separately optimized for high-rate (Al)GaAs growth and for active region GaInNAs(Sb) growth. The high growth rate (Al)GaAs chamber is used for the growth of cladding layers, as well as distributed Bragg reflector (DBR) layers.

After growth, GaInNAs samples were rapid thermal annealed (RTA) in $N_2$ ambient at 760–800°C for 1–2 min, while GaInNAsSb samples were annealed at 760–800°C for 1–3 min, using an AG Heatpulse 310 RTA oven. GaAs proximity caps were used to prevent As desorption during annealing. Thermal annealing was performed to improve crystal quality by removing nonradiative defects and increase photoluminescence efficiency.

Typical compositions of GaInNAs/GaNAs quantum wells (QWs) were 30% In and 1.6% N in the QWs, with 2% N in the barriers, for a band gap near 1300 nm (∼0.95 eV). GaInNAsSb/GaNAs QWs contained approximately 40% In, 2.5% N, and 2.7% Sb in the QWs, with 2.7% N in the barriers, for a band gap near 1550 nm (∼0.8 eV). The compositions could be varied to achieve band gaps spanning most of the telecommunications wavelength range of 1300–1600 nm, with higher concentrations of In, N, and/or Sb generally yielding longer wavelength material.

### 2.1.2 P-I-N Diode Sample Fabrication

Diode samples were used for photocurrent, electroluminescence, and electroreflectance measurements. Photoluminescence from diode samples was also performed for direct comparison with the other techniques.

Diode samples consisted of a 1.38 $\mu$m thick $1\times10^{18}$ cm$^{-3}$ Si-doped GaAs $n$-type region followed by a 0.5 $\mu$m thick GaAs nominally intrinsic region ($<1\times10^{15}$ cm$^{-3}$ $n$-type) and 1.0 $\mu$m of $5\times10^{17}$ cm$^{-3}$ Be-doped GaAs $p$-type region, all grown on a semi-insulating GaAs substrate. A 50 nm-thick, highly doped ($\sim5\times10^{19}$ cm$^{-3}$ Be) cap layer was included to facilitate making ohmic contact to the $p$-layer. Multiple GaInNAs(Sb) quantum wells (8 nm thick) with GaNAs barriers (20 nm thick) were grown in the center of the $i$-region, maintaining the total 0.5 $\mu$m thickness. Up to 9 GaInNAs QWs or 3 GaInNAsSb QWs were included.

Double top-contact circular mesa structures were fabricated for testing, as follows. Top $p$-type contact metal was deposited with electron beam evaporation and consisted of Ti/Pt/Au (250/400/2300 Å). The top contact included a circular aperture in the center for optical probing of the devices and was designed wide enough to provide mechanical stability after etching into mesas. Table 2.1 summarizes the aperture diameters used and the corresponding mesa diameters. Metal patterning was accomplished with a lift-off procedure using a photoresist bi-layer consisting of Shipley Microposit LOL2000 (2000 Å; non-photosensitive) and Shipley Megaposit SPR 3612 (1.5 $\mu$m; photosensitive). After exposure, the resist bi-layer was developed in Shipley Microposit LDD 26-W until the LOL2000 was visibly undercut. The metal film was then deposited, and lift-off was performed in Shipley Microposit 1165 Resist Stripper heated to 60°C and sonicated for 45–60 min. Metal lift-off was followed by rinsing with acetone-methanol-isopropanol to remove metal particles from the wafer surface.

Following top contact metallization, the central apertures were protected with hard-baked SPR 3612 (130°C for 30 min). Mesas were etched down to the $n$-layer with a PlasmaQuest ECR plasma etcher, using chlorine chemistry. The top contact metal served as a self-aligning mask for the mesa etch. Typical etch conditions consisted of 400 W ECR power; gas flows of 15 sccm Ar, 10 sccm $BCl_3$, and 1.5 sccm $Cl_2$; 2 mTorr

Table 2.1: Mesa diameters of diode devices.

| Aperture Diameter ($\mu$m) | Mesa Diameter ($\mu$m) |
|---|---|
| 250 | 900 |
| 500 | 1400 |
| 750 | 1800 |
| 1000 | 2400 |

chamber pressure; −60 V wafer bias; and 0–25°C chuck temperature. Samples were placed on Si carrier wafers and held in place either with copper tape for high chuck temperatures or Si "rails" for lower chuck temperatures. Typical etch rates were ∼20 Å/sec. Laser reflectometry was used for endpoint detection, stopping the etch within the $n$-type contact region.

After etching the mesas, the bottom $n$-type contact metal was deposited using evaporation and lift-off, similar to the top contact. For the $n$-contact, Au/Ge/Ni/Au (400/125/125/2000 Å) layers were deposited, then alloyed at 400°C for 45–60 sec in a rapid thermal annealer with nitrogen ambient. The bottom contact rings were 100 $\mu$m wide and spaced 20 $\mu$m from the mesa edges. A cross section of the finished device is illustrated in Fig. 2.1.

Prior to each process step, surface oxide removal was performed by dipping in 1:1 ammonium hydroxide:deionized water for 60 sec, then drying.

The dual top-side contact mesa structure described above was designed to facilitate wirebonding of individual devices into test packages and to assist in carrier collection for photocurrent measurements by placing both metal contacts close to the active region. In addition, current bunching and voltage nonuniformities in the active region were minimized in the devices by the large mesa diameters with respect to the apertured device areas (Table 2.1), the relatively large thicknesses of the doped regions, and the large area of the metal layers.

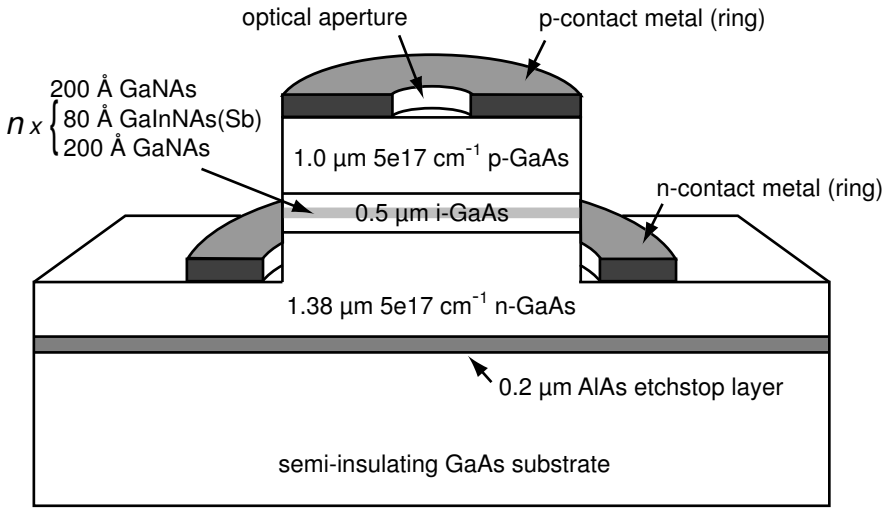


Figure 2.1: Cross section of finished diode device.

## 2.2 X-Ray Absorption Spectroscopy (XAS)

### 2.2.1 Introduction to XAS

X-ray absorption spectroscopy (XAS) is an analytical technique that can be sensitive to individual atomic bonds in molecules or crystals. For this reason, we used XAS to directly examine the nearest neighbor bonding in GaInNAs(Sb) alloys and relate the atomic structure to the observed optical properties (e.g., band gap). The technique generally involves exciting core electrons into empty levels above the Fermi level using x-rays tuned in energy to produce the desired transition, then scanning the incident x-ray energy to obtain information on the joint density of states around that transition. This density of states, which is proportional to the number of absorbed x-rays at each energy, can be very sensitive to local atomic structure, or chemical environment. The experiment often requires a very bright source of x-rays, such as available from a synchrotron. The terminology used to describe the excitations is borrowed from atomic spectroscopy, so for example, a transition of a $1s$ electron into the conduction

band (or into the vacuum level) is called a $K$ transition.

Two experimental regimes exist for XAS that essentially differ in the energy range above the transition edge that is probed and the corresponding resolution of the spectra. Near-edge x-ray absorption fine structure (NEXAFS; also called XANES, or x-ray absorption near-edge structure) probes a few to ∼10 eV of spectral range above the transition edge, with high energy resolution <0.1 eV [37]. The NEXAFS energy region is most sensitive to changes in the density of states and chemical environment. Extended x-ray absorption fine structure (EXAFS) probes a much wider energy range up to several 100's of eV above the transition edge, exciting the electron into the vacuum level, and may use lower energy resolution [38]. The EXAFS signal is essentially an interference pattern resulting from backscattering of the excitation exit wave from the atoms surrounding the excited atom. By converting the energy spectrum of the backscattered amplitude into a reciprocal space spectrum through the equation $k = \sqrt{2m(E - E_0)/\hbar^2}$ and performing a Fourier transform (see details in Section 2.2.3), one can obtain a radial distribution function which reveals information about bond lengths in the atomic shells surrounding the excited atom. These bond lengths can be sensitive to local atomic arrangements.

In general, x-ray absorption experiments can be performed three ways. The first is to directly measure the transmission of x-rays through a sample, however obtaining good signal-to-noise ratio is difficult with this approach and the experiment is not amenable to epitaxial samples where the substrate would absorb much of the x-ray intensity. The other two techniques—fluorescence and electron yield—measure emission resulting from the relaxation process of the excited atom. In fluorescence, x-ray emission from outer electron transitions into the photoexcited core hole are detected. For electron yield, the intensity either of emitted Auger electrons (partial yield) or of inelastically scattered electrons (total yield) resulting from the relaxation process are measured. The electron yield technique is very surface sensitive (within

a few atomic layers from the surface) since it probes exiting electrons, but can be especially sensitive to light elements which have a large Auger emission cross-section. However, electron yield is only useful for probing elements in the sample with more than ∼1 at% concentration and also requires a conducting surface. The fluorescence technique is useful for dilute elements and for probing deeper into the sample (the x-ray absorption depth is typically on the order of tenths of $\mu$m), and does not require a conducting surface. In addition, with fluorescence, the spectral information of the emitted radiation can be used to improve the signal-to-noise ratio by counting only the characteristic x-rays emitted by the atom of interest.

### 2.2.2 Near Edge X-Ray Absorption Fine Structure (NEXAFS)

Nitrogen $K$-edge NEXAFS spectra (onset ∼400 eV) were obtained at beam line 4.0.2 of the Advanced Light Source (ALS) at Lawrence Berkeley National Laboratory [39–41], using fluorescence detection with a high-resolution superconducting tunnel junction x-ray detector operated at ∼0.1 K [42, 43]. The ALS is a third-generation synchrotron producing very intense beams of soft x-rays ($10^{12}$ photons/sec/mm$^2$), which was critical for our measurements, especially for thin-film samples where the signal-to-noise ratio is low due to the small interaction volume. The tunability of the incident x-ray energy was provided by a variable-included-angle plane grating monochromator consisting of gold stripes on a silicon wafer. The Gaussian FWHM resolution of the monochromator around 400 eV x-ray energy was ∼0.07 eV [41].

Fluorescence detection was used, despite nitrogen's light atomic mass, to provide good sensitivity to the low concentration and also since the surface was non-conducting (undoped). In fact, even if the samples were doped, the tendency of surface states to pin the Fermi level near mid-gap in III-V semiconductors would lead to a surface depletion of carriers and leave the surface non-conducting. In addition, the deeper probe depth of the fluorescence measurement allowed better sampling of

the N atomic bonding in the material. The use of the superconducting tunnel junction detector operating as a photon counter provided for increased signal detection (high detector quantum efficiency) due to the extremely small band gap, relative to ordinary semiconducting (e.g., Ge) detectors. The high quantum efficiency is gained at the expense of a small detector area, which requires positioning the detector very close to the sample. In our case, a 3×3 array of 9 detector elements was utilized to increase the effective detector area. The data from each channel were independently calibrated before being summed. The detector could resolve 15 eV in emission energy, allowing excellent discrimination between the characteristic emission from N *vs.* O or C impurities, for increased signal-to-noise ratio [43]. The low Curie temperature of the superconductor used in the detector required multi-stage cooling, including magnetic cooling in the final stage, to achieve the required 0.1 K operating temperature.

Several non-idealities of the NEXAFS setup are worth mentioning. First, the grating monochromator on the x-ray beam line results in a second harmonic with ∼10× lower intensity than the fundamental. For N-$K$ edge spectroscopy at ∼400 eV, the second harmonic at ∼800 eV can excite the O-$K$ edge (onset at ∼530 eV). Thus, the formation of surface oxides needs to be carefully avoided, since even a thin oxide layer can contain much more O than there is N in our samples. To minimize surface oxidation of our samples, a stainless steel desiccator was constructed to transport samples under vacuum (or dry $N_2$ ambient) after removal from the MBE chamber. The samples were exposed to air only for about 10 min during transfer to the NEXAFS chamber, which is under ultra-high vacuum ($10^{-8} - 10^{-9}$ Torr). This careful sample transportation scheme proved critical to obtaining good spectra from our samples. Another non-ideality in the setup was that the detector was tuned for higher-energy edges, and had a low-energy tail peaked near 400 eV, precisely in the energy range of interest, possibly leading to a reduction in resolution. Additionally, three infrared blocking windows were between the sample and the detecting elements, reducing the

detection efficiency. Also, carbon in the windows absorbed radiation in the 300–400 eV range, further reducing efficiency. Ultimately, the result was detection at less-than-optimum efficiency. On the other hand, the XAS signal is highest when probing a light element in a heavy matrix, which was the case for N in GaInNAs.

Both thick-film (relaxed) and thin-film (biaxially strained) samples were grown and measured by NEXAFS. Thick-film samples of GaInNAs were 3000 Å thick and grown on top of GaAs buffers on $n+$ GaAs substrates. Thin-film samples of GaInNAs consisted of uncapped 100 Å films. The thick-film samples were easier to measure due to the film thickness being comparable to the x-ray absorption length ($\sim$0.1 $\mu$m), but the thin-film samples were more representative of the strained quantum well layers used in optoelectronic devices. The relaxed thick-film samples contained a relatively large number of misfit dislocations, however the average distance between dislocations was very large compared to the distance scale of the measurement sensitivity (on the order of a bond length) and also the x-ray beam was large enough to yield a spatial average insensitive to the dislocations. Comparison of the results for thick-film and thin-film samples in Section 4.1 confirm this assertion.

The GaInNAs compositions were approximately 30% In and 3% N (per Group III and Group V atoms, respectively), tuned for approximately 1300 nm band gap. Reference thick-film (1500 Å) GaNAs samples were also grown and measured, containing 3% N for comparison with the GaInNAs samples. As-grown and annealed samples from each wafer were examined separately. The annealing conditions were $\sim$720–820°C for 1–2 min.

### 2.2.3 Extended X-Ray Absorption Fine Structure (EXAFS)

Indium $K$-edge EXAFS spectra (onset $\sim$27.94 keV) were measured in fluorescence at beamline BL01B1 of SPring-8 in Japan using a liquid $N_2$-cooled Ge detector. Fluorescence was a good detection technique for the high concentration of In, which

is also a heavy element. In addition, the large signal level did not require a special detector (such as the STJ detector used for NEXAFS). A large area Ge detector was used to maximize the fraction of emitted radiation collected.

The samples used for EXAFS consisted of 100 Å-thick films of GaInNAs (∼30% In, ∼3% N, similar to the NEXAFS samples) grown strained on GaAs substrates. Both as-grown and annealed (∼720–820°C for 1–2 min) samples were examined. Reference thin-film samples of GaInAs (25% In) were measured as well.

Following, several key points of the data analysis procedures used to extract the radial distribution function (RDF) from EXAFS data are summarized. An excellent treatment of the full procedure, as well as general theory of the EXAFS technique, is found in Teo [38], which should be consulted for additional details. Beginning with the raw (transmission or fluorescence) data converted to linear absorption coefficient $\mu(E)$, the background intensity is removed by first subtracting an extrapolation of the pre-edge fit to a line and then subtracting a smooth "background absorption" function $\mu_0(E)$, obtained by fitting the edge to a cubic spline. The $\mu_0(E)$ function removes low-frequency oscillations due to systematic experimental fluctuations in the spectrum. (Other background absorption functions may also be chosen instead of a cubic spline.) After converting photon energy $E$ to reciprocal-space wavevector $k$ via

$$k = \sqrt{\frac{2m}{\hbar^2}(E - E_0)}, \tag{2.1}$$

where $E_0$ is the edge energy and $m$ is the mass of an electron, then normalizing the background-substracted data, the basic spectrum for analysis is obtained as

$$\chi(k) = (\mu - \mu_0)/\mu_0. \tag{2.2}$$

Before taking the Fourier transform of the the $\chi(k)$ data to construct the RDF, the

data needs to be equalized, to remove undue weight from large amplitude oscillations at low $k$ values. Because the EXAFS signal comes from an atomic absorption edge, the intensity at large $E$ (or $k$) is attenuated, but the interatomic distances depend on the frequency of the EXAFS oscillations and not the amplitude. Thus, the data can be equalized by multiplying by a weighting function, usually $k^3$. Then, the $k^3\chi(k)$ data is Fourier transformed (usually employing a window function such as a Hanning function to avoid spurious peaks from the boundaries of the experimental data) to obtain $\rho(r')$, which is the RDF. The $r'$ signifies that an offset (usually on the order of 0.2–0.5 Å) is present in the distance scale of $\rho(r')$, corresponding to a phase shift that depends on the elements involved and other parameters. The amplitudes of the peaks in $\rho(r')$ do not exactly correspond to a true RDF of the atomic distances due to the weighting factor introduced in the raw data and thus cannot be considered to be precise quantitatively; however, the relative positions of the peaks are reliable.

## 2.3 Photoluminescence (PL)

Photoluminescence (PL) is a commonly used technique to probe the band gap of a semiconductor and also the material quality [44]. The experiment involves using an excitation laser with energy above the band gap to create electron-hole pairs in the material. The generated carriers quickly relax via phonon scattering to the bottom of the conduction band and top of the valence band, where they can recombine radiatively across the band gap. The emitted luminescence is detected, yielding a spectrum peaked at (or near) the band gap energy. The intensity (or quantum efficiency) of emitted light is inversely proportional to the number of non-radiative recombination centers, and thus gives a measure of the material quality.

### 2.3.1 Experimental Setup

Photoluminescence was collected using the experimental setup shown in Fig. 2.2. The 488 nm line of an $Ar^+$ laser was used as the excitation source, allowing efficient absorption of the pump beam by both the quantum well material and the GaAs cladding. A collinear excitation/emission geometry was employed with the pump beam reflected by a dichroic mirror that passes only wavelengths longer than 620 nm and then focused onto the sample with a 0.3 NA lens. The lens also acted as part of the luminescence collection optics, focusing the emitted light onto the entrance slit of an Acton SpectraPro 300i 0.3 m grating spectrometer. A Newport 818-IG InGaAs photodiode placed at the exit slit of the spectrometer was used to detect the luminescence using lock-in detection with a Stanford Research Systems SR830 digital lock-in amplifier (the pump beam was chopped at 307 Hz). The spectrometer and lock-in amplifier were computer controlled to automate the measurement.

The collected PL spectra were corrected to account for the spectral dependence of the optics and the detector by a measured system response. Additionally, second order reflections from the single-grating spectrometer were eliminated, if desired, by inserting a long-pass filter.

For diode samples, the pump beam was focused onto the quantum wells through the top $p$-doped layer. The collected luminescence was lower in this case from absorption of the emitted light by the $p$ layer. In addition, PL spectra could be measured from the diode samples with various dc biases applied.

### 2.3.2 Photoluminescence Theory

Here we present a brief theory of the physical processes related to the photoluminescence (PL) experiment, relevant to the discussions that follow later in this dissertation. Much of the material presented is adapted from Ref. [44], where more detail can be

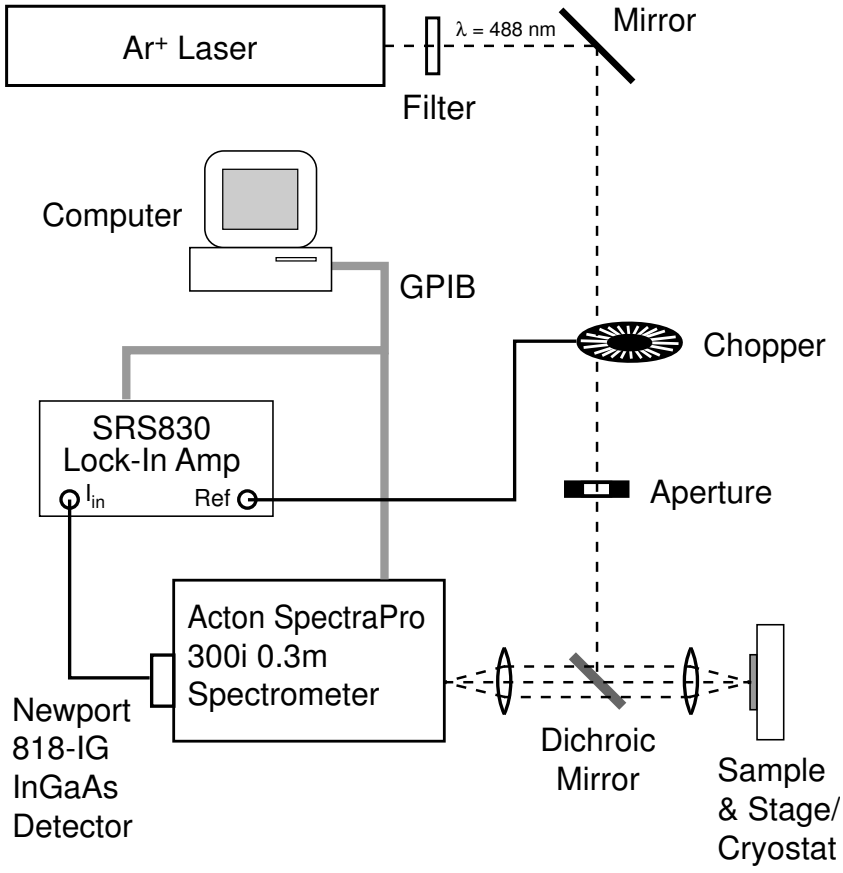


Figure 2.2: Schematic of photoluminescence apparatus.

found.

Photoluminescence refers to the spontaneous emission of optical radiation from a sample when excited to a nonequilibrium state by irradiation with light. The irradiated light is absorbed at the surface of the material, generating electron-hole pairs (EHPs). After some diffusion of the generated carriers, a fraction of them will recombine radiatively, producing light. A certain fraction of the generated light will escape from the sample, where it can be detected. The rest of the recombination radiation either suffers from self-absorption in the sample or is directed away from the observation point. Competition between the three processes of absorption, diffusion, and recombination occurs during the PL experiment, and usually the steady state is measured.

For this work, the PL experiments involved only direct gap semiconductor samples, so we will restrict some of the details of the discussion here to this special case. In our experiments, the 488 nm line of an $Ar^+$ laser was used to excite the samples, generating hot electrons and holes in the conduction and valence bands, respectively, of the GaAs substrate/cap as well as the Ga(In)NAs(Sb) QW/barrier material since the energy is significantly above the band gap. The hot carriers quickly relax (few picosecond timescale) to the bottom of the conduction band and top of the valence band via phonon interaction [45]. For the electrons, significant scattering to the $L$ and $X$ valleys occurs before energy exchange with LO phonons to bring the electrons to the bottom of the lowest energy $\Gamma$ valley. (Further details of these carrier dynamics in semiconductors is discussed in Ref. [46] and references therein.)

After relaxing to the band minima, the electrons and holes can recombine to emit radiation. The recombination lifetime (hundreds of picoseconds to nanoseconds [47, 48]) is much longer than the carrier relaxation rate, so most of the recombination occurs directly across the band gap, which is also a critical point in the band structure ($\nabla_{\mathbf{k}} E_{\text{final}} - \nabla_{\mathbf{k}} E_{\text{initial}} = 0$). Depending on the rate of generation (i.e., the power

density of the excitation source) and the recombination rates, some bandfilling can occur within the semiconductor, however in QWs this is often negligible due to the very high density of states at the band edge. Nonradiative recombination can also take place, especially at crystal defects, and will reduce the luminescence efficiency. In this way, the intensity of PL is a measure of material quality, although the intensity can also be affected by the structure of the sample.

The mechanism described above implies that PL is mainly a ground state spectroscopy, probing the fundamental band gap energy of the semiconductor. With high excitation density and high sample temperatures (large $kT$), some bandfilling can be induced even in QWs, but the intensity of "excited state" emission is greatly attenuated due to the sharply decreasing carrier population at higher energies in the bands. The ground state nature of PL is a characteristic that is very important in the discussion of results below.

In the low excitation density regime, the dominant luminescence mechanism is spontaneous emission. A relation between the spontaneous emission spectrum and the absorption spectrum can be derived from Fermi's Golden Rule and is given by

$$R_{\rm sp}(\hbar\omega) = V_{\rm en} G(\hbar\omega)\alpha(\hbar\omega)e^{-\hbar\omega/kT}e^{-\Delta F/kT}, \tag{2.3}$$

where $R_{\rm sp}(\hbar\omega)$ is the spontaneous emission rate spectrum, $V_{\rm en}$ is the energy velocity (equal to the group velocity in a dielectric medium), $G(\hbar\omega)$ is the optical density of states, $\alpha(\hbar\omega)$ is the absorption spectrum, and $\Delta F$ is the induced separation in electron and hole quasi-Fermi levels from the generation of EHPs [49]. Equation (2.3) is a generalized form of what is called the van Roosbroeck-Shockley relation [50] (or "detailed balance"), for direct band-to-band recombination.

The important consequence of Eq. (2.3) is the proportionality between spontaneous emission and absorption. Particularly, a correlation of the lineshape in optical

emission (PL) and absorption spectroscopies is implied. A general theory of the lineshape for excitonic absorption was developed by Toyozawa [51], and through Eq. (2.3), has direct applicability to PL spectra. Essentially, Toyozawa's theory shows an expected Lorentzian lineshape at low temperatures that transitions to a Gaussian lineshape at higher temperatures as the coupling between excitons and phonons becomes more important. The transition temperature may be material-dependent. Additionally, Toyozawa showed that certain factors, such as crystal defects, translate into an effective increase in the temperature of the system. A final point regarding Eq. (2.3) is the $e^{-\hbar\omega/kT}$ term that multiplies the absorption spectrum. This term contributes to a low-energy shoulder (asymmetry) in the PL lineshape, that may be most noticeable at lower temperatures.

Analysis based on Eq. (2.3) assumes that the luminescence is dominated by spontaneous emission. In fact, it is possible to perform a PL experiment with high enough excitation density that stimulated emission becomes important as well, in which case the theory needs to be revised. In this case, the reabsorption rate of emitted photons is reduced as the excitation of the sample is increased [52]. If enough carriers are generated in the semiconductor such that the separation of quasi-Fermi levels exceeds the photon energy $\hbar\omega$, then the stimulated emission rate can exceed the spontaneous emission rate. This is the familiar condition for optical gain (or laser action), which is actually a simplified statement of the Bernard-Duraffourg condition [53, 54]. In practice, we avoid the experimental regime where stimulated emission has a significant contribution.

## 2.4 Photocurrent (PC)/Absorption

Photocurrent (PC) measurements were used to obtain (electro)absorption spectra from *p-i-n* diode samples with GaInNAs(Sb) QWs in the center of the intrinsic region. The technique measures the current generated from the device when electron-hole pairs are created from absorption of photons. In the limit of 100% internal quantum efficiency and 100% collection of generated carriers by the contacts, the photocurrent measurement yields a signal proportional to the absorption spectrum with high sensitivity.

### 2.4.1 Experimental Setup

Photocurrent measurements were accomplished using a monochromated broadband light source and lock-in current detection. Illumination was provided by a 250 W quartz-tungsten-halogen (QTH) bulb, which provides sufficient power in the wavelength range of our interest (1000–1800 nm). The bulb was fixed in an Oriel research housing with f/0.95 collimation optics. The light was passed through a 950 nm long-pass filter and focused onto the entrance slit of an Oriel 77200 0.25 m monochromator using a f/4.2 plano-convex lens to match the f/# of the monochromator. The long-pass filter was used to eliminate stray light from higher order reflections in the single-grating monochromator, that could be absorbed by the GaAs substrate. (For example, light at 775 nm can lead to significant background absorption when the monochromator is set at 1550 nm, if the filter is not in place.) Measurements in the spectral range from 1000–1800 nm were performed using a 1250 nm blazed grating. Typically, a monochromator resolution of $\sim$4 nm (FWHM) was achieved by using effective slit dimensions of $0.8 \times 9.7$ mm. A rectangular-to-circular quartz fiber bundle was used for efficient output coupling from the monochromator exit slit to the sample. A lens (f = 25 mm) was placed at the end of the fiber bundle to focus the

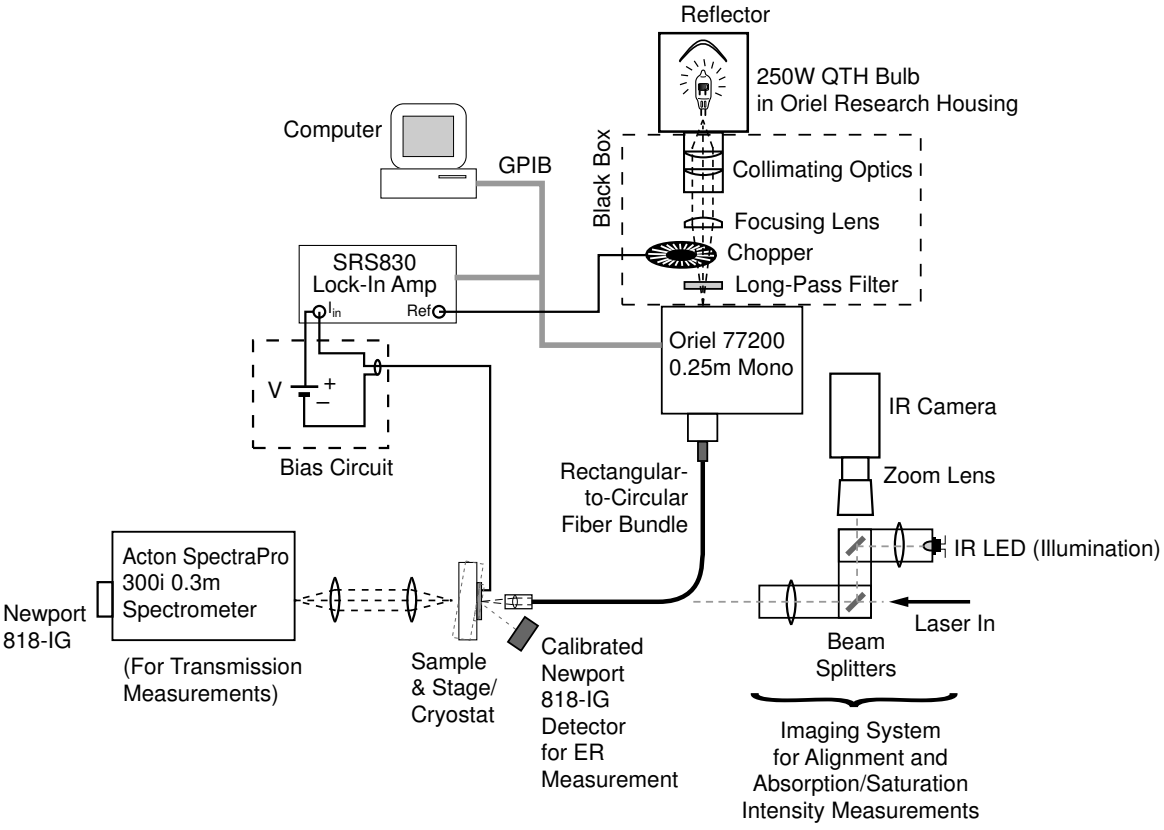


Figure 2.3: Schematic of the photocurrent experimental setup.

monochromated light onto the sample, which was placed inside a liquid helium flow cryostat for variable temperature measurements. Details of the cryostat are described in Section 2.7 below. The experimental setup is shown schematically in Fig. 2.3.

The output power spectrum of the monochromated light source was characterized using a calibrated InGaAs detector (Newport 818-IG). The detector was placed at the focal point of the output light to accurately calibrate the power incident on the sample. Figure 2.4 shows the output power spectrum of the monochromator with the 1250 nm grating installed.

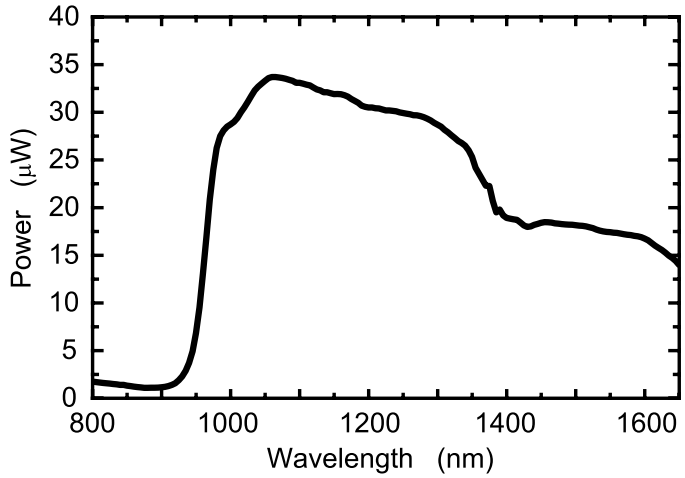


Figure 2.4: Monochromator output power spectrum, including effects of optics, long-pass filter, and fiber bundle.

Characterization of the output spot was also performed to enable accurate determination of the fraction of power incident on the test devices, which were designed with circular apertures. The profile of the beam was determined by placing a 100 $\mu$m slit in the focal plane of the illumination and an InGaAs detector behind the slit. The slit and detector were mounted together on a translation stage, while the illumination optics were fixed. The center of the beam was found by translating the slit until the power on the detector was maximized, then offsetting the slit by 50 $\mu$m (half the slit-width), so that the edge of the slit was located at the peak. The beam was profiled by recording the power on the detector while translating the slit in 100 $\mu$m increments. The beam profile was fit to a Gaussian to verify the shape of the beam and determine the beam waist, as shown in Fig. 2.5.

The photocurrent was detected using a Stanford Research Systems SR830 digital lock-in amplifier set to current detection mode. To bias the device, the auxiliary voltage output on the lock-in was used, in series with the device and the current input. The current input must be set to floating to maintain proper grounding of

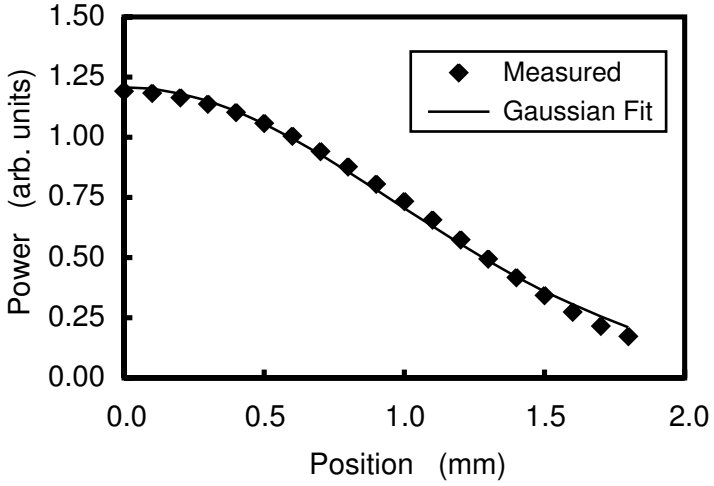


Figure 2.5: Monochromator output fiber bundle beam profile, measured at the focal plane, for 1250 nm light.

the bias circuit. The electric field across the QWs was calculated from the applied voltage using the depletion approximation and accounting for the built-in field as well as background $n$-type doping in the nominally intrinsic region (see Appendix C). The incident light was chopped at 307 Hz before the monochromator to enable lock-in detection. In low signal situations (low temperature, small reverse bias, or poor quality material), improved signal-to-noise ratio was achieved by employing both line filters (60 and 120 Hz) on the lock-in. Also, an increased dynamic range setting (which does not introduce measurement error on a digital lock-in) was used if excess noise overloaded the input. For all measurements, a 24 dB/octave low-pass filter roll-off and time constants of 100–300 ms were used. A settling time of 5–7 time constants was used between measurement points to avoid transient effects. The monochromator and lock-in amplifier were computer controlled to allow automated acquisition of a series of absorption spectra with various applied bias voltages.

The raw PC data was converted to absorption coefficient by assuming the maximum measured internal quantum efficiency (at high temperatures and voltage biases) was 100%, and including both QWs and barriers in the interaction length. Transmission measurements at a fixed wavelength were used to verify the calculated values of absorption coefficient. Interference effects of the multilayer structure on the illumination intensity were included in the calculation by using measured reflectivity spectra. The details of the conversion of the raw data to absorption coefficient is presented in the next section.

### 2.4.2 Theory of Photocurrent Measurement and Extracting Absorption Coefficient

When a photon is absorbed in a semiconductor, an electron-hole pair (EHP) is created which can generate a measurable current if extracted by external leads. Ideally, the magnitude of the photocurrent is proportional to the number of EHPs created, which in turn is proportional to the number of photons absorbed. In unbiased material (flat bands), the generated EHPs diffuse slowly in all directions and many recombine (radiatively or nonradiatively) before reaching the contacts, therefore not contributing to a photocurrent. If an electric field is applied to the material, the drift process greatly enhances the collection efficiency of generated carriers. A reverse biased *p-i-n* diode is an ideal structure for applying such an electric field. Since the drift velocity will depend on the magnitude of the electric field until saturation occurs, the collection efficiency will be higher (approaching 100%) for higher values of applied electric field (or equivalently, applied voltage across the diode).

In our case, the absorbing layers are QWs, which can trap carriers for appreciable time once generated due to the potential barrier for carrier emission. A competition exists between the carrier escape rate and the recombination rates (usually radiative

recombination is dominant since the carriers are already trapped in the QW). With a suitable applied field, we can assume that all the photogenerated carriers that escape from a QW are efficiently collected by the contacts, while a low escape rate can significantly reduce the collection efficiency of the carriers. When carriers escape from the well in which they were generated, they possess relatively high kinetic energy and travel near saturation velocity when a reasonable applied reverse bias exists, so we can safely assume these will reach the contacts. However, at low temperatures, little thermal energy may be available to assist in carrier escape (i.e. thermionic emission). High reverse bias (large electric field) across the QW can help mitigate this effect by lowering the potential barriers and helping to separate the generated electrons and holes. Measurements taken at high temperatures and high reverse bias exhibit the maximum internal quantum efficiency (IQE). In practice, spectra taken at room temperature with only moderate bias show saturation of the IQE (i.e., the photocurrent signal at wavelengths well above the band gap shows no change with increased bias); we assume this saturation to correspond to 100% IQE. The possible error associated with the assumption of 100% maximum IQE leads to a potential underestimate of the absorption coefficient, however this is preferable to an overestimate, with regards to the design of devices.

The absorption coefficient is related to the photocurrent, with the assumption of 100% IQE, by

$$i_p = qP_{\text{in}} \left(1 - e^{-\alpha \ell}\right) / \, h\nu, \tag{2.4}$$

where $i_p$ is the measured photocurrent, $q$ is the charge on an electron, $P_{\text{in}}$ is the incident power on the QWs, $\alpha$ is the absorption coefficient, $\ell$ is the interaction length, and $h\nu$ is the energy of the incident light. In deriving Eq. (2.4), we have assumed that light passing through an infinite stack of QWs will be absorbed in a "bulk-like" fashion and experience an exponential decay of intensity.

The value of $P_{\rm in}$ corresponds to the power reaching the active region (the QWs). Fresnel reflection from the device surface, absorption by the cryostat window, clipping from the device aperture, and free carrier absorption in the cladding all need to be considered. Experimental reflectivity spectra are used to account for the Fresnel reflection, which can have a significant spectral dependence due to the multilayer structure of the samples. The cryostat window introduces a fairly constant 9% absorption over the whole wavelength range of 1000–1800 $\mu$m (see Section 2.7). The device aperture is accounted by the known spot size from the fiber bundle (see Section 2.4.3). Finally, free carrier absorption (FCA) through the 1 $\mu$m or so of $p$-GaAs above the QW is essentially negligible for our samples. A rough estimate of the FCA in GaAs is $\sim$7 cm$^{-1}$ per $10^{18}$ cm$^{-3}$ $p$-type doping and $\sim$3 cm$^{-1}$ per $10^{18}$ cm$^{-3}$ $n$-type doping at 980 nm [55]. Even if this is an underestimate at wavelengths of our interest by an order of magnitude, the amount of absorption expected through the $p$-layer is less than 1%. This value is within the error in measuring the external incident power and from lack of knowledge of the true IQE, so FCA can be ignored.

The interaction length $\ell$ in Eq. (2.4) is somewhat poorly defined for a QW sample, and appears from analogy with bulk absorption. Theoretically, only the thickness of absorbing material should be included, but since there is significant wavefunction overlap with the QW barriers, the total QWs plus barriers thickness is used. This definition of $\ell$ is generally accepted as correct [56].

By rearranging Eq. (2.4) and substituting some more convenient quantities, we arrive at the following equation for $\alpha$ as a function of $i_p$, $P_{\rm in}$, and the incident wavelength $\lambda$:

$$\alpha = -\frac{1}{\ell}\left[1 - \frac{i_p}{P_{\rm in}\,(hc/\lambda)}\right], \tag{2.5}$$

with $\alpha$ given in cm$^{-1}$, $\ell$ in cm, and $(hc/\lambda)$ in eV. It is worth noting that the calculation of $\alpha$ from $i_p$ is rather sensitive to $P_{\rm in}$, requiring a good calibration of the input power

and spot size.

Incidentally, a slight modification to the measurement setup may be possible to allow an approximate determination of the lowering in quantum efficiency by carrier trapping in the wells, especially at low temperatures. Since most of the trapped carriers that do not escape from a QW will recombine radiatively, we can imagine measuring the light output from the QWs during the PC measurement. Since the substrate (GaAs) is transparent at the band gap of the QWs, we can collect the spontaneous emission from the backside of the samples. By tilting the collection optics for the emission with respect to the sample and PC probe beam, we would avoid difficulties with subtracting the large signal of the probe beam transmitting through the sample. Such experiments were not performed for this work because the photocurrent was observed to saturate at high temperatures and reverse biases, where there is reasonable confidence of achieving nearly 100% IQE. Thus, the spectra taken at low biases or temperatures could be scaled up to estimate the intensities corresponding to the maximum IQE (assumed to be 100%).

In general, the magnitude of the photocurrent will scale linearly with incident pump power, and the analysis described above is valid. An important exception to this rule is 2-exciton collision, which can significantly contribute to PC especially at high pump powers and for materials with very large absorption coefficient and long interaction length. Two-exciton collision is equivalent to having two high-energy EHPs in the crystal, and leads to an incorrect accounting of the number of carriers in the QWs via the analysis above [57]. In the ideal case, the 2-exciton collision process would scale as the light intensity squared, but in practice usually still scales linearly with the incident light intensity when the recombination probabilities are high. We neglect 2-exciton collision in our analysis, which is partially justified since the PC was observed to scale linearly with incident light power.

### 2.4.3 Power of a Gaussian Beam Through a Circular Aperture

We can represent the power (or intensity) in a cross-section of a Gaussian beam by

$$P = \frac{P_0}{2\pi\sigma^2} \exp\left(-\frac{\mathbf{r}^2}{2\pi\sigma^2}\right) = \frac{P_0}{2\pi\sigma^2} \exp\left(-\frac{x^2+y^2}{2\pi\sigma^2}\right), \tag{2.6}$$

where $P_0$ is the total power, $\sigma$ is the half-width, $\mathbf{r} = \sqrt{x^2+y^2}$ is the position in the plane relative to the beam center, and the beam is assumed to be axially symmetric. Then, the power included in a centered circular aperture of radius $R$ is given by

$$\int_0^{2\pi}\int_0^R \frac{P_0}{2\pi\sigma^2} \exp\left(-\frac{r^2}{2\sigma^2}\right) r dr d\theta = P_0\left[1 - \exp\left(-\frac{R^2}{2\sigma^2}\right)\right]. \tag{2.7}$$

The fraction of power within the aperture is

$$1 - \exp\left(-\frac{R^2}{2\sigma^2}\right). \tag{2.8}$$

In general, the power of the input beam is measured with a detector of finite size, and we wish to account also for the aperture effect of the detector in the input beam calibration. Then, the ratio of power within an aperture of radius $R_A$ compared to that measured by a detector of radius $R_D$ is

$$\left[1 - \exp\left(-\frac{R_A^2}{2\sigma^2}\right)\right] \Big/ \left[1 - \exp\left(-\frac{R_D^2}{2\sigma^2}\right)\right]. \tag{2.9}$$

This relation yields an approximately quadratic increase in power as the diameter of the aperture is increased. The functional form of Eq. (2.9) was experimentally verified.

## 2.5 Electroreflectance (ER)

### 2.5.1 Experimental Details

Electroreflectance (ER) spectroscopy was performed using a setup similar to that used for the photocurrent measurements, as shown in Fig. 2.3. The samples consisted of the *p-i-n* diode samples described above, with the QWs in the center of the 0.5 $\mu$m intrinsic region. As shown in Fig. 2.3, the sample stage was rotated at a small angle ($<10^{\circ}$) to the incident monochromated beam for ER measurements, configuring a symmetric reflection off of the sample and onto the calibrated InGaAs detector. During the measurement, a positive-square-wave, small-signal ac modulation voltage (typically 0–200 mV at 307 Hz and 50% duty cycle) was applied across the diode samples using an HP 8160A programmable pulse generator. Phase-sensitive detection with a lock-in amplifier was used to measure the modulated reflectivity. A dc bias could also be applied beneath the ac signal using the HP 8160A, to obtain ER spectra at various diode (reverse) bias voltages. The magnitude of the ac modulation was chosen to maximize the signal-to-noise ratio of the measured ER spectra, while verifying that the spectra were unchanged from those taken with smaller ac modulations. The spectra were also verified to be essentially independent of incident angle. The illumination for ER experiments was aligned on the sample by maximizing the photocurrent signal from the device, ensuring that the incident beam was centered on the device and focused onto the plane of the sample.

Slight modifications to the setup are possible for different measurement requirements. Instead of measuring the reflection at small angles, a beamsplitter could be inserted to perform a normal-incidence measurement, although this configuration would require additional calibration to account for the spectral nonuniformity of the beamsplitter. An avalanche photodiode with split ac/dc outputs could replace the Newport photodetector. Then, the ac signal could be sent to the lock-in amplifier,

while the dc signal would provide a direct, real-time measure of the background reflectivity, simplifying the determination of $\Delta R/R$ (the normalized modulated reflectivity, which comprises the ER signal) without having to measure the input power. This approach also can reduce errors in the determination of $R$, which otherwise requires a separate measurement. Another alternative would be to chop the input light at a higher frequency than the electric field modulation (being careful not to chop at a harmonic), and employ two lock-in amplifiers to directly measure the ratio $\Delta R/R$ in real-time.

The use of the *p-i-n* diode configuration for the samples, with the intrinsic region appreciably thicker than the QWs, leads to a nearly constant, homogeneous electric field across the QWs. Having a homogeneous electric field allows for accurate, direct, and quantitative interpretation of the spectra (as described in Section 2.5.2). Experiments similar to ER, such as photoreflectance (where a modulated pump laser beam is used to induce changes in surface electric fields) [58] and contactless electroreflectance (where the sample is immersed in an electrolytic solution to induce surface electric field modulations) [59], suffer from artifacts due to the rapidly varying and inhomogeneous electric fields present, in addition to requiring samples with exposed surface films. Proper and quantitative data analysis (as described below in Section 2.5.2) requires that the underlying assumptions of the mechanism of dielectric function modulation hold. The configuration we have used here best ensures these assumptions are valid.

### 2.5.2 Theory and Lineshape Analysis

Electroreflectance is a sensitive modulation spectroscopy technique that probes critical points in the band structure with a scanned-energy probe beam [58, 60]. The technique essentially measures a derivative of the absorption spectrum. Since the energy of the probe beam is varied to measure the spectral dependence and a derivative

measurement is performed, ER is equally sensitive to both ground and excited states, in contrast to PL which is mainly a ground state measurement technique. Modulation spectroscopy has been used to study the band structure of semiconductors for almost 40 years, since the original work on ER of germanium by Seraphin [61].

Despite the relative simplicity of the technique, much information on the band structure can be obtained, however careful analysis of the resulting spectra is required. Generally, the analysis consists of a peak fitting procedure to identify the critical point transitions and characterize their lineshape, broadening, and type. To perform the peak fitting, an assumption is made of the lineshape function describing structure in the dielectric function near critical points.

Traditionally, at least for bulk materials, a complex Lorentzian lineshape with a variable order parameter has been used successfully to fit the spectra [60]. In this model, the ER line can be written as

$$\Delta R/R = \Re\left[Ce^{i\theta}(E - E_0 + i\Gamma)^{-n}\right], \tag{2.10}$$

where $\Delta R/R$ is the measured modulated reflectivity, $C$ is an amplitude constant, $\theta$ is a phase factor, $E_0$ is the transition energy, $\Gamma$ is a broadening parameter, and $n$ is an order parameter which essentially gives the order of the derivative taken of the Lorentzian function [62, 63]. For multiple transitions, a simple linear sum of the form in Eq. (2.10) can be used, according to the standard critical point (SCP) model [64]. Theoretically, there is a correspondence between the value of $n$ and the type of critical point. Specifically, $n = 3.0$ corresponds to a 2D one-electron critical point, $n = 2.5$ corresponds to a 3D one-electron critical point, and $n = 2.0$ corresponds to a bulk excitonic transition. Empirical evidence also suggests that $n = 3.0$ successfully describes a 3D transition with an associated bound exciton or even the case of quantum wells [65]. Good agreement has also been reported between

experiment and theory for 3D excitonic transitions by decomposing the transition into a 3D single-electron (continuum) transition ($n = 2.5$) and an excitonic transition ($n = 2.0$) [66].

However, for quantum well (QW) samples (at high temperatures), a Gaussian-like function has been shown to be more appropriate in certain cases, due to the excitonic nature of the 2D QW transitions [67]. Furthermore, for our samples, a Gaussian lineshape was measured in photoluminescence, electroluminescence, and photocurrent experiments, so it is known that a Gaussian lineshape should be used for analysis. Toyozawa's theory of the lineshape of excitonic absorption [51] showed a transition from Lorentzian to Gaussian lineshape at higher temperatures due to the onset of strong exciton-phonon coupling, although "high temperature" usually implies well above room temperature. Toyozawa showed that an increase in lattice defects corresponds to an effective increase in temperature. The Gaussian lineshape for GaInNAs(Sb) QWs arises from strong exciton-phonon coupling due to a large exciton effective mass (a consequence of the large electron effective mass) and also a relatively large exciton radius which confines the interaction to a relatively narrow energy bandwidth at the bottom of the exciton band. Furthermore, the intrinsic "lattice defects" from the alloy nature of these materials and especially the high local strain around nitrogen atoms leads to an increase of the effective temperature. Thus, a Gaussian lineshape is observed for the GaInNAs(Sb) QW samples at room temperature and also at lower temperatures (down to $\sim$15 K). Others have also observed a Gaussian lineshape for GaAs multiple quantum well samples at room temperature [68]. In contrast, the lineshape of the GaAs band edge transition from the substrate and cladding is found to be Lorentzian, even at room temperature, as expected.

Proper quantitative analysis of ER spectra requires the use of the correct lineshape. A qualitative similarity exists between the Gaussian lineshape and the Lorentzian

lineshape with $n = 3.0$ (which explains why the latter has been used with some success for quantum wells and 3D excitons), but the different lineshapes will yield very different values for the broadening parameter [69]. In addition, the variation of the broadening parameter with respect to the other parameters (i.e., phase and transition energy) is different for the two lineshapes, so extracting quantitative information relies on the proper choice, which is Gaussian in this case. Following is a brief derivation of the Gaussian ER lineshape.

We begin with the fact that the ER technique measures derivatives of the dielectric function due to the applied modulating field [60], via

$$\Delta R/R = a\Re(\Delta\epsilon) + b\Im(\Delta\epsilon), \tag{2.11}$$

where $a$ and $b$ are the Seraphin coefficients and $\Delta\epsilon$ is the modulated dielectric function resulting from, in our case, modulation of the applied electric field (voltage) across the QWs. For isolated QWs experiencing a change in electric field $\Delta\mathcal{E}$, $\Delta\epsilon$ can be written [70]

$$\Delta\epsilon = \left(\frac{\partial\epsilon}{\partial E_0}\frac{\partial E_0}{\partial\mathcal{E}} + \frac{\partial\epsilon}{\partial\gamma}\frac{\partial\gamma}{\partial\mathcal{E}} + \frac{\partial\epsilon}{\partial I}\frac{\partial I}{\partial\mathcal{E}}\right)\Delta\mathcal{E}, \tag{2.12}$$

where $E_0$ is the transition energy, $\gamma$ is a broadening parameter, and $I$ is the integrated intensity of the transition. To proceed, we need to choose the appropriate lineshape to evaluate Eq. (2.12). Additionally, $b \ll a$ in the vicinity of the fundamental energy gap of semiconductors, so for our analysis Eq. (2.11) reduces to [60]

$$\Delta R/R \propto \Re(\Delta\epsilon). \tag{2.13}$$

The latter two terms in Eq. (2.12) can be lumped together, and following Shen *et al.*, assuming a normalized Gaussian lineshape, the modulated reflectivity can be written

as [67]

$$\begin{aligned} \Delta R/R &= A(1/\gamma^2)\Phi(1, 0.5, -0.5x^2) \\ &\quad + B(2x/\gamma^2)\Phi(2, 1.5, -0.5x^2), \end{aligned} \tag{2.14a}$$

where

$$x = (E - E_0)/\gamma, \tag{2.14b}$$

$\Phi(a, b, z)$ is the confluent hypergeometric function, and $A$ and $B$ are constants related to the optical matrix element of the transition and the relative contributions of band gap dispersion ($A$) and linewidth dispersion ($B$) to the signal, respectively. The relative magnitudes of $A$ and $B$ essentially represent a phase factor [analogous to $\theta$ in Eq. (2.10)], and the total amplitude of the transition can be taken as the quadrature sum

$$C = \sqrt{A^2 + B^2}. \tag{2.15}$$

Equation (2.14) represents the Gaussian lineshape. Incidentally, in Eq. (2.10) with $n = 2.0$ (Lorentzian lineshape for the excitonic case), the phase $\theta$ also is directly related to the relative contributions of $E_0$ and $\Gamma$ to the modulated dielectric function [70].

One difficulty in using the Gaussian lineshape of Eq. (2.14) is the effort required to compute the confluent hypergeometric function. For non-quantitative fitting, various analytical approximations can be used to considerably speed up the computations, although as discussed above the parameters will lose physical meaning. One approximation is to use the complex Lorentzian lineshape of Eq. (2.10) with $n = 3.0$. However, the curvature of the Gaussian lineshape is poorly reproduced with this approach. A better approximation can be constructed by observing that the "A" term in Eq. (2.14) looks like the second derivative (in $E$) of a real Lorentzian function given

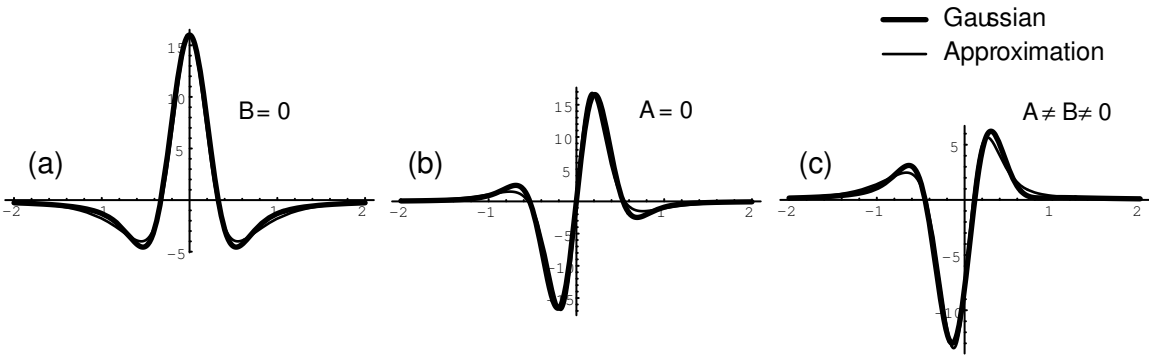


Figure 2.6: Approximation to the Gaussian ER lineshape, using a linear combination of (a) second and (b) third derivatives of a real Lorentzian function.

by $f(E) = \Gamma/\left[(E - E_0)^2 + \Gamma^2\right]$, while the "B" term looks like the third derivative (see Fig. 2.6). After simplification, this lineshape can be written as

$$\begin{aligned} \Delta R/R &= A\left\{\frac{2\Gamma\left[\Gamma^2 + (E_0 - E)^2\right]\left[3(E_0 - E)^2 - \Gamma^2\right]}{\left[\Gamma^2 + (E_0 - E)^2\right]^4}\right\} \\ &\quad + B\left\{\frac{24\Gamma(E_0 - E)(E_0 - \Gamma - E)(E_0 + \Gamma - E)}{\left[\Gamma^2 + (E_0 - E)^2\right]^4}\right\}, \end{aligned} \tag{2.16}$$

where the terms have the same meaning as in Eq. (2.14). This function can be computed very quickly, since it consists only of rational functions of polynomials, and when implemented in Origin 7.0 [71] showed at least a 2× speed improvement over Eq. (2.14) by avoiding evaluation of the (non-analytical) confluent hypergeometric function. Similar functions can also be constructed by combining derivatives of the real Lorentzian function with respective to both $E$ and $\Gamma$.

As an aside, the computation of the complex Lorentzian of Eq. (2.10) can also be

sped up by transforming to a real function:

$$\begin{aligned} f(x) &= \Re\left\{Ce^{i\theta}(x_0 - x - i\Gamma)^{-n}\right\} \\ &= \Re\left\{C(\cos\theta + i\sin\theta)\exp[-n\log(x_0 - x - i\Gamma)]\right\} \\ &= \Re\left\{C(\cos\theta + i\sin\theta)\exp\left[-n\left(\ln\sqrt{(x_0-x)^2+\Gamma^2} + i\cdot\mathrm{Angle}(-\Gamma, x_0 - x)\right)\right]\right\} \\ &= \Re\left\{C(\cos\theta + i\sin\theta)\cdot D\cdot(\cos K + i\sin K)\right\} \\ &= C\cdot D\cdot(\cos\theta\cos K - i\sin\theta\sin K), \end{aligned} \tag{2.17}$$

where in the last two lines we have introduced the substitutions

$$D = \exp\left(-n\ln\sqrt{(x_0-x)^2+\Gamma^2}\right), \tag{2.18a}$$

$$K = -n\cdot\mathrm{Angle}(-\Gamma, x_0 - x). \tag{2.18b}$$

We also define

$$\mathrm{Angle}(-\Gamma, x_0 - x) = \arg\left[-\Gamma + i(x_0 - x)\right] = \begin{cases} \mathrm{Tan}^{-1}\left(\frac{-\Gamma}{x_0-x}\right), & x \le x_0 \\ \mathrm{Tan}^{-1}\left(\frac{-\Gamma}{x_0-x}\right) - \pi, & x > x_0 \end{cases}. \tag{2.19}$$

## 2.6 Electroluminescence (EL)

Since the diode samples used for several of the experiments described above resembled LED structures, electroluminescence (EL) experiments were also possible, in compliment to the photoluminescence experiments. Electroluminescence is directly analogous to PL, except electron-hole pairs are injected into the active region by forward biasing the diode and drawing a current. The spontaneous emission resulting from radiative recombination is collected by a lens, dispersed by a spectrometer, and detected by an InGaAs photodiode, as in the PL measurements. Phase-sensitive detection with a lock-in amplifier is used to reduce the noise in the measured spectra,

and is accomplished by pulsing the current source (at 307 Hz) with a 50% duty cycle square wave. The setup is similar to that shown in Fig. 2.2 for PL, but with the pulsed current supplied by an ILX Lightwave LDC-3722 operated in high bandwidth current drive mode and modulated by an HP 33120A function generator.

The physics of EL is similar to that of PL (see Section 2.3.2), since both involve spontaneous emission. However, band-filling may become more significant in EL since the diode is forward biased, though at low current densities band-filling can be minimized.

## 2.7 Cryostat for Low-Temperature and Temperature-Dependent Measurements

A liquid helium cryostat was incorporated into the experimental setups to allow low-temperature and temperature-dependent measurements of photoluminescence, photoluminescence excitation, electroluminescence, photocurrent, electroreflectance, and electroabsorption. The sample stage for variable-temperature measurements consisted of a modified Cryo Industries CSM-1161-C liquid helium flow cryostat mounted on an X-Y-Z stage. The entire stage could also be rotated about a vertical axis to orient the sample angle with respect to the surrounding optics. A picture of the cryostat on the motion control stage is shown in Fig. 2.7. The cryostat cold finger had a 1 cm hole bored through it for transmission measurements, and 2.5 cm diameter quartz windows on the casing provided optical access to the sample. The windows were measured to have broadband absorption of ∼9% from 1000–1800 nm (see Fig. 2.8).

Modifications were made to incorporate a 10-conductor electrical feedthrough on the cryostat, including a socket that attached to a specially-designed sample holder, for gaining access to device electrical pads during low-temperature testing in vacuum.

Figure 2.7: (Color) Photograph of the modified liquid helium flow cryostat used as the sample stage for variable-temperature measurements.

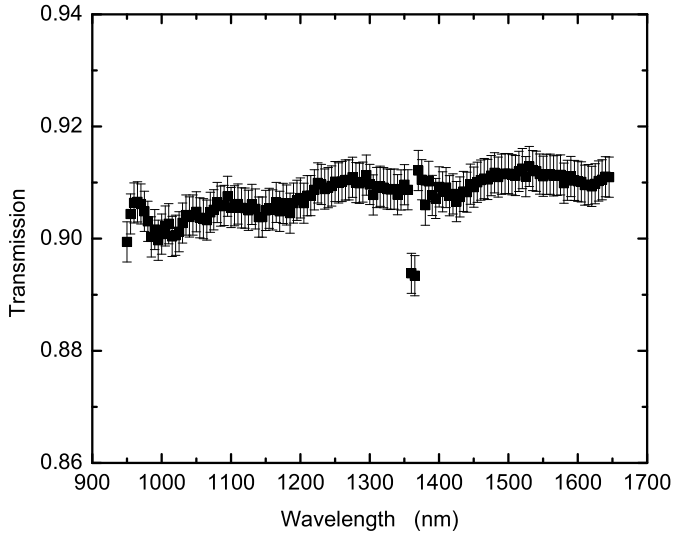


Figure 2.8: Transmission spectrum of the cryostat window glass.

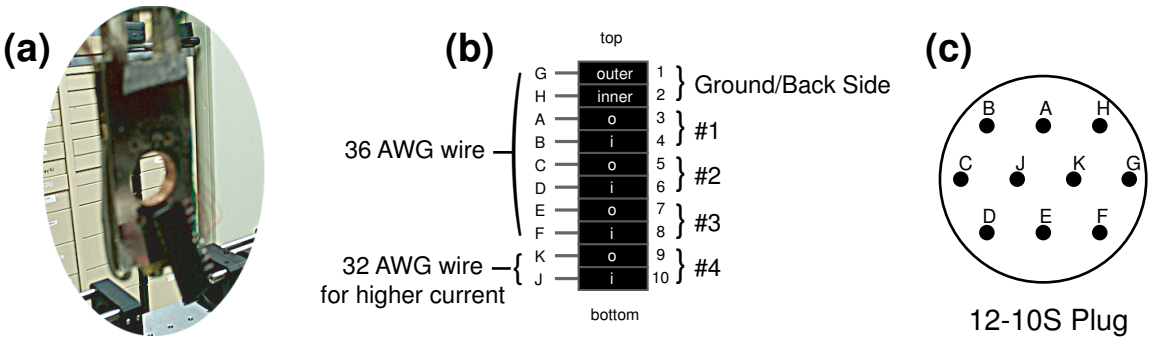


Figure 2.9: (a) Photograph of chip socket on the cryostat cold finger. (b) Diagram of chip socket connections to 12-10S receptacle, with letters A–H corresponding to labels on receptacle, as shown in (c). The labels "#1," "#2," etc. refer to the sample labels in Fig. 2.10 and "o" and "i" refer to the outer and inner conductors, respectively, of the BNC connectors of the biasing cable.

The modifications and sample holder are described in detail below.

The electrical feedthrough was provided to the cryostat with a 12-10S 10-pin receptacle mounted on the housing. Magnet wire of 36 (and 32) AWG was run from the receptacle down to a plastic header connector near the cold finger. Such thin wire was used to avoid excessive heat conduction to the sample from the outside world through these wires. Care was also taken to avoid having any parts make direct contact with the outer shell of the cryostat, to further prevent heat conduction to the sample, which would limit the lowest attainable stable temperature. A biasing cable was constructed to connect to the receptacle on the cryostat using an Amphenol MS3116F12-10S stain-relief socket connector on one end and five BNC connectors on the other. The BNC connectors corresponded to pairs of wires running down to the sample, which connected to individual devices, for example. A schematic of the wiring is shown in Figs. 2.9 and 2.10.

A special sample holder, shown in Fig. 2.10, was also constructed that mounts on the cryostat cold finger and connects to the electrical feedthrough. The sample holder

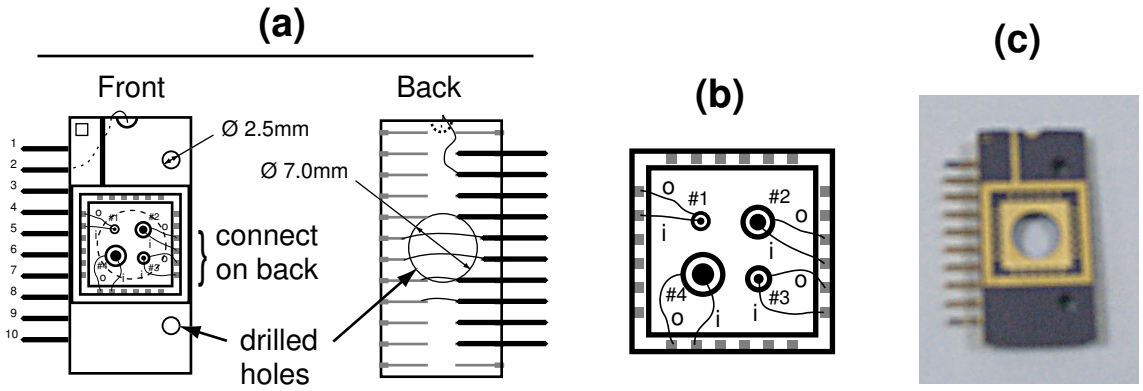


Figure 2.10: (a) Schematic of cryostat sample holder constructed from Spectrum Semiconductor CSB02442 24-pin side-brazed ceramic dual-inline chip package. (b) Close-up of sample wire-bonding onto sample holder. The labels "o" and "i" refer to the outer and inner ring contacts, respectively, on each device, which also correspond to the outer and inner conductors of the external BNC connectors of the biasing cable. The devices labeled "#1," "#2," "#3," and "#4" have aperture diameters of 250, 500, 750, and 1000 $\mu$m, respectively. (c) Photograph of sample holder (before sample bonding).

was constructed from a standard 24-pin side-brazed ceramic dual-inline semiconductor package (Spectrum Semiconductor CSB02442) with a 7 mm diameter hole drilled through the center to allow transmission measurements to be made. Two smaller holes (2.5 mm diameter) were drilled through the package on one side to allow mounting onto the cold finger with screws. Ten header pins were soldered onto the central 10 pins of the package on the opposite side from the mounting holes to interface with the socket (the mounting holes break 2 connections inside the package body on the side opposite the pins). Connections were made on the back using 36 AWG magnet wire, as shown in Fig. 2.10(a), to allow all necessary electrical contacts to be made from one side of the package.

Processed diode samples were epoxied into the package using two dots of epoxy on opposite corners to allow for strain relief from differences in thermal expansion of the wafer and package, and the devices were wire-bonded into the package as shown in the Fig. 2.10. Either of two epoxies was used, both suitable for cryogenic use: STYCAST 2850-FT/Catalyst 9 (Emerson & Cuming) for high thermal and low electrical conductivity, or ECCOBOND CT 5047-2 A/B (Emerson & Cuming) for high thermal and high electrical conductivity. The final packaged samples are mounted quickly onto the cold finger and attached to the external electrical cable by plugging in the header connector described above. Very rapid and reliable sample exchange was enabled in this fashion. Additionally, thermal contact to the cold finger was very good, and negligible temperature difference was measured between the sample and the thermocouple on the cold finger.

The temperature of the cold finger was controlled with a Conductus LTC-10 temperature controller. The temperature could be stabilized to better than 0.02 K. Calibration of the absolute temperature reading was performed by comparing the temperature variation of an undoped GaAs wafer with published data, and was found to read up to $\sim$5 K too high at low temperatures (e.g., for a real temperature of 10 K,

the controller reads about 15 K), but was much more accurate at higher temperatures. Temperature monitoring and control, as well as all other aspects of the measurement system, were automated by computer using LabVIEW software.

# Chapter 3

# *Ab Initio* Band Structure Calculations

This chapter details the methods used for *ab initio* density function theory calculations of the atomic structure and band structure of GaInNAs. The first section describes the computational methods, while subsequent sections expound on the results of band structure and total energy calculations. Density of states calculations are also mentioned that were used for the analysis of x-ray absorption (XAS) and x-ray emission (XES) measurements, although the bulk of that discussion is left for Chapter 4, which deals with the x-ray spectroscopy experiments.

## 3.1 Computational Methods

*Ab initio* calculations were performed using the Vienna *Ab Initio* Simulation Package (VASP) [72–75], which is based on the Kohn-Sham density-functional theory (DFT) using a plane-wave basis set [76]. All calculations involved static (0 K) crystal structures, as opposed to molecular dynamics simulations which study the motion of atoms at finite temperature. In the static case, only the motion of electrons need be considered. In essence, DFT allows recasting of the potential energy terms in the

many-electron Schrödinger equation as functionals of a ground state electron density. Then, solution of the many-electron Schrödinger equation is possible using an exactly equivalent set of independent one-electron equations. In the formulation, the interaction of the electrons with the ionic cores of the atoms is treated with the use of pseudopotentials, which replace the potential within a small cutoff radius around the atom center with an effective potential that exactly reproduces the scattering properties of the core in the region outside of the cutoff radius. The core is defined to include a number of the inner electrons of the atom, so that only a relatively small number of *valence* electrons are included in the solution of the Schrödinger equation. Various formulations for the construction of pseudopotentials have been devised [77]. In this work, ultrasoft (Vanderbilt) pseudopotentials [78] were employed, using the local density approximation [79] of Ceperley and Alder [80] for the exchange-correlation functional as parameterized by Perdew and Zunger [81]. The atomic potentials were generated using theoretical calculations on atoms, without fitting to experimental properties. The pseudopotentials used for Ga, As, In, and N, respectively, included 3 ($4s^2 4p^1$), 5 ($4s^2 4p^3$), 3 ($5s^2 5p^1$), and 5 ($2s^2 2p^3$) valence electrons. Treating the $3d$ electrons of Ga and the $4d$ electrons of In as valence often is required for accurate calculations, but was found not to be necessary for these calculations and omitting them saved considerable computational time (overall, 45,000 cpu-hours of compute time was used to perform the calculations described in this dissertation). Treating the $d$ electrons as valence is ordinarily very important for calculations of nitrides (e.g., GaN) because of strong overlap with the small, electronegative N atom, but since the interatomic spacings in GaInNAs are much larger than in the binary nitrides, the $d$-electron interactions with N are minimized. The pseudopotentials used were validated by running test calculations on the binary compounds. The elastic and electronic properties of GaAs were particularly well reproduced, using both the primitive unit cell and a 64-atom cubic supercell. Further detail on density functional theory,

the local density approximation, pseudopotential theory, and solution methods for the Kohn-Sham equations is found in the excellent primer of Ref. [77].

Total energy calculations were used to determine the equilibrium atomic configurations and analyze the thermodynamic stabilities of the different configurations. Partial local density of states (PLDOS) calculations were used to simulate x-ray absorption and emission spectra. Band structure calculations, including orbital-decomposed band structures or so-called "fat bands," were used to examine general features of the electronic and optical properties of the material, as functions of nitrogen composition, nearest neighbor structure, and clustering.

The following subsections describe the technical details of each type of simulation performed, while the remainder of the chapter discusses the results. However, the results of much of the density of states calculations, which were used primarily to analyze x-ray absorption data, are discussed fully in Chapter 4.

All calculations were performed on IBM parallel supercomputers at the San Diego Supercomputer Center at the University of California in San Diego (BlueHorizon, IBM SP3) and the Texas Advanced Computing Center at the University of Texas in Austin (Longhorn, IBM SP4) through the National Partnership for Advanced Computing Infrastructure, using an optimized parallel (MPI) version of the VASP code. Post-processing of the results was performed using self-developed code on a personal computer. Appendix A includes details of the VASP input files used for the various simulations, as well as discussion of some of the technical issues which are beyond the scope of the discussion here.

### 3.1.1 Total Energy and Relaxation Calculations

Supercells consisting of 64 atoms were used to simulate $Ga_{1-x}In_xN_yAs_{1-y}$ with $x \sim 0.25$–$0.30$ (8–10 In atoms) and $y \sim 0.03$ (1 N atom). The bulk crystal structure is nominally alloyed zinc blende, which has cubic symmetry. The supercell is constructed from 2

$\times$ 2 $\times$ 2 cubic GaAs unit cells, with the appropriate number of In atoms randomly substituted for Ga. A single As atom is replaced by N to model a 3% N concentration (per Group V atoms). Multiple models were constructed with the N atom placed on an As site with differing number of In nearest neighbors, from 0 to 3. These idealized model structures are heretofore referred to as "GaInNAs$^{(n)}$," where $n$ indicates the number of In nearest neighbors to the N atom (e.g., GaInNAs$^{(0)}$ indicates a model crystal where every N atom is bonded to 4 Ga atoms). Additional 128-atom models were constructed to examine lower N concentration and N clustering effects, by starting with 2 $\times$ 2 $\times$ 4 GaAs unit cells. These structures are described in more detail in Section 3.2.3 below, when discussing the results of these calculations.

Direct comparison among the models was made possible by fixing the positions of the In and Ga atoms in all models, so that the only difference between them was the N bonding (aside from the relaxed lattice constant discussed below). Only a single model was constructed for each GaInNAs$^{(n)}$. Further refinement of the calculations could have included the construction of a set of models for each $n$ with different random configurations of the In atoms. Then, repeating the calculations over the set for each $n$ to obtain an average result would address the issue of randomness of the alloy, within the atomistic *ab initio* simulation approach. However, a previous study has shown these effects to be small [82]. Moreover, we show below that local interactions of the N atom and its nearest neighbors dominate the properties of the models.

The first calculation required is a relaxation of the atomic positions within each model to determine the minimum total energy configuration. All subsequent calculations of material properties rely on having model structures that represent the most stable configuration of the atoms. Since there is more than one type of Group III and Group V atom arranged randomly in the crystal, and especially because N is such a relatively small atom, the atomic relaxations result in some atoms being moved off

of lattice sites, breaking the perfect symmetries of the zinc blende structure. The details of these localized atomic motions prove quite significant in understanding the unique properties of GaInNAs.

In addition to relaxing the atomic positions within the supercell, the size and shape of the cell also needs to be relaxed. One could choose an experimentally determined lattice constant for the cell dimensions, however, certain inaccuracies in the pseudopotentials and the high sensitivity of calculated properties on the interatomic distances require that the cell dimensions be relaxed to their minimum energy values within the parameters of the pseudopotentials used. For bulk (unstrained) calculations, a cubic unit cell was enforced to mimic the known cubic symmetry of the crystal, and a single-parameter cell dimension was relaxed. For strained (thin film) calculations, a tetragonal unit cell was used to account for the biaxial strain imposed by growing GaInNAs pseudomorphically on GaAs. In that case, the two in-plane cell parameters were fixed at the value for GaAs (determined from supercell calculations using the same Ga and As pseudopotentials as used in the GaInNAs calculations), and the third dimension was allowed to relax. In both cases, all cell angles were fixed at 90°. A two-step relaxation was used to separately relax the atomic coordinates and the cell dimensions, which was found to be a more efficient approach than performing a single relaxation of all degrees of freedom; the resulting structures were the same from both approaches.

To ensure accuracy in subsequent calculations, relaxations were performed to a high degree of convergence. Ionic relaxations were continued until the Hellman-Feynman forces on all atoms were below 0.01 eV/Å and the total energy was converged to less than $1\times10^{-5}$ eV. For relaxations, a 3×3×3 Monkhorst-Pack [83] $k$-point mesh (14 $k$ points) was found to be sufficient. Dense $k$-point sampling is not required for this type of calculation, particularly for a semiconducting system and such a large

supercell. The plane wave cutoff energy was 26 Ry. The number of empty bands included in the calculation was 140. To save computational time, the perfect zinc blende starting structures were pre-relaxed using a classical forcefield [84–87] to provide the initial structures for the *ab initio* relaxations in VASP.

### 3.1.2 Density of States Calculations

Density of states (DOS) calculations were performed using the relaxed model structures after performing a single-point total energy calculation to generate a high-quality self-consistent charge density using a dense 6×6×6 Monkhorst-Pack $k$-point mesh (108 $k$ points). Significant improvement in the smoothness of the resulting DOS was found compared to using a 3×3×3 mesh. Tests using an 8×8×8 mesh (256 $k$ points) showed further marginal improvement in the accuracy of the DOS, but the significant increase in computational cost did not justify its use. For a slight increase in the accuracy of DOS, and more importantly to probe several eV into the conduction band, 172 empty bands were used in the calculation. A standard electronic energy convergence of $1\times10^{-4}$ eV was sufficient. The plane-wave cutoff was kept at 26 Ry.

Partial local density of states (PLDOS) calculations, which give the atom- and orbital-projected DOS (for example, the $4p$ DOS from a particular Ga atom), were accomplished by projecting the calculated wavefunctions onto spherical harmonics within a specified atomic radius for each atom. The choice of the atomic radii is somewhat ambiguous for a system with more than one element [88]. One possible choice, following the tradition of atomic sphere calculations, is to set the radii so that the overlap between spheres is minimized while the total volume equals the cell volume. We have chosen an alternative approach of simply scaling the tabulated values of covalent radius [89] for each element so that the total volume of all the spheres equals the cell volume. With this approach, all atoms of a given element are

assigned the same atomic radius. The former approach does not guarantee this. In any case, tests were performed that showed very little sensitivity of the shape of the PLDOS to the chosen atomic radii.

### 3.1.3 Band Structure Calculations

Band structure calculations continue from the high-quality charge density generated by the density of states calculation. To calculate the eigenenergies along high symmetry lines through the Brillouin zone, the charge density was kept fixed and a non-self-consistent calculation was performed using 51 $k$-points spanning the $X$, $\Gamma$, $L$, and $K$ points (of the cubic supercell). As for the DOS calculations, a plane-wave cutoff of 26 Ry was used, 172 empty bands were included, and the electronic energy was converged to $1\times10^{-4}$ eV.

Orbital-projected band structures ("fat bands") were generated using the same spherical harmonic projector scheme described above for PLDOS [90]. Individual atom contributions to the bands were also analyzed in the same way. The fat band structures shown in this dissertation are plotted to show the maximum contribution to the bands from each element, offsetting the weighting from the number of atoms of each element in the supercell.

### 3.1.4 Band Offset Calculations

Accurate band offsets between two structures are calculated by forming a supercell consisting of the original two supercells joined at an interface (effectively forming alternating slabs of the two materials) and using the method of Van de Walle [91]. The method consists of optionally relaxing the atoms at the interface, then calculating the local potential throughout the interface supercell, and plotting the local potential across the interface, integrated in the other two directions. Matching the local

potentials calculated in the two original supercells to their respective regions of the interface cell gives a relative offset that is added to the difference between the valence band edges calculated from the band structures of the original cells. Essentially, the average local potential in each material is used as a reference energy to correct the absolute energies of the valence band edges.

In practice, for most of the calculations presented in this dissertation, the difference between structures was so small (the position of one N and one As atom being swapped) that band offsets could be approximated directly from the eigenvalues of the band structure calculations, and the computationally expensive calculation described above could be neglected as a small correction. In cases where the correction had potential significance, the offsets were checked with the full interface calculation.

## 3.2 Simulation Results

### 3.2.1 Atomic Structure Relaxation and Total Energy

Since GaInNAs is nominally a zinc blende random alloy, the Group III elements (Ga and In) share a face-centered cubic (FCC) lattice, and the Group V elements (As and N) share a second interpenetrating FCC lattice offset by a bond length along the cube diagonal. Each atom sits in the center of a tetrahedron, bonded to 4 atoms from the opposite group; particularly, each N atom is bonded to a total of 4 Ga and/or In nearest neighbor atoms, as shown in Fig. 3.1. The ratio of In:Ga atoms surrounding N defines its chemical environment. If the arrangement of atoms in the alloy were random, then the probability distribution for finding a given number of In atoms surrounding any Group V atom (e.g., N) in an alloy with 31% In (relative to Group III atoms) is shown in Fig. 3.2. The most probable arrangement has one In atom bonded to any Group V atom.

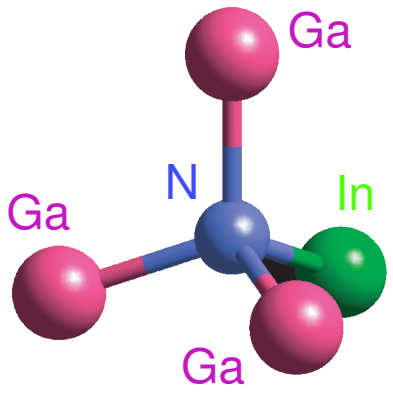


Figure 3.1: (Color) The chemical environment around N is characterized by the ratio of Ga:In nearest neighbors. The particular configuration shown, with one In atom bonded directly to N, corresponds to the GaInNAs$^{(1)}$ model structure.

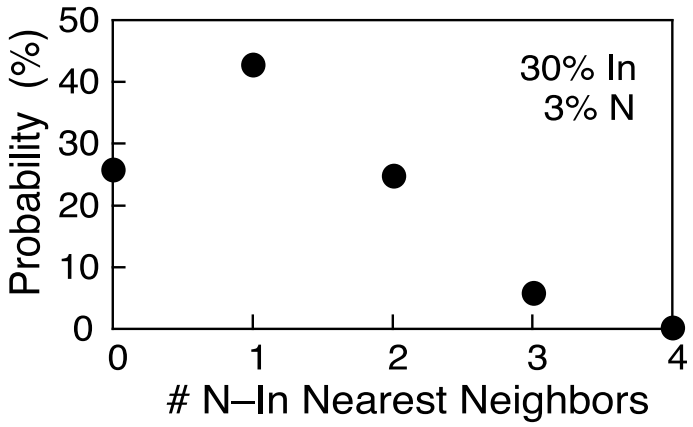


Figure 3.2: The probability of finding a given number of In nearest neighbors to any Group V atom is plotted for a random alloy with 31% In.

The results of the total energy relaxations of the GaInNAs$^{(n)}$ models are shown in Fig. 3.3, where the total energy and equilibrium lattice constant of the relaxed structures is plotted as a function of $n$, or the number of N–In nearest neighbors. The lattice constant reported is referenced to the GaAs cubic unit cell and so is half the supercell dimension from the calculations. The figure shows a decrease in total energy by >10 kcal/mol when 2 or more In atoms are bonded to N, despite a slight increase in lattice constant leading to a slight increase in compressive strain energy when growing GaInNAs epitaxially on GaAs. The decrease in chemical energy with increasing number of N–In bonds is due to overall decreases in individual bond strains, since the large lattice parameter of GaInNAs (near that of GaAs) stretches the longer N–In bond less from equilibrium than the N–Ga bond. (An equivalent interpretation is that the small N atom can couple with the large In atom to offset, on average, their atomic size mismatches within the GaAs host crystal.) The equilibrium bond length in GaN was calculated as 1.93 Å, while in InN it was 2.14 Å. The relaxed bond lengths in GaInNAs range from 1.95 to 2.02 Å for Ga–N and from 2.19 to 2.24 Å for In–N, with shorter bond lengths corresponding to structures with increased number of N–In nearest neighbors. As $n$ increases, the first nearest neighbor shell around N relaxes inward significantly, approaching the bond lengths of the binary compounds, but never quite achieving them. The nearest neighbor bond strain is greatest for GaInNAs$^{(0)}$, at 4.5% and 4.8% for Ga–N and In–N, respectively. For GaInNAs$^{(3)}$, the bonds are strained only 1.0% and 2.4%, respectively. We note that increasing the number of In nearest neighbors to N relieves bond strain to both Ga and In atoms. The second nearest neighbor shell relaxes inward as well, but to a much lesser extent than the first nearest neighbors. Beyond the second shell, atomic relaxations are minimal. For all models, the relaxation of the N nearest neighbors occurs symmetrically, weighted by the atom type (i.e., all Ga–N nearest neighbor bond lengths are the same, and similarly for all the In–N bond lengths).

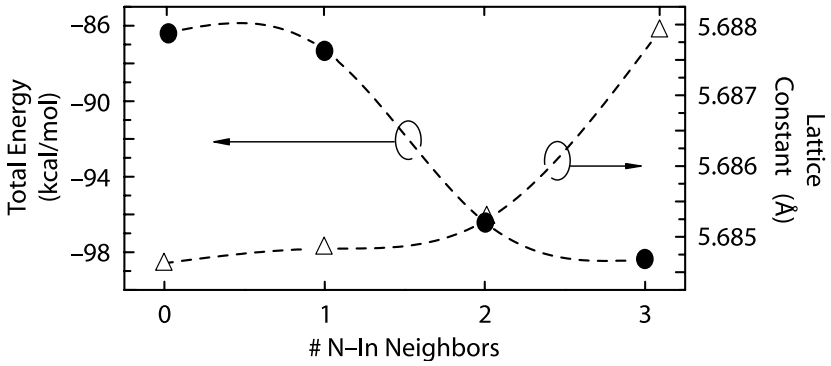


Figure 3.3: The variation of lattice constant and total energy calculated for bulk $Ga_{0.69}In_{0.31}N_{0.03}As_{0.97}$ as a function of N chemical environment.

The significantly lower total energy for structures with higher N–In coordinations shown in Fig. 3.3 has an important implication, namely, that a thermodynamic driving force exists for increasing $n$. Referring back to Fig. 3.2, we see that the most stable structure thermodynamically does not correspond to the most probable configuration ($n = 1$) in a random GaInNAs alloy of this composition.

### 3.2.2 Band Structure

Band structure calculations reveal some insight into general properties of the GaInNAs material system, as well as elucidate fundamental physics about the anomalous band gap bowing in the dilute-nitride arsenides. The results also extend to understanding the nature of the band gap shift during annealing. The most fundamental result of the band structure calculations is the prediction of an increased band gap with increasing degree of N–In bonding in the crystal. The calculated band structures for the bulk GaNAs and $GaInNAs^{(n)}$ models are shown in Figs. 3.4 and 3.5. Spin-orbit coupling was not included in these calculations.

A general feature that is evident in the figures is a severe underestimate of the

band gap resulting from use of the LDA approximation [92]. The underestimate occurs mostly in the conduction band and arises from the fact that DFT-LDA is essentially a ground state calculation. The energy of the ground state depends only on the energies of the occupied states, so excited states are not treated properly. Specifically, the absence of nonlocal interactions in the LDA exchange-correlation potential leads to underestimated excited state energies. Remarkably, however, for a wide range of systems, the computed excited state energies from DFT-LDA have nearly the correct energy spacings and only the band gap is underestimated [92]. Thus, one can often employ the so-called "scissors operator," which rigidly shifts all conduction bands up by a fixed empirical value, to correct the excited state energies.

A somewhat better correction of the excited state energies is obtained by employing generalized density functional theory (GDFT) [93, 94]. The GDFT approach corrects the excited state energies using only the wavefunctions and other quantities (exchange-correlation energy and potential) already computed by ordinary DFT-LDA calculations, via [93]

$$\Delta_{fi} = \int \left[ 2\overline{\epsilon}^{(0)}_{\mathrm{XC}}(\mathbf{r}) - V^{(0)}_{\mathrm{XC}}(\mathbf{r}) \right] \left[ |\psi_f(\mathbf{r})|^2 - |\psi_i(\mathbf{r})|^2 \right] d^3r, \tag{3.1}$$

where $\Delta_{fi}$ is the correction energy between single-particle states $\psi_i$ and $\psi_f$ across the band gap, $\overline{\epsilon}^{(0)}_{\mathrm{XC}}$ is the average ground state exchange-correlation energy, and $V^{(0)}_{\mathrm{XC}}$ is the ground state exchange-correlation potential. Thus, very little additional computational cost is associated with the GDFT correction of the band gap. Furthermore, improvement is also made to the dispersion of the conduction bands. A more detailed description of the GDFT formalism is beyond the present discussion, but the reader is referred to Refs. [93, 94] for a complete treatment.

Another approach to improve the excited state energies of DFT-LDA that is based more on the physical principles of the excitation, but that also does not require much

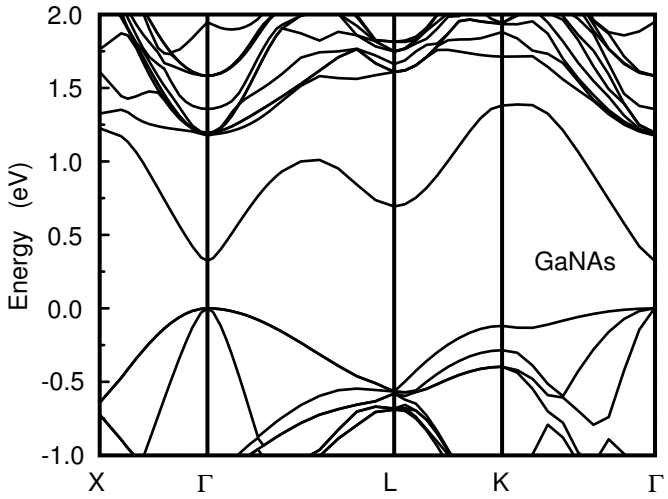


Figure 3.4: Calculated band structure for bulk $GaN_{0.03}As_{0.97}$.

additional computational effort, is the LDA+U method [95–98]. LDA+U introduces an on-site Coulomb interaction at the core of the excited atom to simulate the excess charge associated with the generation of a core hole when exciting an electron into the conduction band. Little difference in the calculated band structures is expected since others have shown, using a full-potential linearized-augmented-plane-wave method [99], that the presence of a core hole does not significantly affect the valence and conduction bands of GaNAs, but mainly modifies the core states [100]. There may be merit, however, in repeating some of the calculations presented here using LDA+U, which recently has been implemented in VASP, for comparison of the results. Various other, significantly more computationally expensive, methods may also be used to calculate the band gap more accurately, for example, the GW method [92].

In any case, the band structures calculated using DFT-LDA and shown in Figs. 3.4 and 3.5 can be assumed to be reasonably accurate, modulo an approximately constant shift of the unoccupied bands upward to correct for the underestimated band gap. The energy separations calculated between unoccupied bands can be taken to be accurate

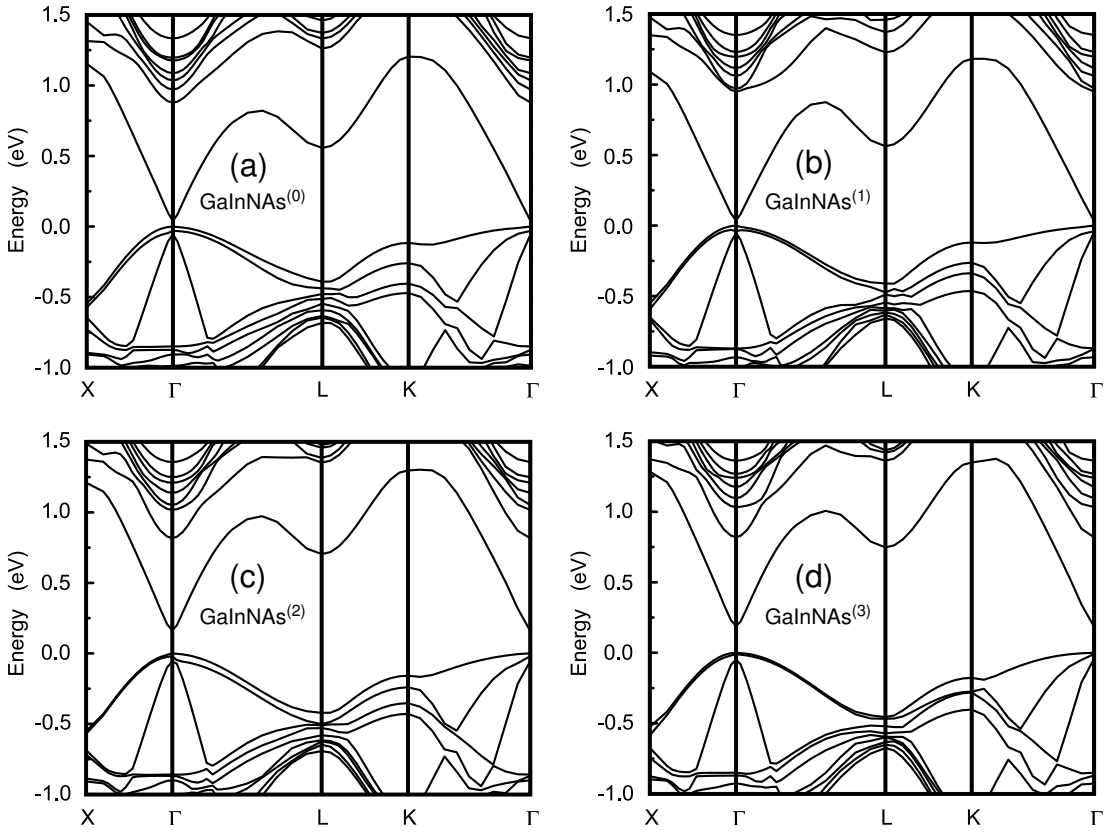


Figure 3.5: Calculated band structure for bulk $Ga_{0.69}In_{0.31}N_{0.03}As_{0.97}$ models with (a) 0, (b) 1, (c) 2, and (d) 3 In nearest neighbors to N.

to within at least approximately 10% or so. We will also consider the dispersion of the conduction band to be reasonably correct, with possible improvement using GDFT. Thus, whether or not an explicit band gap correction is applied, we can accurately compare relative energies (i.e., band gaps) between the models.

The variation of band gap for the GaInNAs$^{(n)}$ models as a function of the number of N–In nearest neighbors extracted from the calculations is plotted in Fig. 3.6. The band gap varies appreciably (up to 150 meV) from the local atomic reconfiguration (N nearest neighbors), with a higher band gap associated with increased N–In bonding. The increase in band gap of up to 150 meV through this mechanism alone is enough for a wavelength shift from 1550 nm to 1300 nm, if annealing changes the atomic configuration. In practice, the observed wavelength shifts are smaller than this amount, and a typical shift of 100–150 nm can be explained even considering some averaged rearrangement within the strict limits. The higher band gap states correspond to thermodynamically preferred configurations, but they are least likely to occur in a purely random alloy, as already discussed and shown in Figs. 3.3 and 3.2. A theory linking the observed blueshift in GaInNAs band gap upon annealing with a thermodynamically-driven rearrangement of atoms toward increased N–In bonding, perhaps with as-grown material having a random configuration, is probable. Much of the remainder of this thesis presents experimental and further theoretical evidence that this indeed is the case.

The calculated band structures also reveal interesting general electronic properties of these materials. The lowest conduction band shows quite a bit of dispersion ($\sim$1 eV bandwidth). Effective masses can be extracted by fitting the curvature of the band minima to parabolas. We find a relatively heavy electron effective mass ($m_{\mathrm{e}}^*$) of 0.07 $m_0$ for GaInNAs with 31% In and 1.5% N, increasing to 0.09 $m_0$ for 3.1% N, consistent with experimental observations. These values correspond to a 25% increase in $m_{\mathrm{e}}^*$ for a 1.5% change in N concentration. Reported experimental values for $m_{\mathrm{e}}^*$

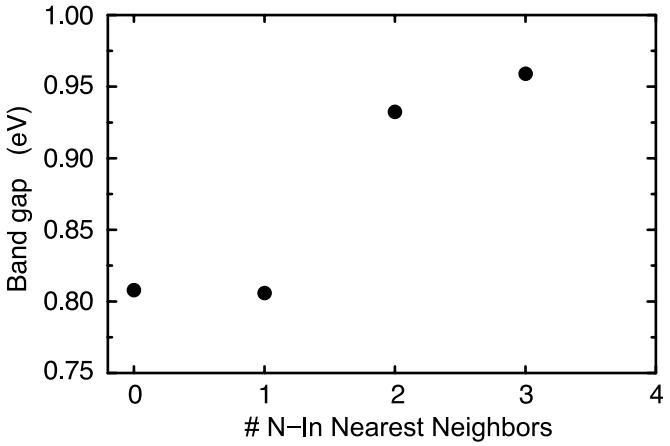


Figure 3.6: The calculated variation of bulk $Ga_{0.69}In_{0.31}N_{0.03}As_{0.97}$ band gap as a function of number of N–In nearest neighbors. The values of band gap have been corrected from the LDA approximation, which underestimates the gap.

span a wide gamut, but have recently converged on the range of 0.08–0.12 $m_0$ for 1–3% N, with generally smaller effective mass for smaller N concentrations [28, 101–105]. For comparison, the electron effective mass for $Ga_{0.69}In_{0.31}As$ is 0.052. The light hole (LH) mass in GaInNAs is found in the calculations to closely match the electron mass at $\sim$0.075 $m_0$ and is nearly insensitive to N concentration (at least between 1.5% and 3.1%). The LH mass for $Ga_{0.69}In_{0.31}As$ is 0.066. The heavy hole (HH) mass, however, cannot accurately be extracted from these band structure calculations, which yield $m^*_{\mathrm{HH}} \sim 1.0\ m_0$. A better approximation is probably obtained from the heavy hole mass of $Ga_{1-x}In_xAs$ (e.g., 0.375 for $x = 0.31$). An additional important conduction band with significant dispersion is seen in Fig. 3.5, $\sim$0.7 eV above the lowest conduction band. We will show below that this band corresponds to the original GaInAs matrix conduction band, but made much heavier by the introduction of N. In contrast to the behavior of the lowest conduction band, the mass of the second conduction band is inversely dependent on the N concentration, in proportion to the increase in mass of the lowest conduction band. For example, the calculations reveal

$m^*_{e2} = 0.37\ m_0$ for 1.5% N and $m^*_{e2} = 0.28\ m_0$ for 3.1% N, a reduction of 25% for a 1.5% increase in N content.

The values of effective mass from these band structure calculations are accurate to within ∼30%. The hole masses are the least accurate, since spin-orbit coupling has not been included in the calculation. Spin-orbit coupling will split the HH and LH bands away from $k = 0$ and give the light hole band extra curvature at $k = 0$, while also pushing the split-off hole (SOH) band to lower energies. However, it has been found that calculations not including spin-orbit coupling, the mass of the SOH (which is then degenerate with the HH/LH band at $k = 0$) closely approximates the true mass of the LH band when spin-orbit interactions are included. Thus, a good approximation of the LH mass is possible without including spin-orbit interactions. The HH mass is not accurately approximated. Furthermore, the bands are quite non-parabolic away from the minima and comparison with experimental values of effective mass can be complicated by this fact, since different experimental techniques probe the effective mass in different ways. For example, cyclotron resonance yields the effective band curvature a finite energy above the band minimum, while measurement techniques based on carrier transport are sensitive to a mass averaged over all directions for an electron with finite energy above the band minimum.

An interesting feature of the GaInNAs band structure (actually, the band structures of all the dilute-nitride arsenides, including GaInNAsSb) is that despite a small band gap, $m^*_e$ is large. This relationship is contrary to the Kane model, which predicts a proportionality between $m^*_e$ and band gap [106]. The explanation lies in the fact that the lowest conduction band in GaInNAs (the "N-band," as described below) mainly interacts with higher lying states to increase $m^*_e$, rather than interacting with lower-lying states across the gap (i.e., the valence band) which would lower $m^*_e$, as is the typical case for semiconductors [107].

The nature of the energy bands was elucidated through a "fat bands" analysis, where the band structure was decomposed into contributions from the various atomic orbitals [90]. Qualitatively, the band structure of GaInNAs and GaNAs (with relatively high N content greater than ∼1%) is similar to that of GaInAs (or GaAs), with a notable exception. Near Γ, a valence band rich in As-4$p$ states forms, and a conduction band rich in Ga-4$s$ and In-5$s$ states forms ∼1–1.5 eV higher in energy, as in GaAs/InGaAs (see Fig. 3.7). However, between these two bands, ∼0.7–1.0 eV below the conduction band, a new conduction band forms that is characterized by $s$-orbital interactions between N and its four nearest neighbors: the "N-band." The formation of the N-band occurs when the N concentration is high enough that semi-localized states within the host band gap interact through the electron density of the matrix to form a dispersive band of their own. The upper conduction band is dominated by Ga/In–As bonding spatially distant (>2 nearest neighbor shells) from the N atoms. In GaInNAs, with higher numbers of In atoms bond to N, an appreciable amount of In-5$s$ contribution from the upper conduction band shifts to the lower N-band, and the N-band simultaneously increases in energy (this is the increase in band gap with increasing numbers of N–In nearest neighbors that has already been presented).

Comparing the fat band structures calculated for 1.5% N (using a 128-atom supercell) to that for 3% N, increasing the N concentration is observed to shift the N-band lower into the host band gap, causing the sharp band gap reduction with addition of N in dilute-nitride arsenides. From 1.5% to 3.1% N, the band gap shrinks 0.022 eV at the Γ point, or ∼15 meV/%N. This rate of band gap lowering is appreciably lower than the experimentally observed value of 40–50 meV/%N because the LDA band gap underestimate causes excessive conduction band–valence band repulsion as the gap shrinks. Increasing the N concentrations also shifts N conduction charge density from higher energy states ($L$, $K$, and $X$ neighborhoods) to the band minimum (Γ neighborhood). Furthermore, increasing the N concentration lowers the $L$ valley

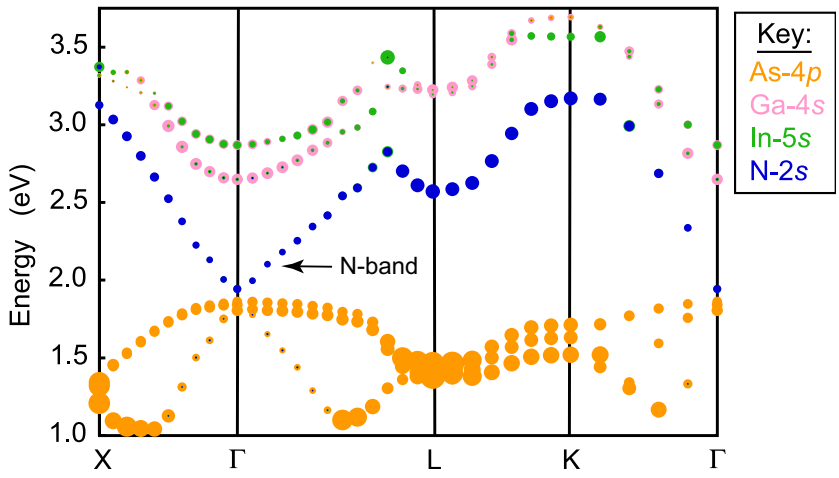


Figure 3.7: (Color) Fat band structure for bulk GaInNAs[(2)], with 3% N and 31% In (representative for GaInNAs), showing the maximum contribution of key orbitals to the bands. The size of each dot is proportional to the respective orbital contribution to each band. The "N-band" is dominated by bonding states between N and its four nearest neighbors. The band gap has not been corrected from the LDA approximation, and so appears underestimated. The correction would shift the conduction bands upwards nearly rigidly by ∼0.7–0.8 eV.

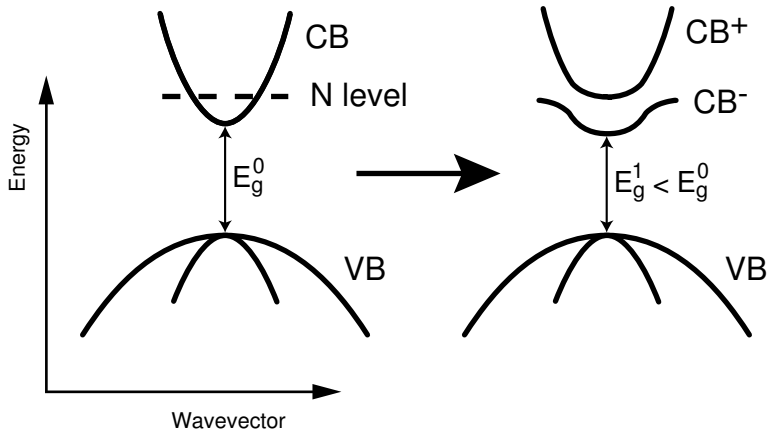


Figure 3.8: Schematic energy band diagram illustrating band anticrossing in very dilute nitride arsenides.

(∼0.16 eV from 1.5% N to 3.1% N) at a rate faster than the Γ valley is reduced. For 3% N, the $L$ valley lies ∼0.56 eV above the Γ valley minimum.

Early theory on the anomalous band gap lowering relied on a phenomenological band anticrossing (BAC) model [108]. The BAC model, illustrated in Fig. 3.8, asserts that discrete localized N states above the host conduction band interact with the conduction band, causing an anticrossing due to the flat dispersion of the localized states. The N states are predicted to exist above the conduction band from calculations of the atomic energy states of the N impurity atom, relative to the electron affinity of the host crystal. The band anticrossing results in a lowering of the conduction band and also an increase in the electron effective mass from reduced curvature due to the interaction. The BAC model predicts an upper conduction band due to N that lies several tenths of eV (depending on composition) above the modified host conduction band, although quantitation is accomplished by fitting to experimental data. The model was originally formulated for the very dilute limit of N concentration (less than ∼1% N), where interactions between N atoms is negligible.

Photoluminescence measurements on very dilute GaNAs show a spectrum of discrete N pair states that exist within the band gap of GaAs, close to the conduction band edge [109–112]. Calculations using the one-band one-site Koster-Slater model show these states to be associated with various N atom pairs having separations less than on the order of 1 nm [113]. Even in the very dilute limit, these N cluster states can interact with the GaAs conduction band to lower the band gap via the formation of an impurity band [111]. In the very dilute limit, the impurity band continues to retain certain localization characteristics, however. With a N concentration near 3%, the average distance between randomly incorporated N atoms is 1.1–1.3 nm. At these more concentrated levels, the N atoms interact quite strongly and form the highly-dispersive N-band shown in Fig. 3.7. In this case, the *lower* conduction band has N character, while the *upper* band retains the nature of the host crystal. (There still may exist a third band originating from the N impurity states above the host conduction band, as above.)

Thus, a complete model of the band gap lowering and nature of the band structure for Ga(In)NAs should incorporate both the BAC model which deals with N impurity states above the conduction band and also the existence of N cluster states distributed within the band gap. This revised model is illustrated in Fig. 3.9. In the very dilute limit, BAC is probably the dominant effect, but as the N concentration is increased, N pair states within the gap become increasingly significant and begin to form a sub-gap impurity band, adding a second mechanism for band gap lowering. At the highest concentrations of N (2–4%, which approach the solubility limit), the N-band that forms from N–N long-range interactions dominates the optical properties. The fat band structure calculations show that the band gap lowering at least from 1.5% to 3.1% N is dominated by the N-band. The crossover point for the formation of the N-band is probably around 1% N or less, and it is possible that a kink in the band gap bowing occurs near this crossover point, although such a kink may be below

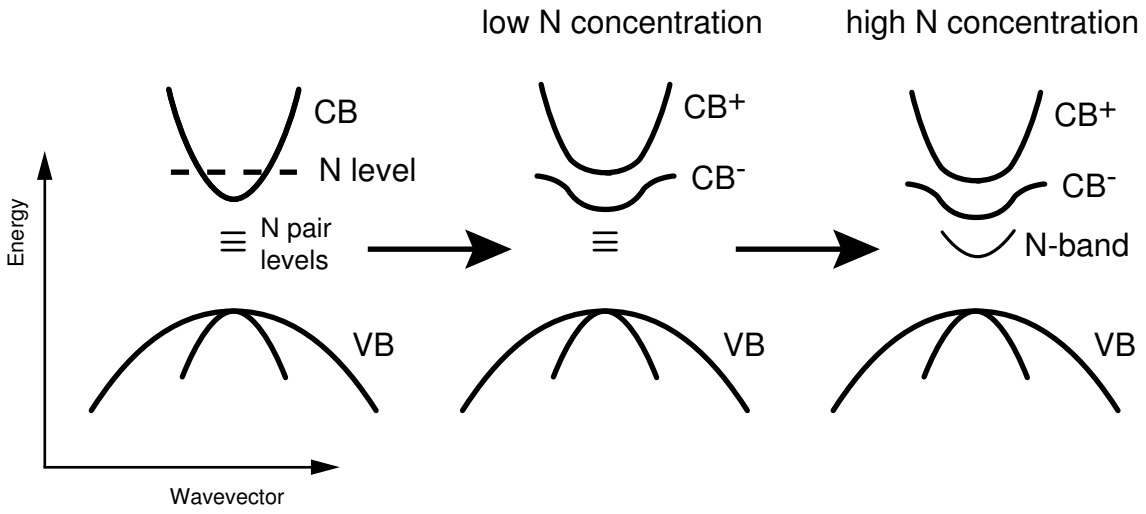


Figure 3.9: The complete model of band gap narrowing in dilute-nitride arsenides includes the formation of a N-band at higher N concentrations, from sub-gap states due to N pair interactions. The illustration does not include the additional, finer-scale effect of N nearest neighbor band splitting.

the detection limit of experimental determinations of the band gap. For GaNAs, a localized to delocalized transition was theoretically predicted to occur at ∼0.6% N where cluster states in the gap are overtaken by a downwards moving conduction band edge [114, 115].

For GaInNAs (compared to GaNAs), in addition to the band gap lowering due to N incorporation, there is the additional issue of the N–In nearest neighbor states which form a fine-splitting of the conduction band, and may modify the energy position of the band edge quite significantly through local atomic rearrangements (for example, during annealing). The modification of the conduction band edge may change the number of sub-gap N cluster states which remain in the gap. The nearest neighbor rearrangement also affects the valence band edge, but to a much lesser extent, which is practically negligible.

### 3.2.3 Nitrogen Clustering Effects

In addition to the long-range N clustering effect described above involving the sub-gap N pair states, there are additional clustering effects of N second nearest neighbor pairs in GaInNAs, which can be important considering the high N compositions of technologically important material. To study these effects, DFT calculations were performed on 128-atom N second nearest neighbor cluster models. The models were constructed to contain nominally 3% N, like the 64-atom GaInNAs$^{(n)}$ models, but had the two N atoms arranged to form a second nearest neighbor cluster. Two types of cluster models were constructed: one with a "bridging" In atom and the other with a "bridging" Ga atom. In the "In bridge" model, the bonding arrangement around the cluster was ($GaIn_2$)N–In–N($InGa_2$), while in the "Ga bridge" model, the bonding arrangement was ($GaIn_2$)N–Ga–N($In_2Ga$). The clusters were constructed to maintain a GaInNAs$^{(2)}$ configuration around the N atoms as much as possible without changing the total numbers of each atom type in the cluster. The atomic structures corresponding to these two arrangements are shown schematically in Fig. 3.10. Except in the vicinity of the cluster, both 64-atom halves of the cluster models were identical, with the remaining atoms randomized within the supercell. To allow comparison to the calculations performed on the 64-atom supercells, the arrangement of atoms more than two atomic shells away from the N cluster was kept identical to that used in the 64-atom models. Atomic relaxations were performed on the cluster models for the atoms within two atomic shells of the cluster core (a total of 33 atoms). The resulting total energies predict that the "In bridge" (N–In–N) cluster is thermodynamically favored over the "Ga bridge" (N–Ga–N) cluster by $\sim$7 kcal/mol, or 60% of the energy difference between GaInNAs$^{(0)}$ and GaInNAs$^{(3)}$.

Figure 3.11 shows the fat band structure calculated for the "In bridge" N second nearest neighbor cluster model. The appearance of a second, higher energy N-band is apparent. This second N-band has a relatively flat dispersion, particularly from $\Gamma$

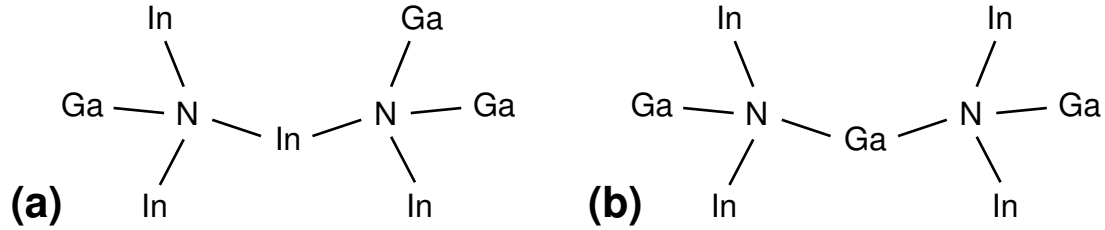


Figure 3.10: Schematic of the atomic arrangements in the (a) "In bridge" and (b) "Ga bridge" N second nearest neighbor cluster models. Only the atoms defining the cluster and the "bridge" are shown. Bond lengths and angles are not to scale.

to $L$, and looks similar to the impurity level assumed in the BAC model. In fact, some $L$-valley tracking is evident. The presence of the N second nearest neighbor cluster also enhances the N charge density contribution to the original lower energy N-band. Furthermore, in the "In bridge" model, the In contribution to the lower N-band is increased significantly compared to the non-cluster model. There is also fairly significant In contribution to the upper N-band.

The fat band structure of the "Ga bridge" model looks similar to that for the "In bridge" model shown in Fig. 3.11. However, with Ga connecting the N second nearest neighbors, the lower N-band does not show enhanced In contribution, which is expected, but it also does not show enhanced Ga contribution. However, the upper N-band continues to show significant In contribution in the "Ga bridge" model, which is indicative of the origin of the upper N-band mainly from N nearest neighbor bonds *surrounding* the cluster, rather than within it (i.e., the cluster bonds that form the upper N-band exclude the bridging atom). This observation is perplexing at first thought, since the upper N-band does not appear in the non-cluster models, yet does not strongly depend directly on the bridging atom. The paradox is resolved in the discussion below and is related to charge-sharing in the cluster through the bridging atom.

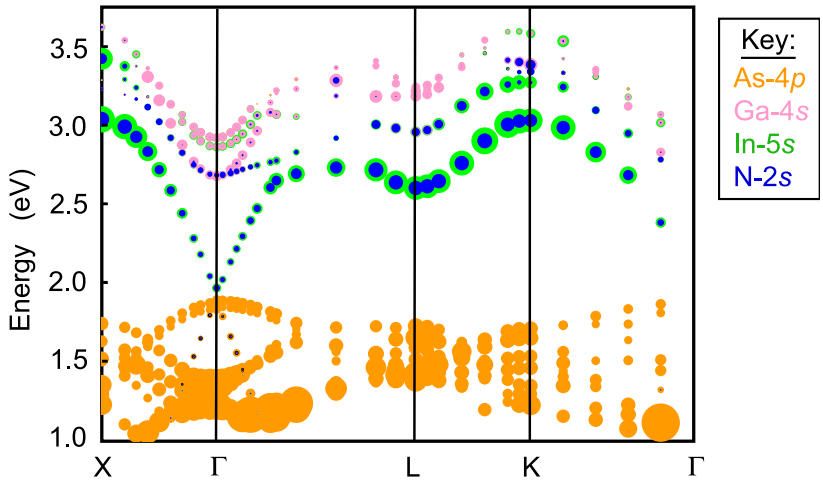


Figure 3.11: (Color) Fat band structure calculated for the "In bridge" N second nearest neighbor cluster model, showing the formation of a second N-band.

Additional insight into the cluster bonding is obtained by examining the electron localization function (ELF) [116] of each model. The ELF provides a means for more precise analysis of the chemical bonding between atoms than simple analysis of the charge density, by including the effects of Pauli exclusion. From examination of the ELF of the various models, we in general find a slightly greater localization of N valence electron density toward Ga nearest neighbors than toward In, due to the stronger, shorter N–Ga bond, irrespective of the presence of clusters or not. However, when two N atoms are clustered through an In bridge, a strong interaction forms between the N atoms through the bridging In atom which diminishes the bonding to the other surrounding atoms significantly. The enhancement of electron localization between N second nearest neighbors through a bridging In atom is greater than for the other N–In bonds in the clustered model and much greater than that for N–In bonds in the non-clustered models. On the other hand, a N second nearest neighbor cluster with a Ga bridge exhibits a deficit of electron localization toward and through

the bridging Ga atom, and the N atoms do not interact strongly. Quite the contrary, the Ga bridge actually enhances N bonding to the surrounding "outer" nearest neighbors of the cluster—those bonds related to the upper N-band—particularly to the surrounding In nearest neighbors. Thus a Ga bridge reduces the N pair interaction, but promotes charge sharing related to the upper N-band. These interactions in the N second nearest neighbor cluster models further illustrate the importance of the N–In bonds in the properties of this material.

In addition, the ELF clearly shows strong localization of charge around the N atoms, which are highly electronegative relative to the other atoms. An overwhelming portion of the crystal charge density is localized around the N atoms, but furthermore the bonds themselves are highly localized. The bonding attractors of the ELF between N and its nearest neighbors are very close to the N atoms and remain very localized in space. In contrast, the As atoms exhibit long, delocalized hybridized bond orbitals that extend out toward the nearest neighbors. These properties exist in both cluster and non-cluster models.

# Chapter 4

# X-Ray Absorption Spectroscopy Results

X-ray absorption spectroscopy (XAS) was performed on several GaInNAs samples to directly probe the N–In nearest neighbor configuration before and after annealing. Nitrogen $K$-edge spectra were taken from 3000 Å thick-film samples to examine the bonding around N atoms. Measurements were also performed on 100 Å thin-film samples to study the effect of biaxial strain. Near-edge fine-structure spectroscopy (NEXAFS) was used for the N-$K$ spectra ($\sim$400 eV) since overlapping In-$M$ and O-$K$ edges occur only slightly higher in energy ($\sim$450 and 530 eV, respectively). Indium $K$-edge spectra also were taken from thin-film samples to examine the local bonding from the perspective of In-centered bonds. Extended fine-structure spectroscopy (EXAFS) was employed for the In spectra. The experimental techniques were detailed in Section 2.2.

In principle, the local chemical environment, or nearest neighbor bonding, of N atoms in GaInNAs could be probed using XAS on any of the elements involved in the bonding: N, In, or Ga. (Indirectly, As spectra also could be employed, to examine the nature of bonds *not* involving N. Since there are exactly two Group III and two Group V elements in the zinc blende crystal, the bonding arrangement around any of the elements reveals relative information about the bonding around the others.) Poor

sensitivity to bonding changes would be expected from As spectra, since As makes up approximately 50% of the material but few of those atoms are second nearest neighbors to N. Gallium spectroscopy would suffer from poor specificity due to the high Ga concentration. Thus, N and In spectra were examined for the analysis below. While In might be expected to give a stronger signal due to its higher concentration and stronger scattering strength, the N spectra proved to be the most sensitive and significant. In hindsight, the high sensitivity of the N spectroscopy to the local bonding is not surprising, since all of the N atoms in the sample are directly involved in the bonding of interest, while only a small fraction of the In and Ga atoms are bonded to N.

## 4.1 Near-Edge X-Ray Absorption Fine Structure

### 4.1.1 Relaxed Thick-Film Results

Figure 4.1(a) shows N $K$-edge NEXAFS spectra taken from 3000 Å thick samples of as-grown and annealed GaInNAs, as well as from a GaNAs reference sample with approximately the same N content. Relative to the GaNAs spectrum, the GaInNAs spectrum is shifted ∼0.2–0.3 eV downward in energy for as-grown material and an additional ∼0.1 eV after annealing. Intensity increases are also observed after annealing in the GaInNAs spectra between 400.5–401.5 eV and at the edge peak. Measurements verified that no change occurred in the GaNAs reference sample after annealing.

Interpretation of the NEXAFS spectra requires accurate band structure calculations to determine the joint DOS of the probed transition, which is the experimental quantity measured by NEXAFS [37]. (In principle, the dipole matrix elements connecting the initial and final states should be included in the calculation of the absorption spectra, but others have shown that little difference results from doing so,

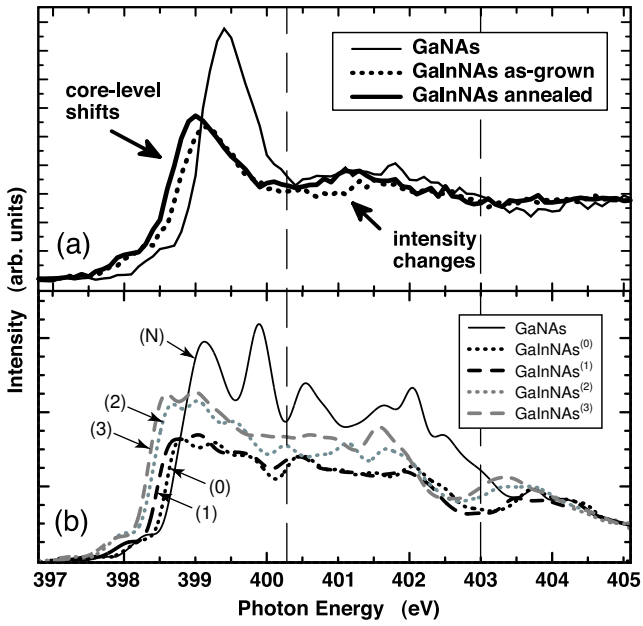


Figure 4.1: (a) Measured N $K$-edge NEXAFS spectra from thick-film samples, and (b) simulated spectra from N-2$p$ PLDOS.

for this material system [100].) The joint DOS is dominated by the DOS of the final state in the case of N-$K$ NEXAFS, since the initial state (the N 1$s$ core level) has a very sharp energy distribution. The final state lies within the empty 2$p$ states of the N atom where the excitation took place, thus the spectra are properly described by the N-2$p$ partial local density of states (PLDOS).

The simulated NEXAFS spectra from the different model structures, shown in Fig. 4.1(b), were obtained by convolving the calculated N-2$p$ PLDOS by a 0.35 eV (FWHM) Gaussian to account for the finite monochromator resolution (0.25 eV) and for lifetime broadening ($\sim$0.25 eV). The PLDOS were calculated relative to the Fermi levels in each model and were shifted to match the absolute edge energy. Relative offsets between the spectra were determined from calculated core-level shifts ($\Delta c$) and conduction band offsets (CBO). The CBO were taken directly from the band edges in band structure calculations, since the model structures are nearly identical and therefore the average bulk local potentials in the Van de Walle model can be assumed to be the same [91]. In practice, the core-level shifts dominate differences in the band offsets by two orders of magnitude anyway. Core-level shifts are calculated in the initial state approximation by computing the average electrostatic potential $\overline{V}$ on the N ion for each model, via

$$\overline{V} = \int V(\mathbf{r})\rho_{\text{test}}(|\mathbf{r} - \mathbf{R_N}|)\mathrm{d}^3\mathbf{r}, \tag{4.1}$$

where $V(\mathbf{r})$ denotes the potential throughout the unit cell and $\rho_{\text{test}}$ is a normalized test charge placed a distance $|\mathbf{r} - \mathbf{R_N}|$ from the N center at $\mathbf{R_N}$. The core-level shifts are then obtained from

$$\Delta c = (\overline{V}_2 - E_{\text{Fermi},2}) - (\overline{V}_1 - E_{\text{Fermi},1}), \tag{4.2}$$

where the $\overline{V}_i$ are referenced to the Fermi levels in each model.

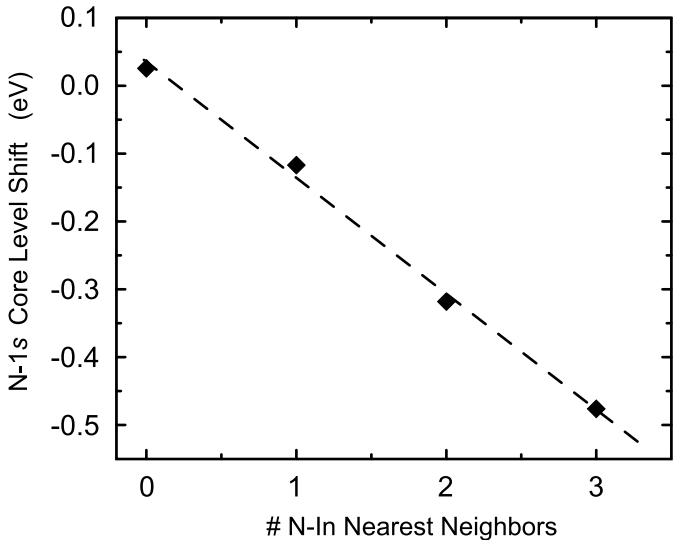


Figure 4.2: Calculated core level shift $\Delta c$ of GaInNAs$^{(n)}$ relative to GaNAs.

The simulated spectra in Figure 4.1(b) show that increasing the degree of N–In bonding monotonically shifts the N $K$-edge to lower energies by ∼110–120 meV/In atom, when accounting for both the (nearly constant) CBO between GaInNAs$^{(n)}$ and GaNAs (50–80 meV) and the core-level shifts. (The notation "GaInNAs$^{(n)}$" was defined in Section 3.1.1 and refers to a model structure with $n$ In atoms surrounding each N atom.) In addition, from Fig. 4.2 which shows only the $\Delta c$ component of the calculated spectrum shift, we see that the $\Delta c$ between GaNAs and GaInNAs$^{(0)}$ is nearly zero, indicating that first nearest neighbor bonding is the dominant parameter in determining the shift since second and higher In nearest neighbors do not appreciably affect $\Delta c$.

Thus, we conclude that the shifts observed in the measured spectra in Fig. 4.1(a) are due to increased bonding between N and In after annealing. The lack of any change in the GaNAs spectra after annealing further supports this conclusion, since there is no possible nearest neighbor reconfiguration in GaNAs. (We note, however,

a small shift in the PL peak wavelength for the GaNAs sample after annealing. The band gap shift in GaNAs probably involves second nearest neighbor N clustering and other effects not discussed here.)

The relation between nearest neighbor bonding and $\Delta c$ can be understood through the traditional theory of chemical shift in NEXAFS spectra: the modification of the core potential resulting from a perturbation of the screening potential. The N–In bond has a greater electronegativity (E.N.) difference than the N–Ga bond, which causes N to extract more charge from In than from Ga ($\text{E.N.}^{\text{In}} = 1.78$, $\text{E.N.}^{\text{Ga}} = 1.81$, $\text{E.N.}^{\text{N}} = 3.04$). The additional negative charge around N reduces its core-level ($1s$) binding energy and shifts the spectrum to lower energies. Previous theoretical work on GaNAs has shown charge localization on N [117], which is confirmed by our simulations which show localization of >80% of the crystal's charge density on the highly electronegative N atoms (see Section 3.2.3). Our simulations additionally show increasing charge localization on N when bonded to more In atoms, causing a progressive increase in polarity of the N–In bond. These simulation results support the reasoning presented above for a monotonically increasing core level shift with increased N–In bonding.

By comparing quantitatively the measured and calculated shifts in Fig. 4.1, we conclude that our as-grown material is nearly random in configuration. The observed shift of ∼0.2–0.3 eV between GaNAs and as-grown GaInNAs, and the additional ∼0.1 eV shift after RTA, is consistent with a distribution of bonds dominated by $\text{GaInNAs}^{(1)}$ before annealing and $\text{GaInNAs}^{(3)}$ after annealing. Figure 3.3 shows that this corresponds to a random configuration before annealing and the thermodynamically-preferred configuration after annealing. This result is not surprising, as our low-temperature MBE growth promotes a kinetic product, while increased thermal dosing during RTA moves the material toward thermodynamic equilibrium. A previous theoretical study using Monte Carlo simulations also predicted

a thermodynamically-preferred configuration favoring N–$In_3Ga$ clusters, but did not consider the effects of annealing or high In content [118].

While nearest neighbor bonding directly impacts the spectrum shift, finer details of the bonding appear as differences in the precise edge shape (i.e., the oscillations above the edge). The increases in intensity observed around 401 eV and at the edge peak both can be attributed to increased numbers of N–In bonds, as shown in Fig. 4.1(b). The strong oscillations present in the simulations that are not present in the measured spectra are due to artificial long-range periodicity introduced by the supercells and also finite $k$-point sampling. While averaging several supercells may better model the alloy effects and eliminate the strong oscillations, a previous study has shown this to have only a minor effect on the DOS [82]. Additional effects such as second nearest neighbor interactions and N clustering could also affect the spectra to second-order. Calculations of some N clustering effects are discussed below in Section 4.1.4.

The relationship between the arrangement of N–In/Ga bonds and the band gap shift/annealing behavior can be further understood through analysis of the calculated "fat band structure" of the material. The formation of a "N-band" within the band gap of the host crystal [(In)GaAs] for N concentrations greater than 1% or so has been discussed in Section 3.2.2. Since the N-band, which determines the band gap, is dominated by N nearest neighbor bonding, it is clear that the band gap depends on the number of N–In nearest neighbors. The total energy calculations discussed in Section 3.2.1 show that when both Ga and In are bonded to N, the Ga–N bond is stretched further from equilibrium than the In–N bond. This is due mainly to the fact that the GaInNAs alloy has a lattice constant near that of GaAs, rather than that of either of the binary nitrides. Additionally, the Ga–N bond is further stretched when fewer In atoms are bonded to N. In this way, the degree of valence electron interaction between the atoms is modulated by the Ga:In ratio. When the N conduction band

is dominated by N–In bonds, for example, the band gap is larger since the reduced bond stretching leads to stronger interatomic interactions. A nonlinear increase of the band gap with the number of N–In nearest neighbors results from the details of the atomic relaxations in each environment discussed in Chapter 3 (see Fig. 3.6). These bond-length effects on the band gap variation are similar to those used to explain the band gap bowing in GaNAs, calculated from first principles [119].

Additionally, the importance of the In-5$s$ contribution to the blueshifted N-band found from the fat bands analysis implies that the same mechanism that blueshifts the PL upon annealing also contributes to increasing the optical efficiency of the material somewhat by creating additional N–In "active sites." In the case of PL, other factors related to annealing, particularly the removal of point defects that act as nonradiative recombination centers, are dominant in improving the efficiency. However, we show in Chapter 5 from the results of absorption measurements and electroreflectance spectroscopy that annealing does indeed increase the oscillator strength of band edge recombination, up to a factor of 1.5–2, which is manifested in a significant increase in the absorption coefficient after annealing.

### 4.1.2 Strained Thin-Film Results

The experiments and analysis described above were repeated on strained thin-film (100 Å) samples of GaInNAs having essentially the same composition as used above (∼30% In and ∼3% N). The strain in the films was verified by x-ray reciprocal space mapping, which showed that the thin films were grown pseudomorphically on GaAs [34]. Similar features were observed in thin-film NEXAFS spectra as for the thick films, and the same basic conclusions were reached: despite strain in the films, the as-grown material contained a nearly random distribution of bonds, while the material annealed at 800°C for 2 min showed an increase in the degree of N–In bonding toward a distribution peaked at 2 or 3 N–In bonds per N atom. Representative N-$K$ edge

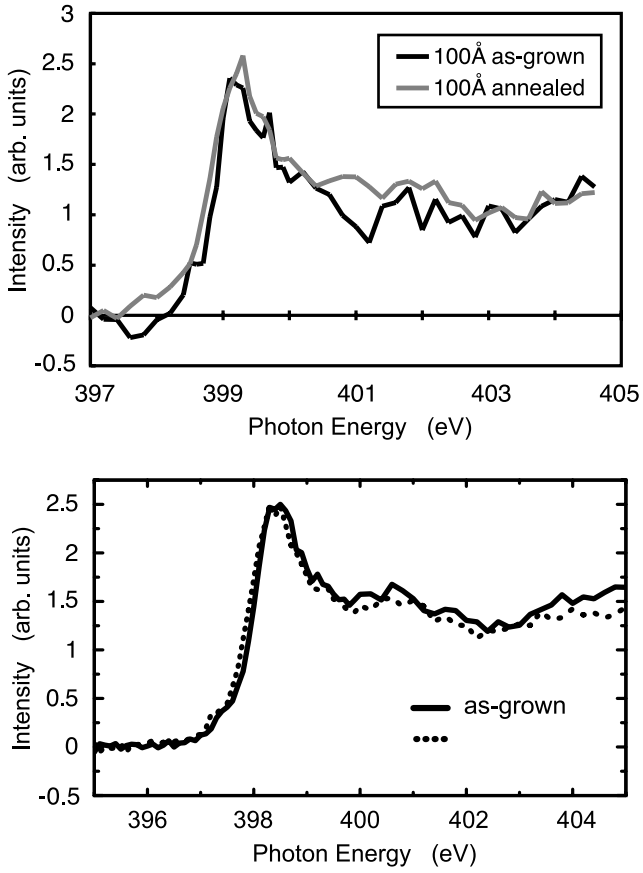


Figure 4.3: Measured N $K$-edge NEXAFS spectra from compressively-strained thin-film GaInNAs samples, showing essentially the same features as for the thick-film samples.

NEXAFS spectra taken from GaInNAs thin-film samples before and after annealing are shown in Fig. 4.3. Longer acquisition times were necessary in these experiments to achieve comparable signal-to-noise ratio, since the x-ray interaction length was much shorter. Furthermore, several acquired spectra were averaged together (from multiple samples as well as multiple exposures).

Proper analysis of the thin-film NEXAFS data required repeating the supercell calculations to account for strain. Calculations were performed nominally on the

same 64-atom supercell model structures used for the analysis above. To account for the biaxial compressive strain in the film resulting from pseudomorphic growth on a GaAs substrate, the lattice constant in the two in-plane directions were fixed to that of GaAs for each model. The GaAs lattice constant was taken from calculations using the same Ga and As pseudopotentials as for the GaInNAs calculations, rather than from the experimental value, for self-consistency. Relaxations were then performed to determine the out-of-plane lattice constant and equilibrium atom positions, before performing calculations of the band structure, partial local density of states, and core level shifts (see details in Chapter 3 and Appendix A). The atomic positions and out-of-plane lattice constant were relaxed independently. During variation of the out-of-plane lattice constant, the relative atomic coordinates within the supercell were held fixed at the equilibrium value for the corresponding cubic (unstrained) supercell. Then, a final relaxation of the atomic coordinates within the tetragonal supercell was performed, resulting in the same minimum energy structure as found by performing a single relaxation with both atomic coordinates and out-of-plane lattice constant as degrees of freedom. The two-step relaxation was much more computationally efficient, however, than relaxing all the degrees of freedom simultaneously. Ultimately, the relative positions of the ions in the supercell changed very little between the unstrained (cubic) and strained cases, and the change in the shape of the supercell was the dominant effect. The Poisson's ratio determined using this method (0.34) agrees to within 4% of that obtained using Vegard's law (linear combination of the elastic constants $C_{11}$ and $C_{12}$ of the endpoint binaries) which is consistent with synchrotron x-ray diffraction experiments [120]. Since the calculations using these tetragonal supercells do not include quantum confinement effects or a free surface, the results strictly apply only to biaxially strained bulk material, rather than true thin films, but with regard to the x-ray absorption experiments, this distinction is minor.

The driving force for the nearest neighbor reconfiguration toward increased N–In

bonding after annealing is the reduction of the total energy of the system, as already discussed. The reconfiguration also slightly increases the average lattice constant of the (model) material by ∼0.05%, which results in increased strain energy when grown pseudomorphically on GaAs (Fig. 3.3). We can calculate how significant the increase in strain may be, to determine whether an effect on the annealing behavior is predicted for strained thin-film samples. Figure 4.4 shows the total energy calculated for the different model structures, with and without strain. The total energy penalty for growing strained material (the "strain penalty") is depicted by the vertical lines connecting each set of points (strained and unstrained). The strain penalty is relatively constant at ∼2 kcal/mol for all of the configurations. The only significant increase in strain penalty occurs between 0 and 1 N–In nearest neighbors, where it increases ∼20%. Since as-grown material (assumed to be random) is predicted to have a distribution of bonds centered around 1 N–In nearest neighbor for the GaInNAs composition considered here (31% In, 3% N), the strain penalty should not favor any particular bonding arrangement over another. So we do not predict a significant effect of strain on the annealing behavior, from a thermodynamic point of view.

The results of band structure and $\Delta c$ calculations on the biaxially strained models show that the N core levels are modified and the conduction band offsets change slightly compared to the unstrained case. The core-level shifts relative to unstrained GaNAs are reduced, and the rate of shift with increasing N–In nearest neighbors is also reduced somewhat. Thus, we qualitatively expect smaller spectrum shifts between the NEXAFS spectra for strained samples than for unstrained samples, assuming the same behavior of N nearest neighbor reconfiguration upon annealing. Quantitatively, the shifts are expected to be ∼0.1–0.15 eV smaller for strained samples than for unstrained samples if the nearest neighbor reconfigurations are identical.

The main quantitative measurement result of the thin-film NEXAFS experiments is the magnitude of the N $K$-edge spectrum shift relative to GaNAs, which includes

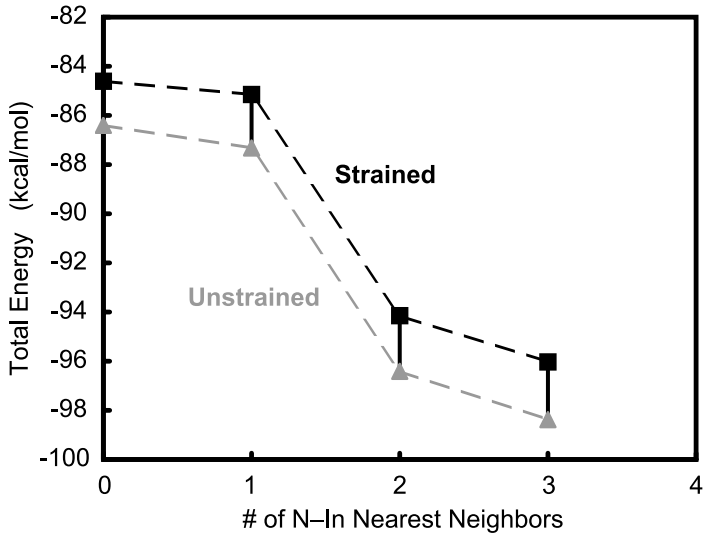


Figure 4.4: The strain penalty for growing GaInNAs pseudomorphically on GaAs, depicted by the vertical lines connecting the points for strained and unstrained calculated total energies, does not depend strongly on the number of N–In nearest neighbors.

both the core-level shift and the nearly constant offset from the GaNAs/GaInNAs CBO. The calculated spectrum shifts for the strained GaInNAs$^{(n)}$ models is plotted in Fig. 4.5, along with the measured data. For comparison, the data and theoretical predictions for the unstrained thick-film samples are also included. The straight lines in the figure indicate the calculated spectrum shifts relative to GaNAs for the different configurations of N–In nearest neighbors in both strained and unstrained GaInNAs. The measured shifts for as-grown and annealed material are plotted as symbols on top of the theoretical curves to determine the dominant bonding configuration. The arrows in the figure indicate the transitions from as-grown to annealed material. Some uncertainty in the calculations exists from the difficulty in accurately determining conduction band offsets, and a measurement error on the order of a couple of symbol widths exists, but the general conclusions are clear. As-grown material is dominated by GaInNAs$^{(1)}$ bonds (a random distribution), while annealed material contains an increase in N–In bonding (toward thermodynamic equilibrium). These samples show signs of "incomplete" annealing, with further shifts in the nearest neighbor bonding possible. Quite significantly, little difference is observed in the bonding distributions between strained and unstrained GaInNAs, at least for this MBE-grown material, consistent with the thermodynamic analysis above.

Besides the spectrum shifts, intensity changes are also observed between as-grown and annealed material. The most obvious intensity change occurs at ∼401 eV for unstrained material [see Fig. 4.1(a)]. The increased intensity in this energy region corresponds to a predicted increase in the N-2$p$ PLDOS when the number of N–In bonds increases, as seen in Fig. 4.1(b). Partial local density of states calculations of the empty N-2$p$ states for the strained model structures, shown in Fig. 4.6, reveal only minor differences in the edge shapes for the strained case compared to the unstrained calculations, while small offsets in edge energy are the most significant features. The small differences in the intensity changes upon annealing that are predicted for the

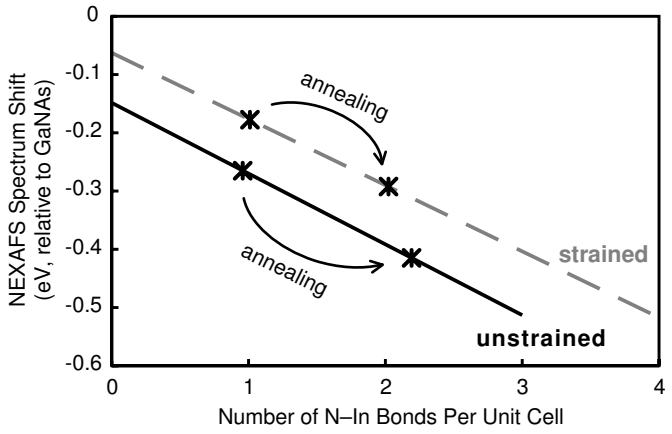


Figure 4.5: Measured spectrum shifts (symbols) in N $K$-edge NEXAFS, relative to unstrained GaNAs, plotted on top of theoretical curves showing the predicted dependence on N nearest neighbor environment, for both strained and unstrained GaInNAs. Arrows indicate transitions from as-grown to annealed material.

unstrained *versus* strained samples are highlighted in yellow in Fig. 4.6. In going from low N–In coordination to high N–In coordination, the intensity at the edge peak becomes sharper for unstrained material, while the situation is reversed for strained material. Also, a slight increase in energy of the intensity minimum around 401 eV is predicted for strained *versus* unstrained material, with a narrower bandwidth of the minimum also predicted. These features are manifested in the measured data, as evident by comparing Figs. 4.1(a) and 4.3.

A final result of the thin-film calculations is an estimate of the maximum thickness of material that can be grown pseudomorphically on GaAs, from the magnitude of the strain penalty in Fig. 4.4. By converting the 2 kcal/mol value of strain penalty into energy/area/thickness and comparing to a calculation of the energy/area of forming a square array of misfit dislocations using elasticity theory, we estimate a critical thickness of $\sim$700 Å. This overestimates the critical thickness compared to a simple calculation using only elasticity theory which gives 195 Å, and is also somewhat

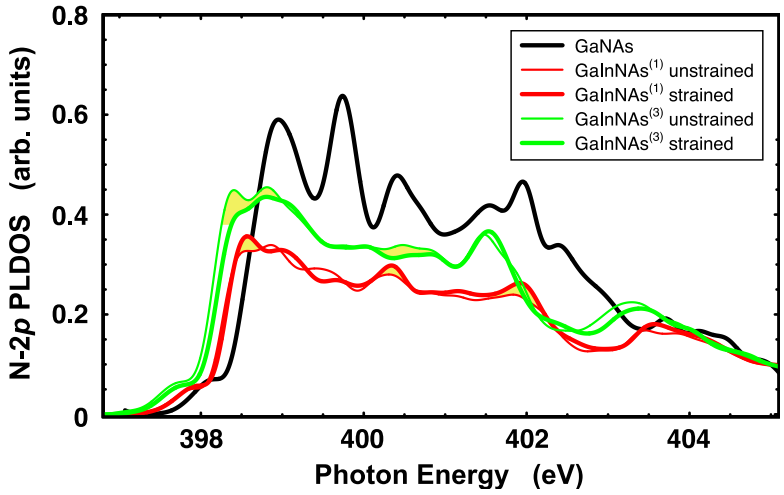


Figure 4.6: (Color) Comparison of calculated, broadened PLDOS for strained and unstrained GaInNAs, showing small offsets between the spectra, but very little intensity differences. The few significant intensity differences between the strained and unstrained models are highlighted in yellow.

above the experimental observation of ∼320 Å. In this analysis, the formula for the energy/area of a square array of misfit dislocations is given by [121]

$$E_{\text{disloc\_array}} = \frac{\mu b^2}{4\pi(1-\nu)} \frac{2}{S} \ln\left(\frac{\beta h}{b}\right), \tag{4.3}$$

where $S$ is the average distance between dislocations (with the critical thickness corresponding to the limit $S \rightarrow \infty$), $b$ is the length of the Burger's vector (on the order of the atomic spacing), $\beta$ is a parameter related to the size of the dislocation core (usually taken as $\approx 1.0$), $\mu$ is the shear modulus ($C_{44}$ for [100] epitaxial films), $\nu$ is Poisson's ratio, and $h$ is the film thickness.

### 4.1.3 Comparison of MBE-Grown and OMVPE-Grown Material

Nitrogen $K$-edge NEXAFS data were also taken from OMVPE-grown thin-film samples [122] to compare with the MBE-grown material. These data did not show any significant shift between as-grown and annealed samples, but both were shifted significantly from the GaNAs edge. Both spectra look similar to the spectrum taken from annealed MBE material, although a blueshift in the photoluminescence wavelength is still observed after annealing. Possible *in situ* annealing by the x-ray beam during the experiment was suspected, but is unlikely since the temperature rise at the surface of the wafer was estimated to be too low. However, some degree of *in situ* annealing occurring during the high-temperature OMVPE growth ($\sim$700°C) is possible. Then, as-grown OMVPE GaInNAs material would be partially annealed, with the remainder of the nearest neighbor rearrangement occurring during post-growth annealing. We show in Chapter 5 how a shift in the *distribution* of nearest neighbor states occurs during annealing, progressively blueshifting the band gap.

In Chapter 5, we also show that both as-grown GaInNAs and as-grown GaInNAsSb from MBE have random configurations, a result of the low growth temperature. The data here suggests that as-grown OMVPE GaInNAs has a less random nearest neighbor configuration, consistent with the higher temperature growth which somewhat anneals the material *in situ*. An interesting question, then, is what would be the behavior of OMVPE GaInNAsSb (if it could be grown)? Since Sb is a reactive surfactant that reduces surface diffusivities during growth, it is possible that as-grown OMVPE GaInNAsSb would also have a random configuration, despite the higher-temperature growth.

### 4.1.4 Nitrogen Clustering Effect

We observe some small differences in the fine structure of the N-2$p$ PLDOS for the N second nearest neighbor cluster models discussed in Section 3.2.3, which may be relevant to NEXAFS measurements. For both cluster models, the density of states of the small N-2$p$ "pre-edge" is increased relative to the non-clustered models and actually becomes a double peak, as shown in Fig. 4.7. Changes in this region might be interpreted as related to conduction band "tail states" in the band gap, but actually arise directly from the density of states at the bottom of the N-band. The high dispersion of the N-band at its minimum, combined with the small fraction of atoms in the crystal that strongly contribute to this band, cause the absolute density of these states to be small. On the other hand, changes to the density of states in this region can be directly correlated to changes in N bonding. In addition to the general increase in density of states in the pre-edge observed for the cluster models, a subtle difference is also observed *between* the two cluster models, as shown in Fig. 4.7. The "In bridge" model shows a nearly constant distribution of states throughout the pre-edge, while the "Ga bridge" model peaks in the higher energy portion of the pre-edge. The resolution of the pre-edge in current NEXAFS measurements is not sufficient to discriminate such subtle differences, although evidence does exist of a double-peak structure. Perhaps future experiments could try to resolve this pre-edge more carefully to look for second nearest neighbor clustering effects and/or changes with annealing. The predicted thermodynamic preference for N–In–N clusters rather than N–Ga–N clusters (see Section 3.2.3) might be examined.

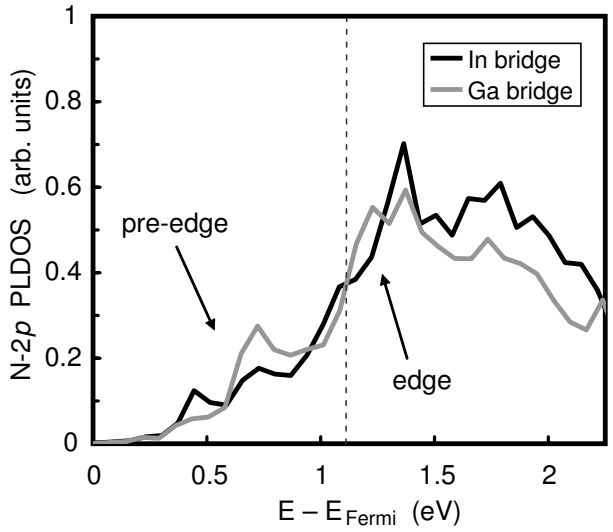


Figure 4.7: Comparison of calculated N-2$p$ PLDOS of "In bridge" and "Ga bridge" N second nearest neighbor cluster models.

## 4.2 X-Ray Emission Spectroscopy

Strocov *et al.* recently performed x-ray emission spectroscopy (XES) measurements on GaInNAs [123]. The XES experiment is similar to the fluorescence XAS experiment. After excitation and formation of the core hole, electrons near the top of the valence band can transition down into the hole, emitting a soft x-ray which comprises the measured signal in both XAS and XES. In fluorescence XAS, the excitation energy is scanned and all of the emitted photons are collected to yield a signal essentially proportional to the conduction band density of states. In XES, a fixed excitation energy is used and the emitted photons are analyzed by a spectrometer to yield a signal essentially proportional to the valence band density of states.

The general features observed in the N-$K$ XES spectra are a gradual onset of the valence band maximum (VBM), a peak in the valence band density of states $\sim$4 eV below the VBM, a smaller peak $\sim$6 eV below the VBM, a narrow peak at

7.4 eV below the VBM in resonant XES spectra, and a shift of the N density of states toward the VBM for GaInNAs relative to GaNAs [123]. We simulated the XES spectra, as a function of number of N–In nearest neighbors, using the density of occupied N-2$p$ states from the PLDOS calculations used above to analyze the XAS spectra. In general, we find excellent agreement with the experimental spectra. The valence band PLDOS rises gradually from the band edge, a large peak ∼4 eV below the VBM is present, with a smaller peak ∼6 eV below the VBM, and a sharp peak 7 eV below the VBM. A small additional peak ∼3.2 eV below the VBM is present in the simulations, however this peak is too close to the 4 eV peak to easily resolve experimentally. These results are similar to calculations performed on GaNAs [100]. Furthermore, as the number of N–In nearest neighbors is increased, the peak ∼4 eV below the VBM, and to a lesser extent the peak at ∼3.2 eV, shift to higher energies by up to 0.3 eV, accumulating N charge density near the VBM. The peak ∼6 eV below the VBM increases in intensity monotonically with increasing number of N–In nearest neighbors, but does not shift in energy. The sharp peak at 7 eV below the VBM is largely unaffected by the N local environment.

While the overall character of the VBM is mostly derived from As-4$p$ states, the subtle changes in the N PLDOS described above are significant because the band-edge optical transitions are dominated by N states (the N-band). The N charge accumulation at the VBM with increased N–In bonding causes a modest increase in the optical transition matrix element, increasing the band-edge absorption coefficient significantly and contributing to the increase in PL efficiency after annealing. This increase in matrix element after annealing is discussed in more detail in Chapter 5.

## 4.3 Extended X-Ray Absorption Fine Structure

In addition to N-$K$ NEXAFS, we also measured the nearest neighbor radial distribution function (RDF) around In for as-grown and annealed 100 Å GaInNAs quantum well samples using In $K$-edge EXAFS. The measured data are shown in Fig. 4.8. Radial distribution functions, shown in Fig. 4.9(a) were obtained from the raw data by $k$-space filtering and taking the Fourier transform, as described in Section 2.2.3. The RDFs for both as-grown and annealed material show a dominant In–As peak at $\sim$2.25 Å and a smaller shoulder at shorter bond lengths, accentuated by the vertical arrows in the figure. The shoulders correspond to the In–N bond, whose precise length is shown by simulations to depend on the number of Ga atoms around N, as shown in Fig. 4.9(b). The sharp curves in Fig. 4.9(b) show the distribution of In bond lengths calculated from the different 64-atom GaInNAs$^{(n)}$ model crystal structures. Simulated RDFs were then obtained, and fit to the experiments, by convolving the bond length distributions with a mixed Gaussian-Lorentzian function and assuming that annealing drives the material from a distribution with mostly GaInNAs$^{(1)}$ to mostly GaInNAs$^{(3)}$. The key feature in the as-grown In RDF is the change in slope on the short bond length side of the In–As peak, indicating the presence of an In–N peak that is mostly obscured by the dominant peak. The In–N shoulder in the RDF becomes more prominent after annealing because the number of In–N bonds increases and also because the peak radius shifts further from the center of the overwhelming In–As peak, to a region with a flatter background. The same features appear in the simulated curves. The excellent agreement between the simulation and experiment is further verification, using an independent measurement, that annealing increases the degree of N–In bonding.

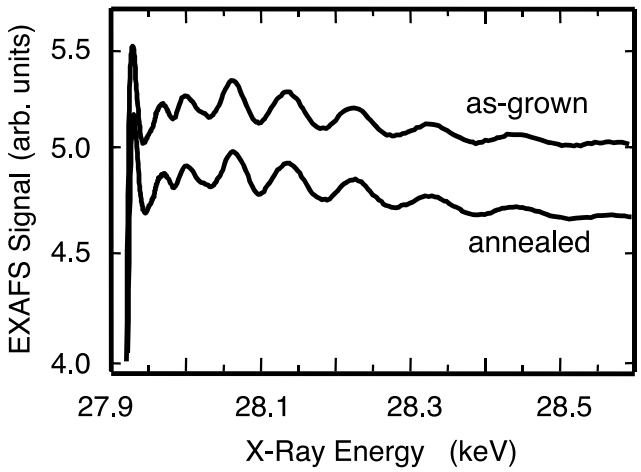


Figure 4.8: Raw In $K$-edge EXAFS spectra taken from 100 Å GaInNAs thin films, with background subtracted.

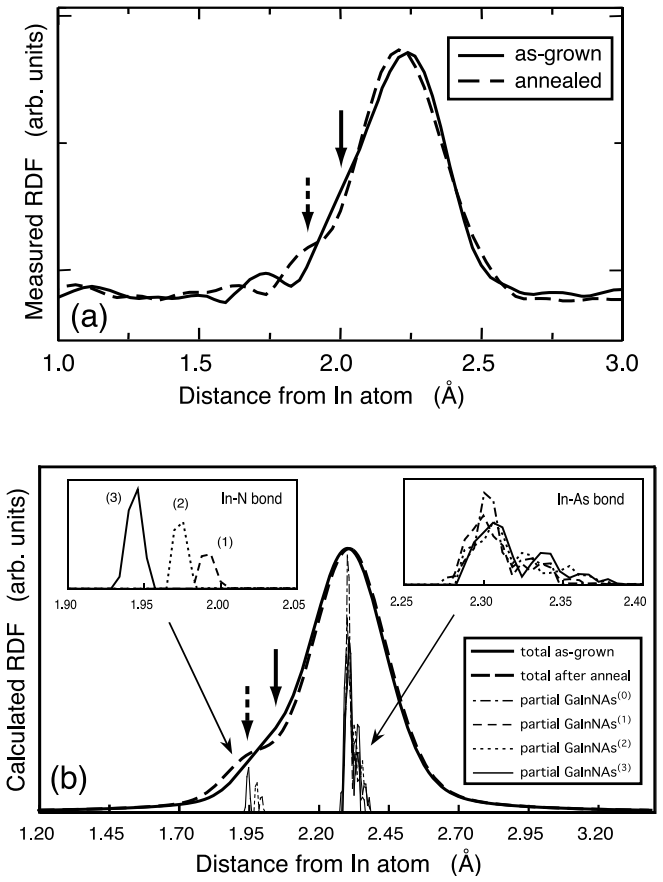


Figure 4.9: (a) Measured In first nearest neighbor radial distribution function (RDF), extracted from $K$-edge EXAFS data shown in Fig. 4.8. Arrows indicate the short bond-length In–N bond. (b) Simulated RDFs, calculated from bond-length distributions in the model structures. The insets show close-up views of the component peaks.

# Chapter 5

# Quantitative Determination of Nearest Neighbor Distributions in GaInNAs(Sb)

Building on the results of the x-ray absorption measurements and the predictions of the band structure calculations, various optical spectroscopy techniques were used to determine quantitatively the evolution of N nearest neighbor states in GaInNAs(Sb) quantum wells during annealing. The results of these photoluminescence, electroreflectance, and photocurrent spectroscopy experiments are discussed in this chapter.

## 5.1 Room Temperature Photoluminescence Measurements

A series of photoluminescence (PL) spectra taken at room temperature from variously annealed GaInNAsSb QW samples is shown in Fig. 5.1. The samples were *p-i-n* diodes, described in Section 2.1.2, used also for electroreflectance spectroscopy (Section 5.3) and absorption measurements (Chapter 6). The series of samples shown in the figure correspond to as-grown, annealed at 760°C for 1 min, annealed at 800°C for 1 min, and annealed at 800°C for 3 min. The figure shows that increased thermal

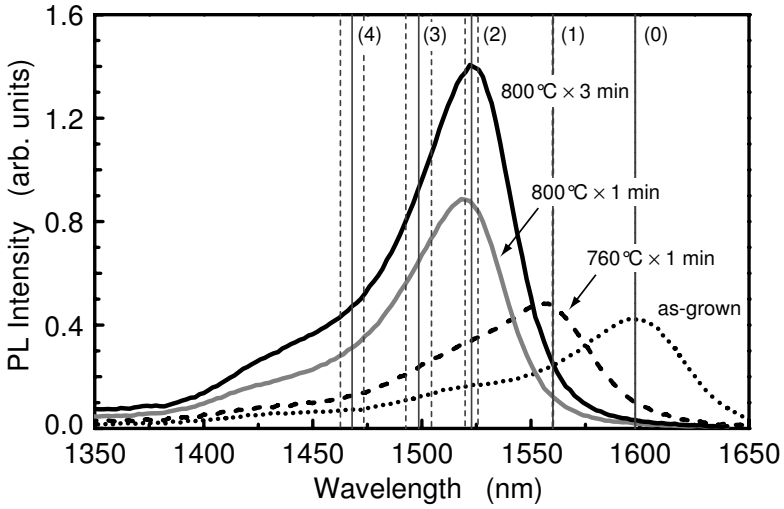


Figure 5.1: Room temperature photoluminescence spectra from as-grown and annealed GaInNAsSb QWs. The solid vertical lines indicate the N–In nearest neighbor peak fit positions, while the dashed vertical lines demarcate one standard deviation of error for each peak position.

dose in the RTA results in increased PL intensity, but also a blueshift of the peak wavelength (increased band gap). The wavelength shift apparently occurs in discrete jumps, and after a certain dose (800°C for 1 min in this case), the wavelength shift saturates while the intensity continues to increase. Similar behavior is observed from GaInNAs samples as well.

As described in Section 2.3.2, the presence of nonradiative defects or traps in the material will degrade PL efficiency (intensity) by introducing a competitive recombination pathway to spontaneous emission. Thus, a highly defective material will generally have low PL emission. The as-grown GaInNAs(Sb) material contains a large concentration of point defects mainly caused by the low growth temperature required to inhibit phase segregation and other gross growth defects as discussed in Section 2.1.1. The presence of Sb has been found generally to reduce the concentration of as-grown point defects, and consequently the as-grown PL intensity from

GaInNAsSb QWs is a factor of 2–4× higher than for as-grown GaInNAs of comparable N composition. (There seems to be an empirical correlation between higher N-content and lower PL intensity in these materials [12, 33, 124].) For both GaInNAs and GaInNAsSb, however, the PL intensity for as-grown material is generally low and can be increased by a factor of 10–50× by thermal annealing, as demonstrated in Fig. 5.1. The dramatic increase in PL intensity after annealing is often greater for GaInNAs than for GaInNAsSb due to the poorer as-grown material. The large increase in PL efficiency after annealing is predominantly due to healing of nonradiative point defects in the crystal, which is highly desired.

The spectra shown in Fig. 5.1 were acquired under conditions of high excitation density (20 kW/cm$^2$) and relatively high temperature (room temperature), enabling the appearance of excited state transitions observed as the short-wavelength bumps in the spectra. These transitions could be fit very well to a set of five Gaussian peaks, indicated by the vertical lines in Fig. 5.1. The fitting was performed independently for each spectrum, using the smallest number of peaks that resulted in a reasonable fit to the data, and a set of exactly 5 peaks common to all of the spectra was found. Example peak fits are shown in Fig. 5.2, which also shows that the GaAs substrate peak simultaneously is well fit by a single Lorentzian line. [Fig. 5.2(a)]. In Fig. 5.2(b), the Gaussian N nearest neighbor peaks are accentuated by a semilog scale. Attempted peak fitting with any number of Lorentzian lines for the QWs yielded very poor results.

The Gaussian lineshape of the spontaneous emission spectrum at room temperature [and thus also the absorption spectrum through the van Roosbroeck-Shockley relation given in Eq. (2.3)] is significant, and somewhat unexpected. We also observe a Gaussian lineshape in electroluminescence, absorption (Section 6.1), and electroreflectance (Section 5.3) experiments, with linewidths in agreement with the PL peak fits. A Gaussian lineshape is usually associated with very high temperatures (or effective temperatures), as described in Section 2.3.2, although a Gaussian lineshape

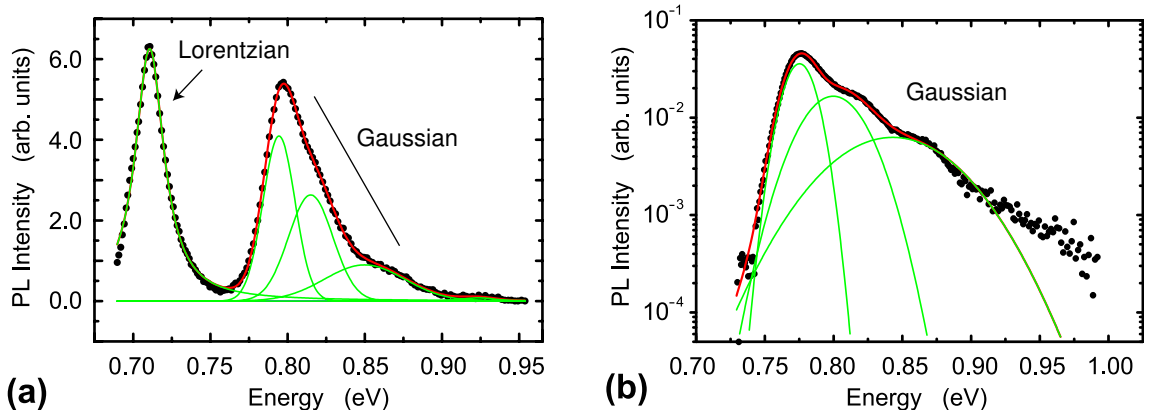


Figure 5.2: (Color) (a) Example Gaussian peak fitting of room temperature PL spectrum from as-grown GaInNAsSb, with simultaneous Lorentzian fit to the GaAs double-diffraction peak at 0.71 eV. (b) The individual peaks in this PL spectrum of GaInNAsSb annealed at 760°C for 1 min are accentuated when plotted on a semilog scale.

has been reported for multiple quantum well samples at room temperature [125]. We observe a Gaussian lineshape for the GaInNAs(Sb) QW emission even at very low temperatures (∼15 K), which is quite unusual. We understand the Gaussian lineshape in terms of Toyozawa's theory of absorption lineshape as resulting from a strong exciton-phonon coupling in GaInNAs(Sb) from the large exciton mass, large exciton radius, and intrinsic lattice defects, which correspond to an effective increase of the lattice temperature [51].

In Fig. 5.1, the fit peak positions are indicated by the solid vertical lines (with $1\sigma$ deviations indicated by the dashed vertical lines). The peaks show a spacing of 17–20 meV and have FWHM of 20–25 meV. Within this energy range above the fundamental gap, no excited state transitions are expected, since the first light hole transition is more than 100 meV higher in energy, and similarly for the second heavy hole level. Thus, the levels can be associated with either a splitting of the band gap

(e.g., caused by different N–In nearest neighbor arrangements), intrawell spatial inhomogeneities, interwell inhomogeneities (thickness or composition), or defect states. Spatial and interwell inhomogeneities are ruled out by repeating the measurements at very low temperatures (25 K), where only a single sharp transition is observed for each sample. If different regions of the sample had local fluctuations of the band gap from inhomogeneities observable by PL (distance separation more than an exciton radius), then the low temperature spectra would show multiple discrete sharp peaks. At 25 K, the PL spectra show a single symmetrical line or a slight shoulder on the *low* energy side arising from the $\exp(-\hbar\omega/kT)$ term in the van Roosbroeck–Shockley relation for band-to-band recombination [see Eq. (2.3)]. Therefore, the discrete peaks in the room temperature spectra cannot correspond to spatial or interwell inhomogeneities because they do not appear in the low temperature spectra. Furthermore, increasing the excitation density in the PL experiment was found not to be effective in filling these states, while increasing the thermal distribution of carriers by raising the temperature was effective. This is additional evidence that rules out spatial inhomogeneities. If the sample had spatially localized band gaps, each region would accumulate carriers and emit luminescence at different wavelengths when sufficient incident power was applied. For a homogeneous QW, the density of states is very high at the band edge and significant bandfilling is difficult to achieve with increased excitation density.

Then, drawing on the knowledge gained from the XAS experiments (Chapter 4) and the *ab-initio* band structure calculations (Chapters 3 and 4) which showed a monotonic increase in the number of N–In nearest neighbors during annealing and a corresponding predicted increase in band gap of up to ∼150 meV for GaInNAs, we assign the five peaks in the PL spectra to the five possible N nearest neighbor configurational states, since no other transitions are expected in this energy range. Not coincidentally do we find exactly five peaks, which correspond to the five possible

configurations with 0–4 In atoms bonded to N. The numbers in parentheses in Fig. 5.1 indicate the number of In neighbors to N for each of the fit peak positions. Electroreflectance (ER) results presented below in Section 5.3 solidify the assignment of these peaks to the different N nearest neighbor configurations. A quantitative analysis of the distributions of states is performed using ER, taking advantage of the excited state nature of ER spectroscopy.

## 5.2 Temperature-Dependent Photoluminescence Measurements

The temperature dependence of the PL spectra provide a metric of the concentration of defects in the samples. The variation of the peak energy with temperature, or more precisely the deviation from the expected variation, can be used to quantify the crystal quality. In these experiments, we associate the peak PL energy from the QWs with the semiconductor band gap and assume that changes in the peak energy track the variation of the band gap. This assumption is shown to be valid in Appendix B.

Generally, the band gap of a semiconductor monotonically increases as the temperature is decreased due to thermal contraction of the crystal and stronger interactions between the valence electrons. The variation often follows the empirical relation developed by Varshni [126]:

$$E_g(T) = E_g(0) - \frac{\alpha T^2}{T + \beta}, \tag{5.1}$$

where $T$ is the absolute temperature, $E_g(0)$ is the band gap at $T = 0$, and $\alpha$ and $\beta$ are fitting parameters. Experimental observations of the temperature dependence of the band gap of GaInNAs have shown significant deviation from this functional form at temperatures below ∼150 K, in the extreme case exhibiting an "S" shape with two

maxima in the $E_g(T)$ curve [127–129]. The turnover of the $E_g(T)$ curve at low temperatures has been attributed to potential fluctuations in the crystal, due to a nonuniform N distribution, that confine excitons when the fluctuations are greater than the thermal energy [128]. To quantify the potential fluctuations, a low-temperature "localization energy" was defined as the separation at 10 K between the measured data and a fit of Eq. (5.1) to the high-temperature data [127, 129]. This localization energy can be associated with point defects and inhomogeneities in the crystal, and so serves as a quantification of the crystal quality. A typical value of the 10 K localization energy reported in the literature for "good" quality GaInNAs with 3% N is 7 meV [129].

Our measurements of the $E_g(T)$ dependence of MBE GaInNAs and GaInNAsSb samples grown at Stanford, including those used in this study and many of similar nature, have never shown an "S" shape and deviate only slightly from the Varshni fit. A flattening of the $E_g(T)$ curve below ∼50–70 K is the only manifestation of localization. The 10 K localization energy of our samples ranges from ∼2–7 meV, with reduced localization energy with the incorporation of Sb and/or the use of ion deflection plates during growth [130]. A direct correlation was found between the concentration of grown-in point defects (of various types) and an increased localization energy, supporting the initial interpretation.

Our results indicate an unusually low concentration of defects in the material utilized in this study. Additional details of these results are currently being prepared for publication [130] and will not be expounded upon here, except to mention that the same results are obtained whether the band gap energy is measured with PL or absorption (photocurrent), provided the excitation density is kept sufficiently low in both cases. (For reference, typical values of the Varshni fitting parameters for our material were in the ranges $\alpha \sim 0.4 - 0.6$ meV/K and $\beta \sim 200 - 300$ K. For example, annealed GaInNAs with a band gap of 0.99 eV (1250 nm) was fit by $\alpha = 0.46$ meV/K

and $\beta = 247$ K. The parameters for GaAs are $\alpha_{\mathrm{GaAs}} = 0.5405$ meV/K and $\beta_{\mathrm{GaAs}} = 204$ K [131].)

Because the GaInNAs(Sb) material used in this study was free of excessive defects, as evident from the low localization energy, the effects of N nearest neighbor configurations were well isolated, leading to the elegant results described in this chapter. Since the N–In nearest neighbor reconfiguration is the dominant mechanism of the observed wavelength shift in these samples, the saturation of the shift after sufficient annealing is observed, rather than a continual shift due to a defect-related mechanism. In material with a large concentration of defects, several other non-intrinsic mechanisms may also affect the band gap during annealing. For example, early work suggested that an out-diffusion of N from the quantum wells occurred [31]. In the current material grown in our lab, this out-diffusion has been mitigated by exploiting a new aperture on the N plasma cell that effectively eliminates the incorporation of N interstitials [15]. Other recent work has shown that certain as-yet unidentified damage-induced defects can also cause a band gap shift [35, 132]. However, optimized growth procedures can eliminate or reduce such defects. The N–In nearest neighbor reconfiguration is an intrinsic property of the alloys containing both N and In, modifying the band gap by a thermodynamic process.

Another result of the high crystalline quality of the material used in this study is the presence of relatively sharp exciton peaks in the absorption spectra. These spectra are discussed in detail in Chapter 6 and in Section 5.4 below. Previous work had not revealed the presence of excitonic resonances in GaInNAs at such long wavelengths.

Additional analysis of the PL($T$) data indicates the possible presence of a low-concentration of a sub-gap defect state that appears at low temperatures ($< 65$ K) [133]. The observed defect state may be a N–N pair state in the gap with a binding energy too large to hybridize with the N-band. This hypothesis is consistent with the model developed in Chapter 3 of the spectrum of N pair states in the host crystal's

band gap that interact to form the N-band at sufficiently high N concentration. As the N concentration is increased, the N-band is pushed lower in energy and overtakes the discrete pair states. However, there will likely be one or more discrete states remaining below the N-band (so-called "band tail" states), for many N concentrations. Another possibility for this defect state is a $(\text{N–N})_{\text{As}}$ split interstitial.

## 5.3 Electroreflectance Measurements

Electroreflectance (ER) spectroscopy is a suitable technique for studying the splitting of the band gap states by different N nearest neighbor configurations, due to the technique's intrinsic sensitivity to excited states, as discussed in Section 2.5.2. Electroreflectance spectroscopy also is not very sensitive to variations in the matrix elements, which are expected to be approximately the same for each configuration. (Actually, we find a slight variation of the matrix elements, on the order of 1.5–2.0×, from absorption (photocurrent) measurements presented below in Section 5.4, but this does not have a large effect on the ER results.) Room temperature ER spectra are shown in Fig. 5.3 for a series of variously annealed GaInNAsSb samples. The spectra were taken from the same samples used for the PL data shown in Fig. 5.1 [134]. Each spectrum was analyzed using the methods described in Section 2.5.2, employing the Gaussian lineshape given by Eq. (2.14). Careful fitting was performed to the least number of oscillators that resulted in a good fit for each spectrum, which actually was a non-trivial process. The procedure, described in the next paragraph, was able to fit the spectra extremely well ($R^2 > 0.999$) over the entire energy range of the data.

The spectra at first glance appear to consist of single lines for each HH and LH transition, but very poor fits result from using only one oscillator, even if a lineshape different from Eq. (2.14) is used (i.e., the Lorentzian lineshapes of Eq. (2.10)

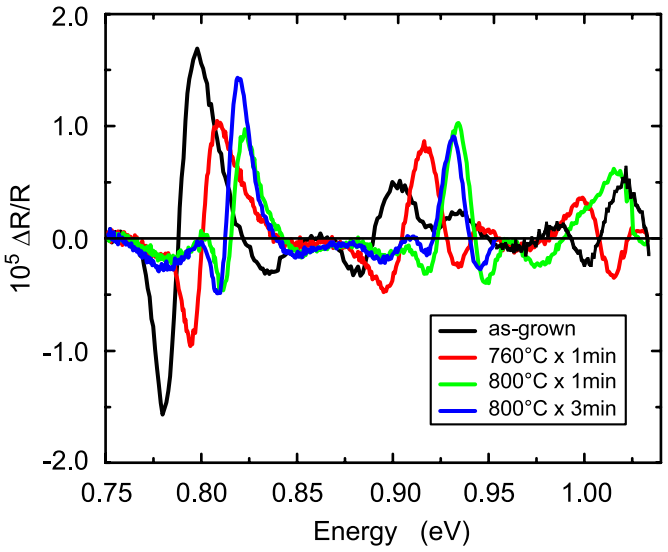


Figure 5.3: (Color) Room temperature electroreflectance spectra taken from variously annealed GaInNAsSb QWs.

with various values of $n$). However, careful fitting with multiple oscillators enabled excellent fitting over the entire measurement range, as demonstrated in Fig. 5.4(a). Care in the fitting procedure is essential to ensure the parameters of the fitted lines do not diverge to unreasonable values and that extraneous lines are not included. The minimum number of oscillators to achieve an excellent fit was always used and attention was paid to parameters such as linewidth during the fitting, to ensure they remained in a physically reasonable range.

Without *a priori* assumptions, the fit transition energies were found to match closely with the peak positions determined by PL [see Fig. 5.4(b)]. The linewidths and lineshape (Gaussian) also matched those from the PL fits. In addition, the linewidth and lineshape also agree with that of the dominant exciton peak observed in photocurrent (absorption) measurements discussed in Chapter 6. The strongest transitions in ER had FWHM of 20–25 meV, while very weak transitions showed broadening up to

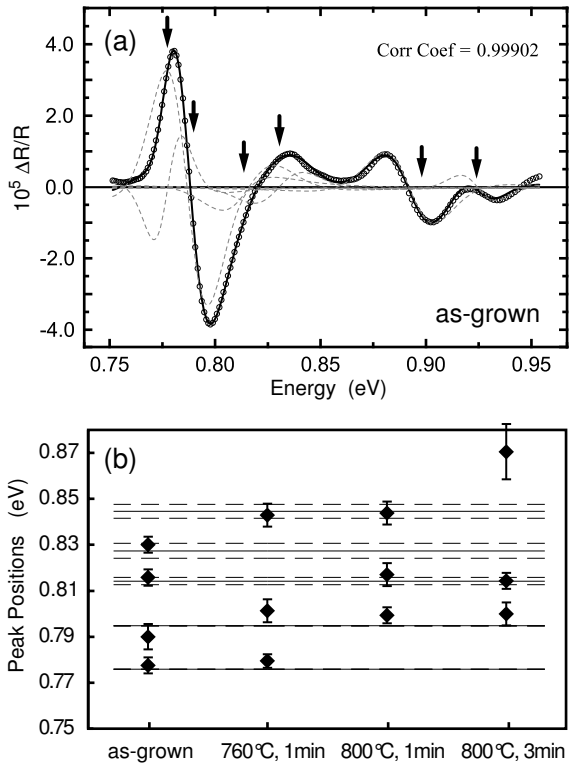


Figure 5.4: (a) Room temperature electroreflectance spectrum from as-grown GaInNAsSb QW (open circles) and theoretical fit (solid curve). Dashed curves show the individual oscillator fits, while arrows indicate the transition energies. (b) Dominant peak positions for HH1 to conduction band transitions obtained by ER (symbols) plotted against the peak fit positions from PL (solid horizontal lines). The dashed horizontal lines demarcate ±1 standard deviation of the PL peak positions.

40–50 meV, consistent with the PL and PC measurements. The independent agreement of the data fitting for the different experimental techniques provides validation of the ER analysis and is also satisfying in the context of the equivalence between absorption and emission as given by the van Roosbroeck-Shockley relation [Eq. (2.3)].

Further refinement of the ER fits, taking into account the PL results as constraints, allowed accurate determination of the fitting parameters for all of the nearest neighbor states in each sample. Figure 5.4(a) reproduces the ER spectrum for the as-grown GaInNAsSb QW sample from Fig. 5.3, with the analysis shown. The arrows indicate the transition energies of the fit oscillators, while the dashed lines shown the individual curve fits. The total fit to the data (thick solid line) is extremely close over the entire energy range, as indicated by the correlation coefficient shown on the figure of greater than 0.999. The main feature(s) around 0.785 eV arises from transitions across the fundmental gap between the first heavy hole (HH1) and first electron (E1) levels, while the smaller features around 0.9 eV arise from both first light hole (LH1) and second heavy hole (HH2) transitions. The nature of the transitions could be determined by analysis of the relative intensities in the ER spectra and observation of the directions of peak shifts when dc bias is applied, along with comparison with calculated energies. Theoretically, a 6:1 ratio of transition strength (peak intensity) is expected for HH:LH transitions in ER, corresponding to a 3:1 ratio in absorption experiments [135]. In practice, the observed ratio can deviate appreciably from this value, which nonetheless remains approximately valid. Additionally, variations in the intensities arise from differences in the wavefunction overlaps of the various transitions (e.g., HH1, LH1, HH2), and generally the amplitudes also get smaller with applied external bias as the wavefunction overlaps decrease with separation of the electrons and holes. Despite these non-idealities, a relatively close agreement to the expected amplitude ratio is observed in the ER spectra for the transitions assigned to HH1 and LH1. Furthermore, the quantum confined Stark effect (discussed in Chapter 6)

leads to a redshift of the energies of odd-numbered transitions (e.g., HH1, LH1, HH3) when an external electric field is applied, but a blueshift of even-numbered transitions (e.g., HH2) [125]. Thus, verification of the assignment of the transitions is obtained by examining a series of ER spectra taken with increasing applied dc bias, or applied electric field, as shown in Fig. 5.5 for the GaInNAsSb QW sample annealed at 760°C for 1 min. In Fig. 5.5, the lowest energy transition is observed to decrease in energy with increasing dc bias (HH1), while the next higher energy transition increases in energy with increasing dc bias (HH2). The third transition, assigned to LH1, decreases in energy with increasing dc bias. Further verification of the assignment of the transitions was obtained by calculating the expected energies of the various quantum confined levels using standard effective mass techniques by interpolating the parameters for the GaInNAs(Sb) system. Non-linear interpolations were used for the band parameters in the calculations [136].

The large separation and spectral independence of the HH1 and LH1 features is clear in the ER data. This has an important implication in that there are no expected transitions in the energy range up to ∼100 meV above the fundamental gap, where we do indeed observe a series of transitions. From the results of the x-ray absorption experiments and *ab initio* band structure calculations discussed earlier in Chapters 3 and 4, we can assign these transitions to the different N nearest neighbor configurations in the crystal, with a monotonic increase in band gap associated with a monotonic increase in the N–In local coordination. The monotonic dependence of the association allows the transitions to be labeled precisely, since exactly five transitions are observed in ER (and PL) and correspond to all of the possible N–In nearest neighbor states. These states are labeled in Fig. 5.1 with "($n$)," where $n = 0$–4 is the number of In atoms locally bonded directly to N.

Incidentally, the splitting of the band gap by the distribution of N–In nearest neighbor bonds present in the material is not unique to the fundamental gap, but

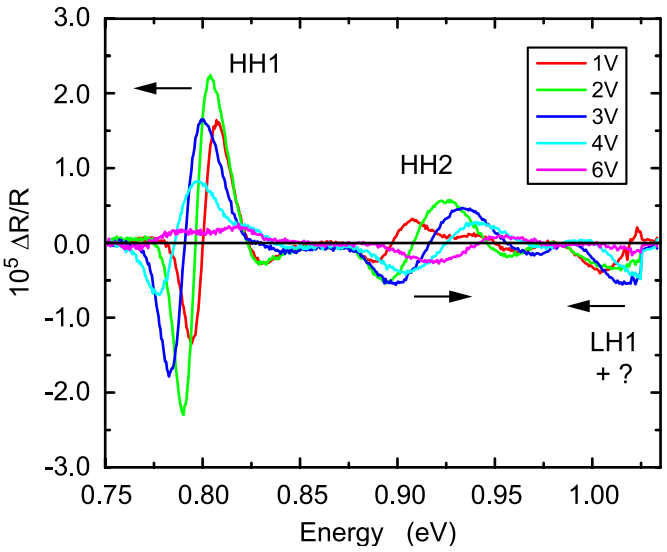


Figure 5.5: (Color) Room temperature electroreflectance spectra taken from GaInNAsSb QW sample annealed at 760°C for 1 min, with different applied dc voltages, showing the characteristic shifts of the quantum confined levels with increasing applied electric field.

is also seen in higher order transitions, such as the LH1→E1 transition. However, the spectrum of states for these higher order transitions often is convoluted by the close proximity of other primary transitions [such as the HH2 transition, as seen in Fig. 5.4(a)]. Only the $E_0$ transition (HH1→E1) occurs in an isolated energy range where the nearest neighbor splitting can be clearly observed. It is possible for defect or trap levels to exist near the fundamental gap (either within or above the gap) which could complicate the analysis, but these do not seem to be present in sufficient concentration to affect the analysis of the present samples.

The exciting consequence of the ability to fit separate oscillators to the individual N–In nearest neighbor states in the ER spectra is that this allows the quantitative extraction of the distribution of nearest neighbor bonds in the material, using a relatively simple experiment and drawing on the results of the x-ray absorption measurements and band structure calculations. Since the states have approximately the same intrinsic matrix element, the relative amplitudes of the oscillators for the nearest neighbor transitions directly determine the distribution of nearest neighbor states in the material. In analyzing the relative magnitudes of the transitions, we take the total amplitude $C = \sqrt{A^2 + B^2}$ as defined in Eq. (2.15). The extracted distributions are plotted in Fig. 5.6 for the as-grown and variously annealed GaInNAsSb samples. The shift in distribution toward increased N–In bonding after annealing is clearly seen. Also plotted in Fig. 5.6 is the calculated distribution for a random arrangement of atoms in material having the same In and N composition as these samples (stars and dashed line). The very close agreement between the random distribution and the distribution measured for the as-grown sample confirms the kinetic nature of the low-temperature MBE-grown material. As the material is annealed, the less thermodynamically-favored $N^{(0)}$ and $N^{(1)}$ states are quickly depleted as high In-coordinated configurations become dominant. The results also show a very good

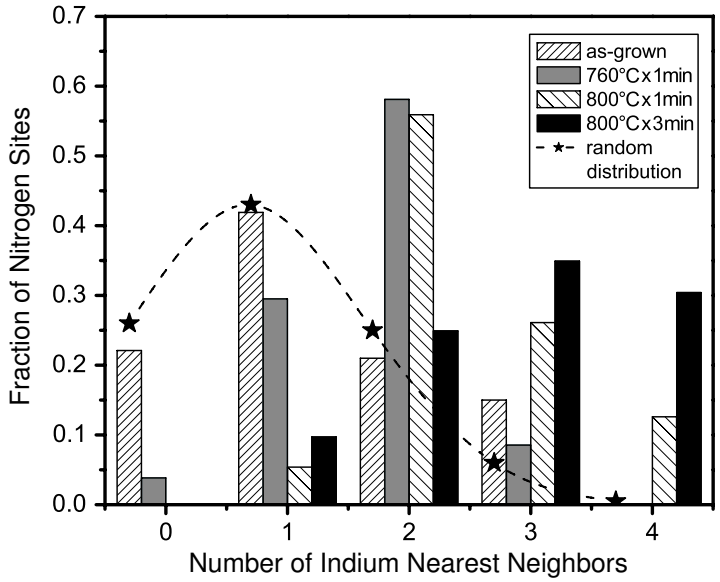


Figure 5.6: Distributions of N–In nearest neighbor bonding in GaInNAsSb QW samples, obtained from fits of ER data. The dashed line and stars indicate the calculated distribution for random bonding, which agrees well with the measured distribution for as-grown material.

agreement with the total energy prediction in Fig. 3.3 that $N^{(2+)}$ states are thermodynamically preferred after annealing. (Here, the notation "$N^{(n)}$" denotes a N environment with $n$ In nearest neighbors, analogous to the $GaInNAs^{(n)}$ notation used to refer to the different calculation models in Chapter 3.

## 5.4 Photocurrent Measurements

Figure 5.7 summarizes the results of photocurrent (absorption) measurements from the same GaInNAsSb samples used in the PL and ER experiments, with the raw responsivity data converted to absorption coefficient. The wavelength region shown only includes transitions from the HH1 band to the conduction band. The excitonic peaks in the absorption spectra were well fit by a Gaussian lineshape with FWHM

$\sim$ 25 meV, consistent with the PL and ER results presented above. These data are discussed in more detail in Chapter 6, concerning electroabsorption and the quantum confined Stark effect, but are reproduced here in the context of analyzing the relative matrix elements of the different nearest neighbor states.

The PC/absorption spectra clearly show discrete peaks corresponding to the transitions found in PL and ER, which are indicated by the vertical lines in the figure, and the higher energy states are seen to grow as the material is annealed. The evolution of states to higher N–In coordination as annealing proceeds is evident. Similar to the PL results, we see discrete jumps between the states, but unlike PL which essentially shows a single peak for the lowest energy transition, PC reveals the relative oscillator strengths (matrix elements) of each of the possible transitions weighted by the distribution of states. The reason PC is sensitive to the oscillator strengths of the transitions is that the technique reflects a direct absorption process of exciting an electron from the valence band into the conduction band. Thus, comparison of the PC data with the distributions of states extracted from ER enables the determination of the relative magnitudes of the different optical transition matrix elements in the samples and relate them to the nearest neighbor states. For example, the data in Fig. 5.7, when compared with Fig. 5.6, show that the $N^{(0)}$ state has a small oscillator strength, since even with significant population of the $N^{(0)}$ state in the as-grown sample (Fig. 5.6), the absorption spectrum is strongly peaked at the $N^{(1)}$ position and shows only a small kink for the $N^{(0)}$ state [Fig. 5.7(a)]. On the other hand, the states with 1 or more N–In nearest neighbors show considerably larger oscillator strengths (particularly for $N^{(2+)}$).

As annealing proceeds, the absorption coefficient at the band edge increases about two-fold as the less optically efficient low-N–In coordinated states are removed and also as defects are removed, resulting in a narrowing of the exciton linewidth to almost 20 meV. Thus, some increase in absorption coefficient can be attributed to

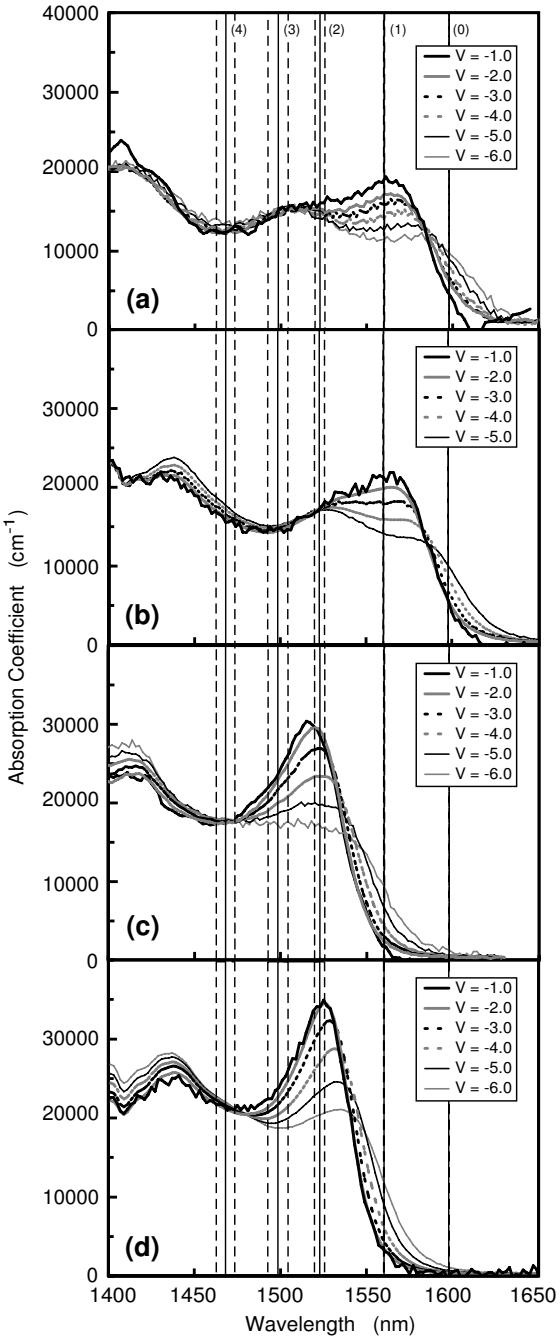


Figure 5.7: Absorption spectra of GaInNAsSb QWs around the band edge region taken with photocurrent, for (a) as-grown, (b) annealed 760°C for 1 min, (c) annealed 800°C for 1 min, and (d) annealed 800°C for 3 min. The vertical lines indicate the positions of the N–In nearest neighbor states, determined from PL and ER.

the removal of nonradiative point defects in the material, but the dominant effect is the increase in oscillator strength with increasing numbers of N–In nearest neighbors, since PC probes the absorption process rather than emission. In PL, which probes the emission process, nonradiative defects dramatically influence the radiative recombination efficiency and observed spectral intensity. After annealing, we observe 10–50× improvement in PL intensity. However, in PC, we only see a 2× increase in absorption coefficient after annealing, owing to the technique's relative insensitivity to the concentration of nonradiative defects other than through exciton linewidth narrowing. Photocurrent is sensitive to the absorption (transition) probability which is proportional to the oscillator strength. From the PC results, then, we conclude that annealing increases the band edge optical transition strength of GaInNAs(Sb) through the redistribution of N–In nearest neighbor states toward those with higher In coordination and higher oscillator strength.

## 5.5 Discussion on Nearest Neighbor Distributions in GaInNAs(Sb)

The ER and PL results, in light of the XAS results and band stucture calculations, and along with the PC results, show a series of five transitions near the fundamental band gap of GaInNAs(Sb) that correspond to the five possible N–In nearest neighbor configurations. The ER results show quantitatively how the nearest neighbor bonding changes as the material is annealed and the band gap blueshifts, a phenomenon observed at least qualitatively with all of the techniques.

For GaInNAsSb, the incorporation of Sb, in addition to N, contributes to the band gap lowering relative to GaInNAs due to the small band gaps of the binary antimonides, but nitrogen bonding still dominates the band edge states of GaInNAsSb,

as in GaInNAs. The two main effects of Sb incorporation, other than the incidental band gap lowering, are improvement in material/interface quality through the reactive surfactant effect of Sb [20] and increase of the valence band offset between QW and barrier. Being a group V element, Sb does not directly influence the N bonding in the material, although an enhancement of N incorporation from the presence of Sb has been observed [34, 137, 138]. The precise effect of Sb as both a surfactant and incorporant in GaInNAsSb is complex and not yet fully understood. Certainly, there are contributions to the attachment and diffusion rate of species (e.g., N and In) on the surface during growth and also an apparent increase in the In sticking coefficient especially during initial layer growth [139], however, the random distribution of as-deposited N–In bonds is not affected by the presence of Sb at our low MBE growth temperatures. The ER results in Fig. 5.6 clearly show the random nature of the as-grown bonding, even when Sb is present. Nevertheless, while the presence of Sb does not play a direct role in the N nearest neighbor bonding in GaInNAsSb, the energy spacing between the nearest neighbor states is found to be about 50% smaller in GaInNAsSb than in GaInNAs, indicating an effect that is not yet understood (perhaps second nearest neighbor related, or perhaps simply a result of the smaller band gap). The measurements on GaInNAsSb indicate a spacing of ∼18–25 meV between nearest neighbor (conduction) band edge states. Our calculations for GaInNAs with comparable N content predict an average energy spacing of ∼34 meV per In atom (Chapter 3), which agrees with measurements that have found a spacing of ∼40 meV or more [140].

The saturation of the PL blueshift with increased annealing (temperature, time, or both) is very important for the practical use of GaInNAs(Sb) in optoelectronic devices such as vertical cavity surface emitting lasers (VCSELs) and resonant cavity modulators. The ability to accurately and reliably predict the peak gain (or absorption) wavelength (related to the peak PL wavelength) is necessary to allow matching

of the material to the VCSEL (or modulator) cavity and specification of the device's operating wavelength. In the past, matching the wavelength has been difficult to achieve since annealing and other thermal processing resulted in a potentially unknown wavelength shift. However, the results of this work show that if the material is "fully" annealed prior to processing, the wavelength will be stable and, furthermore, the amount of the shift from as-grown material can be predicted. The protocol of "fully" annealing the QWs assumes that no intensity degradation results from longer and/or hotter anneals. Steps may need to be taken to prevent degradation of PL intensity at the highest annealing temperatures/times ("rollover"), which sometimes is observed. The precise mechanism of this degradation is not fully understood, but probably has to do with activation of some point defect or in-diffusion of vacancies from the wafer surface. Thick cap layers (which are inherently a part of laser or modulator structures) and high quality interfaces seem to mitigate this effect. Furthermore, employing special techniques during growth to reduce the concentration of grown-in defects, such as As-capping during plasma ignition [35, 36] and the use of ion deflection plates at the N source aperture [35, 141–144], also seems to help.

A further interesting implication of these results is that "partially" annealed material is indeed possible. From a technological point of view, the "fully" annealed state is the most ideal for device design, as described above; however, comparison of the PL and ER results shows that even when the PL wavelength apparently has saturated, the nearest neighbor distributions may still continue to shift. While the ER technique is well suited to measuring excited states and thus was able to produce the distributions shown in Fig. 5.6, PL is most sensitive to the lowest energy transition in the system, since the intraband carrier relaxation rates are much higher than the spontaneous recombination rates and the thermal population of excited states is exponentially lower than the ground state population. Thus, the most dramatic shifts in the PL spectra are observed when a lower energy state essentially disappears. By

examining Figs. 5.1 and 5.6, we see that after annealing at 760°C for 1 min, the as-grown material lost essentially all of the $N^{(0)}$ states and produced a correspondingly large shift in the PL. Similarly, the sample annealed at 800°C for 1 min showed an additional discrete shift in PL as the $N^{(1)}$ state was depleted. However, all of the samples show significant populations of the $N^{(2)}$ state, and no significant further shift is clearly observed in PL after annealing at 800°C for 1 min. Additionally, the peaks in PL are spaced very close together (∼18 meV) compared to their full-widths (∼25 meV), so small changes in the nearest neighbor distributions would not be grossly apparent, as in the case between the samples annealed at 800°C for 1 and 3 min.

Also, it is not clear what the final equilibrium distribution of nearest neighbors should be; the distribution from ER for the furthest annealed sample shows a sort of equalization of the $N^{(2)}$, $N^{(3)}$, and $N^{(4)}$ states. While our calculations show a thermodynamic driving force for increasing the degree of N–In bonding (with a relatively large penalty for having less than 2 In atoms bonded to N), there also is a (composition-dependent) configurational entropy term that drives the distribution wider, assuming the material can be modeled as a random alloy (as opposed to undergoing a second order phase transition to a single most-stable structure.) We also note that early in the annealing process, the $N^{(0)}$ and $N^{(1)}$ states are quickly diminished to very low levels. This is consistent with the calculations shown in Fig. 3.3, where the greatest drop in the total energy of the system occurs between the $N^{(1)}$ and $N^{(2)}$ states.

Another point is that annealing also improves the intrinsic optical activity of the material by increasing the N–In coordination. While the large increase in PL intensity observed after annealing is mostly attributable to the removal of nonradiative recombination centers, the effect of increasing the matrix element for radiative recombination is also an important intrinsic property of the crystalline material. Our band structure calculations (Chapter 3 and Section 4.2) and the x-ray absorption/emission

experiments of Strocov *et al.* [123] show this to be due to an increase in the N-2$s$ density of states near the top of the valence band, and a resulting charge redistribution in energy space, when N is bonded to an increased number of In nearest neighbors. Since N-related states dominate the optical transitions across the band gap and are responsible for the anomalous sharp band gap reduction in the dilute-nitride arsensides, the increase in the density of states with increased N–In bonding leads to better overlap between the band-edge hole and electron states and a higher band-edge optical matrix element. Our absorption/photocurrent measurements directly confirm this prediction by showing that the $N^{(2+)}$ nearest neighbor states have stronger matrix elements than the low-In coordinated states.

Finally, it is worthwhile to comment on how the atoms in the crystal diffuse to achieve the short-range rearrangement upon annealing. Our results suggest that annealing involves the diffusion of In atoms and perhaps not necessarily N atoms. Figure 3.2 shows that there are just about enough randomly distributed $N^{(3)}$ sites to accommodate all of the N, but there are practically no $N^{(4)}$ sites. Since the final material has a distribution of coordinations including $N^{(4)}$, the diffusion of In is necessary to create those sites. Additionally, if only N atoms diffused, relatively long range motion of the atoms would be necessary for them to reach a $N^{(3)}$ site, whereas only short hops by In would be sufficient to convert many sites to higher In coordinations. Furthermore, other studies that agree with our results were performed on low In-content material, where the likelihood of randomly occurring $N^{(3)}$ sites is very much diminished [118, 140, 145].

At first glance, one might think that N is much more mobile in the lattice than In due to its small size, but this is not necessarily the case. Since In is so large relative to the other atoms and the material is compressively strained, elasticity theory provides for a driving force for the motion of In (conceptually, the In atoms are squeezed by the matrix). In fact, rapid diffusion of In is known to occur in GaInAs, mediated

predominantly by second nearest neighbor hopping via triply-negatively charged Ga or In vacancies, similar to the Ga self-diffusion in GaAs [146, 147]. On the other hand, N diffusion in GaInNAs probably occurs via As vacancies. Systematic studies of the diffusion of N and In in GaInNAs could be pursued in the future to clarify this issue and could take advantage of variations in the As vacancy concentration that can be achieved by varying the As over-pressure during growth.

# Chapter 6

# Quantum Confined Stark Effect of GaInNAs(Sb) Quantum Wells

## 6.1 Introduction

We wish to explore the use of GaInNAs(Sb) quantum wells (QWs) in the active region of electroabsorption modulators. The mechanism of optical modulation employed in these modulators is the quantum confined Stark effect (QCSE), which in essence refers to the redshift of the QW band gap or absorption edge upon application of an electric field perpendicular to the wells [125]. The band gap redshift arises from modification of the QW potential by the electric field to induce shifts in the quantized energy levels within the well. Since the carriers are confined by the quantum well barriers, exciton ionization and consequent broadening of the absorption edge is suppressed when the field is applied, leading to a sharp shift of the edge. The mechanism of the QCSE is illustrated in Fig. 6.1.

To determine the efficacy of GaInNAs(Sb) QWs for optical modulators, absorption spectra were measured from *p-i-n* diode samples using the photocurrent technique as described in Section 2.4. A description of the technique as well as theory of the analysis are presented in Section 2.4. The growth and fabrication of the test devices were described in Section 2.1. Measurements were performed for both GaInNAs/GaNAs

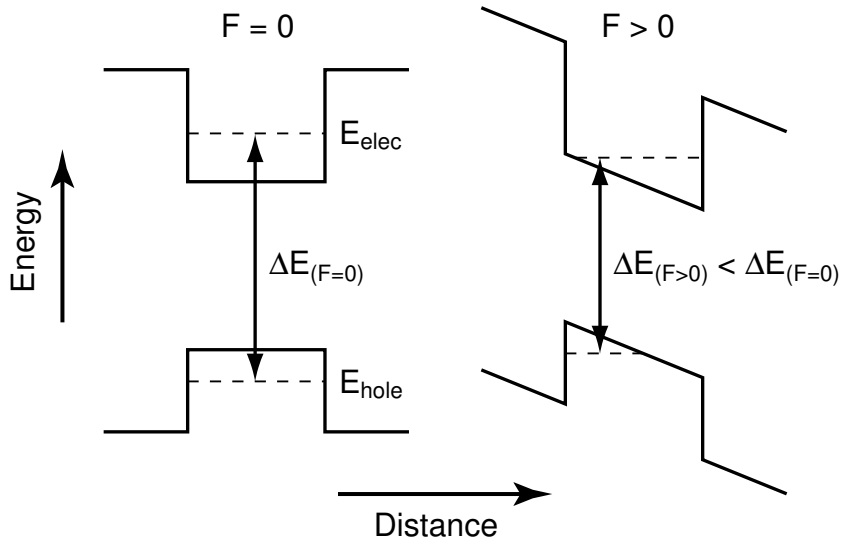


Figure 6.1: Illustration of the mechanism of the QCSE. When an electric field, $F$, is applied across the QW potential (right figure), the quantized energy levels indicated by the dashed lines "fall into the wells," and the effective band gap decreases.

and GaInNAsSb/GaNAs QWs, tuned for ∼1300 nm and ∼1550 nm operation, respectively. The GaInNAs samples contained 9 QWs, while the GaInNAsSb samples contained 3 QWs. Both as-grown and annealed samples were examined.

To demonstrate QCSE behavior suitable for optical modulation, measurements were performed at room temperature in ambient environment. Applied electric fields up to 78 kV/cm (corresponding to reverse bias voltages up to 9 V) were used to observe the QCSE of the QWs. In addition, spectra were taken at various temperatures from 20–295 K to study the temperature dependence of the exciton broadening, the variation of band gap with temperature (in conjunction with photoluminescence measurements), and the relative rates of carrier trapping and emission. At low temperatures, the population of phonons is decreased, leading to a reduction in linewidth since phonon scattering is the dominant exciton dissociation mechanism that determines

the exciton lifetime and thus the linewidth, through the Heisenberg uncertainty principle. More precisely, the scattering processes from phonon absorption are reduced at low temperatures due to the reduced number of phonons, but phonon emission is not affected. However, energy conservation forbids phonon emission from the fundamental gap state, thus this broadening process only affects excited states (e.g., the second quantized electron level in the QW). Phonons freeze-out at very low temperatures, and phonon scattering may no longer dominate the exciton lifetime. In this very low temperature regime, the lifetime (and linewidth) may be limited by the effects of point defects and dislocations, for example, as well as well-width fluctuations and alloy broadening.

Lineshape analysis of all of the optical measurements (PL, EL, ER, PC) shows a Gaussian broadening of the exciton at room temperature and also persisting to very low temperatures ($\sim$15 K). Ordinarily, bulk semiconductors at room temperature are in the "low temperature" regime, which exhibits Lorentzian exciton broadening [51]. It has been shown that quantum confinement can cause Gaussian broadening of multiple quantum well excitons at room temperature (e.g. GaAs/AlGaAs MQWs) [125], however at lower temperatures the broadening becomes Lorentzian. For GaInNAs(Sb), the large exciton mass, large exciton radius, and intrinsic lattice defects cause a strong exciton-phonon coupling that dominates the exciton lifetime even at low temperatures with a small population of phonons. The factors that cause strong exciton-phonon coupling correspond to an effective increase of the lattice temperature [51]. Incidentally, measurement of the lineshape for the GaAs substrate reveals a Lorentzian broadening even somewhat above room temperature. In our simulations of the QCSE that take into account excitonic effects, the broadening is assumed to occur via absorption of a single phonon by an electron at the bottom of the conduction band [136]. The lifetime determined in this way agrees reasonably well with the measured broadening.

Representative raw photocurrent spectra taken from a GaInNAs/GaNAs multiple (9) quantum well sample at various temperatures from 25 to 285 K are shown in Fig. 6.2. We can immediately see the blueshift of the band gap as the temperature is decreased due to the thermal contraction of the lattice (following closely the Varshni model [126]). We also observe a general decrease in the magnitude of the measured photocurrent as the temperature is lowered due to increased carrier trapping and consequent reduced internal quantum efficiency. In addition, a sharpening of the absorption features (exciton resonances) occurs as the temperature is lowered and phonon scattering is reduced, as discussed above. The reduction of linewidth with temperature is not as dramatic as is observed with more typical materials, for example InGaAs/InP QWs [148], indicating that intrinsic lattice defects in the GaInNAs(Sb) alloy begin to limit the exciton lifetime at relatively high temperatures ($\sim$50–100 K), rather than phonon scattering. This is consistent with the temperature dependence of the linewidth in photoluminescence, which begins to level off to a constant value below $\sim$150 K, indicating the onset of phonon freeze-out which should occur at approximately half the Debye temperature, $\Theta_D$. For GaInNAs(Sb) alloys with 20–40% In and less than $\sim$5% N and/or Sb, we estimate $\Theta_D \sim$ 330–340 K from a linear interpolation between the endpoint binary compounds.

Generally, photocurrent data is more meaningfully displayed as responsivity versus photon energy, as shown representatively in Fig. 6.3. The data in this form is directly related to the absorption coefficient and can readily be converted to a spectrum of absorption coefficient versus energy (or wavelength) using the formulae derived in Section 2.4.2, with knowledge of the optical interaction length in the sample. As mentioned in Section 2.4.2, proper accounting of the incident power on the device, including effects of Fresnel reflection from the multilayer stack, is important for accurate determination of the responsivity (and absorption coefficient), especially over a wide spectral range. A representative reflectivity measurement from the surface of a

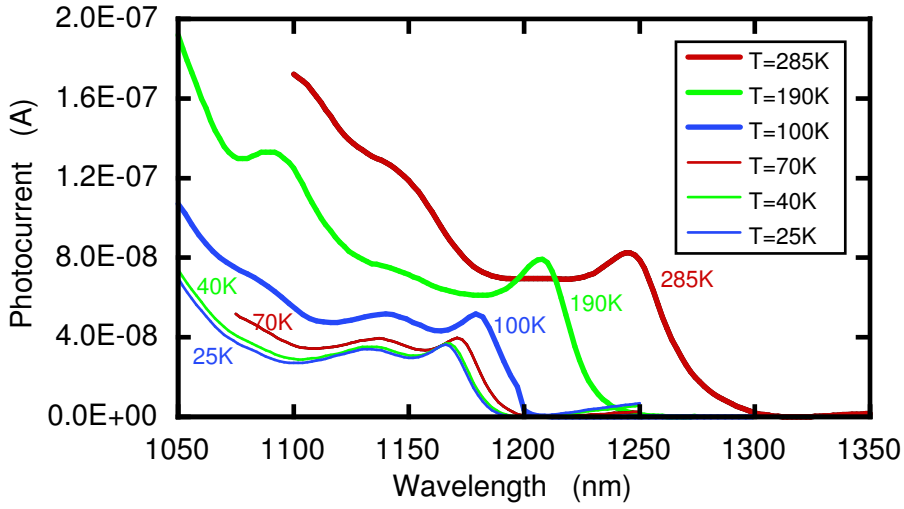


Figure 6.2: (Color) Sample raw photocurrent spectra taken from GaInNAs/GaNAs multiple quantum wells at various temperatures, with approximately 360 nW incident power on the device and −1 V bias.

GaInNAs QW *p-i-n* diode sample, used for such calibration, is shown in Fig. 6.4. Most of the spectra displayed in the following sections have been converted to absorption coefficient for clarity and to facilitate analysis of expected device performance.

## 6.2 Photocurrent Results

### 6.2.1 GaInNAs/GaNAs Quantum Wells

For device operation around 1300 nm, GaInNAs/GaNAs QWs were used with a composition of approximately 30% In and 1.6% N in the QWs, and 2.0% N in the barriers. These samples contained 9 QWs 80 Å thick with 200 Å thick barriers. The *p-i-n* diode sample structure was as described in Section 2.1.2.

Figure 6.5 shows the measured room temperature absorption spectra for these GaInNAs QWs around 1300 nm [23]. The family of curves represents applied reverse

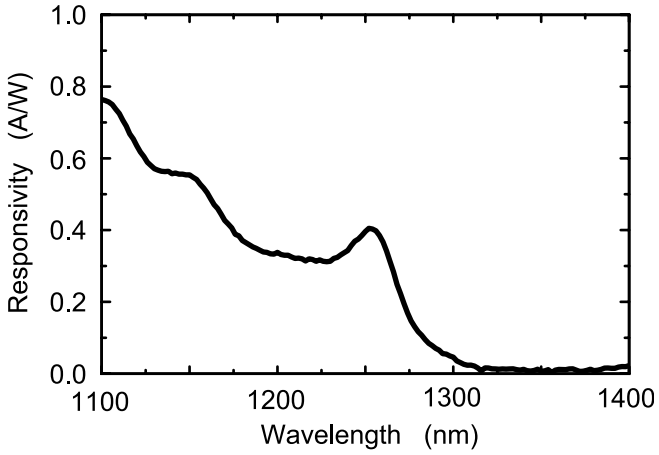


Figure 6.3: Sample photocurrent data from GaInNAs/GaNAs QWs with 1 V reverse bias applied, plotted as responsivity versus incident photon energy.

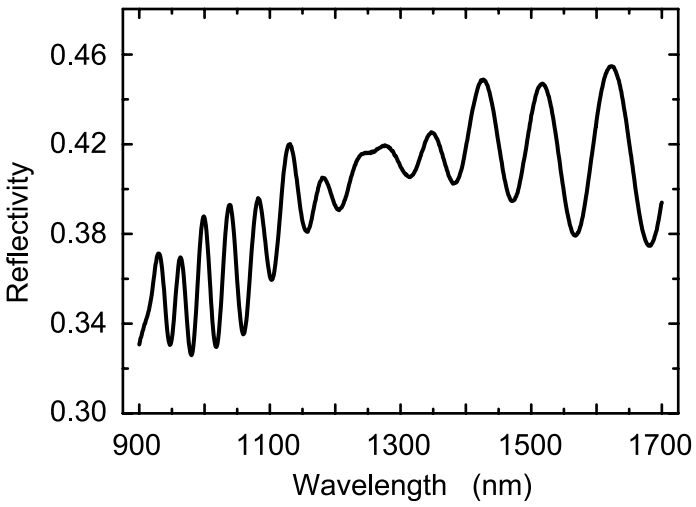


Figure 6.4: Representative normal-incidence reflectivity data taken from a GaInNAs/ GaNAs QW *p-i-n* diode sample, used for proper calibration of incident optical power on the device and converting the measured photocurrent to responsivity or absorption coefficient.

biases of 0–7 V, corresponding to electric fields of 20–70 kV/cm across the QWs, as indicated on the figure. The value of electric field corresponding to the applied voltage bias was calculated using the depletion approximation, as described in Appendix C. Examination of the behavior at electric fields smaller than the built-in field, by using small positive voltage biases (<1 V), yields spectra very similar to that for 0 V bias. In any case, with such small electric fields, the low signal-to-noise ratio due to reduced carrier collection efficiency makes accurate determination of the edge shape and onset difficult.

The results for both as-grown material [Fig. 6.5(a)] and material annealed after growth at 720°C for 1 min [Fig. 6.5(b)] are shown. Quantum confined Stark effect behavior is observed in both cases, with a clear improvement after annealing, which also results in a 2× increase in absorption coefficient. The exciton resonance peaks also become sharper after annealing, from ∼30 meV to ∼25 meV Gaussian FWHM, as the exciton lifetime is increased from the removal of crystal defects. Furthermore, the absorption edge (band gap) is observed to shift to shorter wavelengths after annealing. This well-known phenomenon has already been discussed extensively in this dissertation, and in these samples is caused dominantly by a redistribution of N nearest neighbor bonds from mostly N–Ga to mostly N–In as discussed in Chapters 3–5 and Refs. [16, 30, 42, 134].

These data represent the first report of sharp excitonic absorption and the QCSE in GaInNAs material in this wavelength range. Figure 6.5 shows a region from ∼1210–1320 nm where the absorption coefficient is strongly dependent on applied bias. The peak absorption coefficient of ∼18,100 $cm^{-1}$ at 1250 nm for the annealed sample is a record for GaInNAs, which along with the sharp exciton peaks is indicative of very high crystalline quality. Here, we define absorption coefficient for a multiple quantum well sample as in Eqs. (2.4) and (2.5), where both the barriers and QWs are included in the interaction length and a bulk-like exponential decay of intensity through the

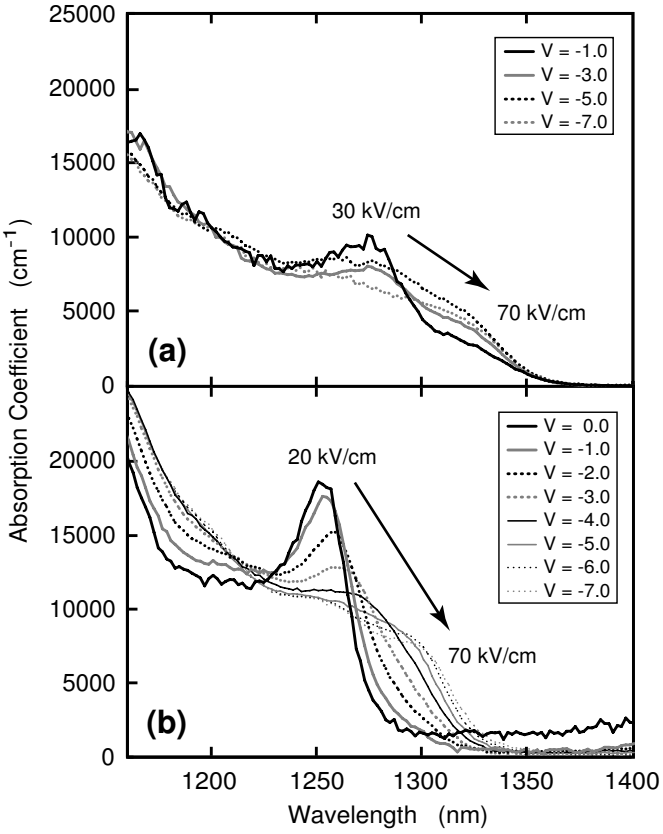


Figure 6.5: Room temperature absorption spectra from GaInNAs/GaNAs QWs with varying perpendicular applied electric fields, for (a) as-grown material and (b) material annealed at 720°C for 1 min. Clear QCSE behavior around 1300 nm is evident.

QWs is assumed. We observe persistently sharp absorption edges even with applied fields as high as 70 kV/cm. Only one previous report showed exciton absorption for GaInNAs QWs, with a peak absorption coefficient at 1150 nm of ∼9,000–10,000 $cm^{-1}$, for material grown by OMVPE [149]. The excellent material quality of our MBE-grown GaInNAs was accomplished through years of growth optimization, including plasma tuning (cell pressure from $N_2$ flow rate and aperture design; use of pure rather than diluted $N_2$), growth temperature optimization, minimizing oxygen impurities, etc. as described in Section 2.1.1. The growth optimizations resulted in material with a low concentration of intrinsic defects, as evidenced by temperature-dependent PL measurements (see Section 5.2).

Low temperature absorption measurements show sharper features and also accentuate the nearest neighbor splitting of the band gap with the appearance of peaks at high energies (shorter wavelengths) in the photocurrent spectra that track the band gap shift with applied bias. Spectra taken at 70 K and 100 K are shown in Fig. 6.6, where the data are shown as raw photocurrent (arbitrary units). The reduced broadening of the spectra at cryogenic temperatures further demonstrates very high quality quantum confined Stark effect, with exciton peaks having FWHM ∼13 meV at 70 K.

Finally, Fig. 6.7 shows a few representative spectra acquired over a wide wavelength range. High frequency oscillations, most obvious at the shorter wavelengths, can be seen throughout the spectra. These oscillations arise from interference of reflections from the various layers in the structure and demonstrate the necessity of calibrating out the reflectivity contribution to the input optical power, as mentioned above. The absorption at short wavelengths well above the band gap is not affected by applied electric field, and the spectra for the various biases fall on top of each other in the short-wavelength region. This fact can be used to scale the low-field spectra that suffer from low internal quantum efficiency, to match the short wavelength absorption from the high-field spectra, thus correcting for non-unity internal quantum

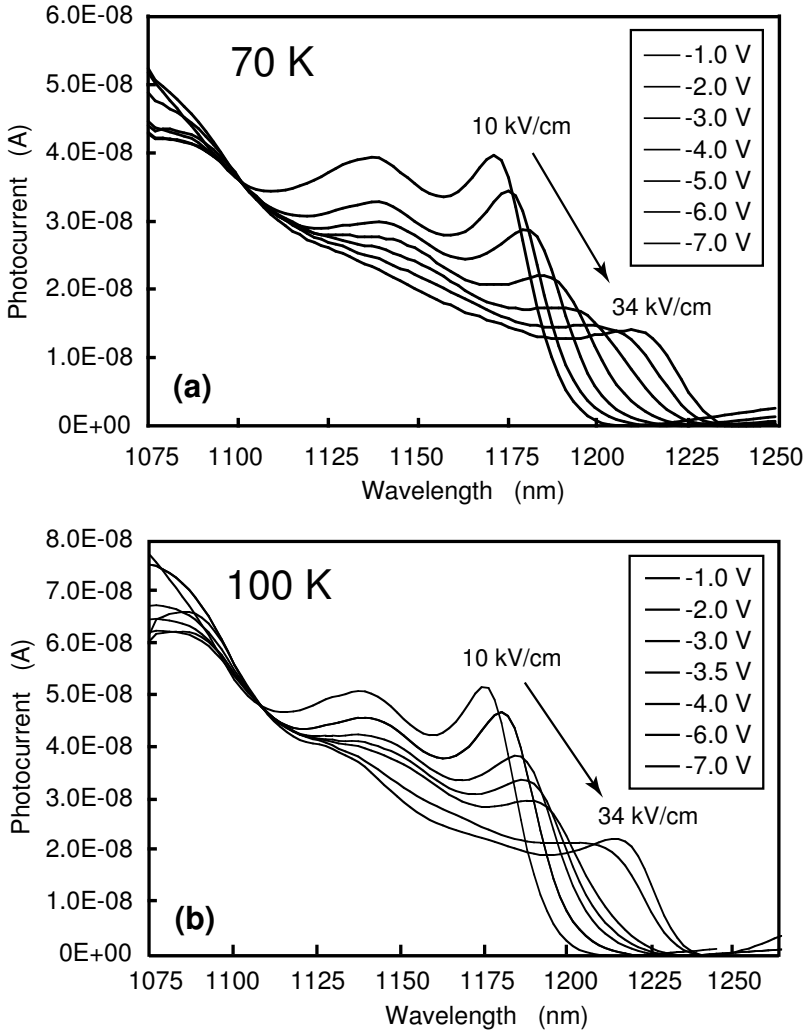


Figure 6.6: Low temperature photocurrent spectra from GaInNAs/GaNAs QWs with varying perpendicular applied electric fields, taken at (a) 70 K and (b) 100 K.

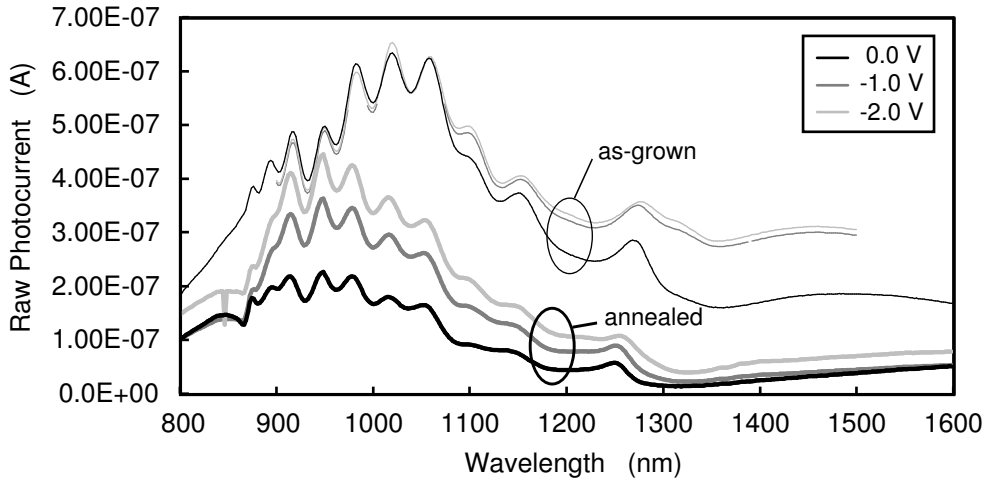


Figure 6.7: Photocurrent spectra taken from GaInNAs/GaNAS QWs at room temperature over a wide wavelength range. Fresnel reflections from the layered device structure and low internal quantum efficiency at low bias voltages are demonstrated.

efficiency.

### 6.2.2 GaInNAsSb/GaNAs Quantum Wells

For device operation around 1500 nm, GaInNAsSb/GaNAs QWs were used with a composition of approximately 40% In, 2.5% N, and 2.7% Sb in the QWs, and 2.7% N in the barriers. These samples were grown with 3 QWs 80 Å thick separated by 200 Å thick barriers, and employed the As-capping technique described in Section 2.1.1 to protect the active region from damage during growth due to N plasma ignition. The active region was grown in the center of a *p-i-n* diode sample structure described in Section 2.1.2.

Figure 6.8 shows the measured room temperature absorption spectra for GaInNAsSb QWs with various applied electric fields [23]. For these samples, applied reverse biases of 1–6 V correspond to electric fields of 30–63 kV/cm. The figure shows results for a series of different thermal annealing conditions: (a) as-grown, (b) 760°C for 1 min,

(c) 800°C for 1 min, and (d) 800°C for 3 min. The region from ∼1500–1610 nm shows strong dependence of the absorption coefficient on applied bias voltage.

As with the GaInNAs samples, the absorption coefficient nearly doubles after the longest anneal. However, more notable is the fact that the peak absorption coefficient for the as-grown GaInNAsSb sample is comparable to the peak value measured for the annealed GaInNAs sample, and after annealing the peak GaInNAsSb absorption coefficient at wavelengths around 1550 nm reaches a value (∼34,800 $cm^{-1}$) much higher than that reported for the competing InGaAs(P) material system grown on InP [148, 150, 151]. In addition, the maximum positive change in absorption coefficient with applied electric field for a single wavelength (∼10,000 $cm^{-1}$ around 1560 nm), a critical parameter for modulator device performance, is similar to or significantly larger than for competing InGaAs/InGaAsP QWs, depending on the quality of the InGaAs material.

The data shown here represents the first demonstration of the QCSE in the 1550 nm wavelength range for a material grown on GaAs, and particularly the first report of sharp exciton absorption for GaInNAsSb material. Similar to the GaInNAs results presented in the previous section, the FWHM of the Gaussian-broadened exciton peaks of the annealed GaInNAsSb QWs at room temperature was measured to be less than 25 meV. This is only slightly broader than the 15 meV FWHM reported for room temperature InGaAsP on InP at 1550 nm [148], which does not suffer broadening from nearest neighbor disorder. At temperatures around 25–70 K, the FWHM for GaInNAsSb is reduced to ∼10–15 meV. At high applied electric fields, a relatively sharp exciton peak is still observed even at room temperature, as seen in Fig. 6.8. For example, with applied electric field of 63 kV/cm, the FWHM is ∼35 meV. The decreased rate of field ionization of excitons in the GaInNAsSb/GaNAs QWs compared to the GaInNAs/GaNAs QWs results from the better hole confinement in the Sb-containing QWs from the increased valence band offset. On the other hand, the

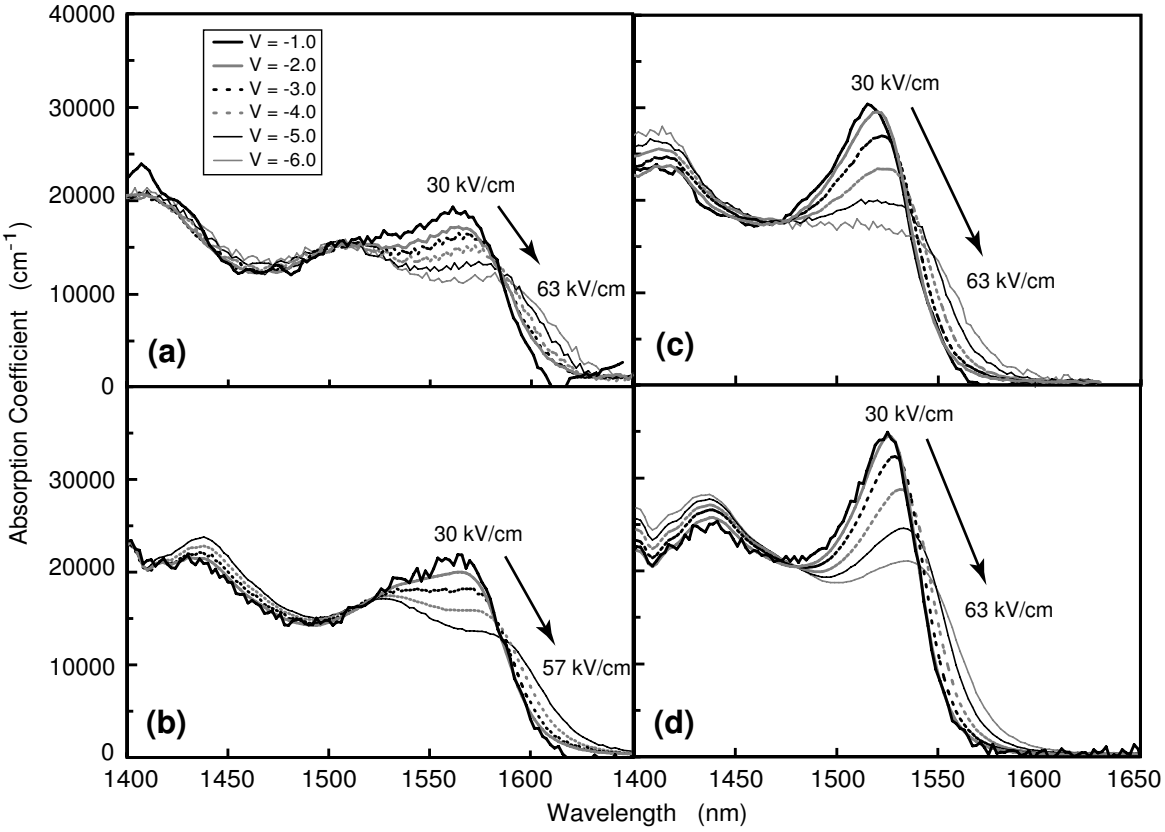


Figure 6.8: Room temperature absorption spectra from GaInNAsSb/GaNAs QWs with varying perpendicular applied electric fields, for (a) as-grown material and material annealed at (b) 760°C for 1 min, (c) 800°C for 1 min, and (d) 800°C for 3 min. Clear QCSE behavior around 1550 nm is evident.

lower electron effective mass of GaInNAsSb compared to GaInNAs reduces the magnitude of the absorption shift with applied electric field via the QCSE. However, as will be shown, the expected performance of a modulator device using GaInNAsSb in the active region is not adversely affected, due to the very strong, sharp absorption features. The lighter electron mass may however contribute to a higher required voltage for modulator device operation.

## 6.3 Discussion of Photocurrent Results

The large values of absorption coefficient measured for the GaInNAs(Sb) system, compared to more typical materials used for optoelectronic devices in the 1200–1600 nm wavelength range, are mainly a consequence of the large electron effective masses of the dilute-nitride arsenides [on the order of 0.08–0.12 $m_0$ (see Section 3.2.2), or about 50% higher than for GaAs, for example] leading to an increased band edge joint density of states as the electron and hole effective masses are better matched. The $E_P$ parameter is not expected to differ very much for GaInNAs(Sb) from the typical values for most III-V semiconductors ($\sim$20–28 eV [131]). The observed $\sim$3$\times$ improvement in absorption probability for the GaInNAs(Sb) system compared to competing materials comes from band structure effects (effective mass and wavefunction overlap in the QWs). An additional unique feature of this material system is the large separation of heavy hole (HH) and light hole (LH) confinement energies in the QWs, on the order of 100–120 meV or more between the HH1 and LH1 transitions (see Section 5.3). This large energy separation of the hole states leads to the band edge absorption being strictly HH to electron in nature. The band edge absorption is sharper, because a nearby LH transition does not convolute the spectrum, as in GaAs/AlGaAs QWs, for example. However, an additional band-edge broadening mechanism exists for the GaInNAs(Sb) system, from the N nearest neighbor splitting

of the band gap. In GaInNAs, the nearest neighbor states are spaced by ∼40 meV, and in GaInNAsSb, by ∼20–25 meV, which is near the room temperature broadening of the exciton peaks from phonon scattering.

## 6.4 Optical Modulator Application

### 6.4.1 Predicted Device Performance

Two possible operating regimes for the modulator exist: the "normally on" regime at wavelengths longer than the exciton peak and the "normally off" regime at wavelengths shorter than the exciton peak. For wavelengths slightly above the exciton peak, the absorption coefficient is seen to rise with the application of external bias, for "normally on" operation; below the exciton peak, the absorption coefficient is lowered by the bias, for "normally off" operation. In general, it is desirable to operate in the long-wavelength "normally on" region to minimize device insertion loss and maximize contrast ratio. By examining Figs. 6.5 and 6.8, we can see that in the "normally on" region, a large absolute absorption change $\Delta\alpha$ is accompanied by a large ratio of $\alpha_{\max}/\alpha_{\min}$ because of the very small $\alpha_{\min}$. In addition, the small absorption in the "on" or 0 V state minimizes the insertion loss. On the other hand, in the "normally off" region, although a slightly larger $\Delta\alpha$ can be achieved by operating at the wavelength of the 0 V exciton peak, the $\alpha_{\max}/\alpha_{\min}$ ratio is low due to considerable absorption in the "on" state. Additionally, a large fraction of the input optical power is absorbed by the device even in the "on" state of the "normally off" modulator, leading to a large insertion loss. In the discussion that follows, we assume "normally on" operation.

Generally, two practical configurations for a modulator device are feasible. In a reflection (or transmission) configuration, the electroabsorptive properties of the

QWs are used to modulate the amplitude of light reflecting off the device's surface (or transmitting through the device) by applying a voltage across the device. Alternatively, a waveguide configuration can be used, where a voltage applied to the device changes the absorption of the QWs in the waveguide and modulates the light propagating through the waveguide. The reflection configuration is especially attractive for optical interconnect and other optical computing applications, since the fabrication of 2D arrays is facilitated. The waveguide approach may be more suitable for use in integrated optical circuits. Some disadvantages of the waveguide approach are polarization-sensitivity, larger wafer real estate required, inability to form 2D arrays, more difficult input/output coupling, and difficulty in scaling to very high speeds due to the large device area. However, waveguides allow engineering of the interaction length independently of growth thickness. A novel combination of the waveguide and reflection approaches might also be possible to tradeoff the advantages of each configuration [152].

Incidentally, a transmission configuration, where light passes through the QWs at normal incidence and is modulated by voltage-control of the absorption, is feasible in principle, although such devices have been shown to always operate non-optimally compared to reflective devices [153]. However, in some integrated device architectures, such as a continuous-wave vertical cavity laser (VCSEL) integrated with a vertical cavity external modulator, a transmission modulator might still be desired; its operation is similar to a reflective device.

From the measured electroabsorption properties of the QWs, we can estimate maximum expected device performance, if a device architecture is chosen. For illustration, an asymmetric Fabry-Perot reflection modulator configuration [153–159] will be discussed here. This architecture takes advantage of the absorption changes from the QCSE to modulate the intensity of reflected light from the device, but also utilizes a resonant cavity to enhance the contrast ratio. There are also intrinsic advantages

to using this high-contrast, reflective configuration, for both telecommunication and optical interconnect applications, in terms of speed, compact arrayability, low power consumption, and chirp-free operation [160].

The general principle of the asymmetric Fabry-Perot reflection modulator, shown schematically in Fig. 6.9, involves using a resonant cavity with different (asymmetric) front and back mirror reflectivities. By introducing a variable loss into the cavity (e.g., voltage-controlled absorption through the QCSE), the cavity loss can be tuned to exactly compensate the difference in mirror reflectivities, in effect yielding a symmetric cavity for a specific value of loss. In the symmetric case, the cavity resonance yields 100% (transmission + absorption) through the device for a specific wavelength and incident angle, and hence 0% reflection. With the loss tuned to some other value, the cavity becomes asymmetric and there is finite reflectivity. With proper design, the device can achieve very high contrast ratio; indeed the idealized illustration just given would yield infinite contrast ratio for a perfectly-tuned device.

Optimization of the front mirror reflectivity $R_f$ and back mirror reflectivity $R_b$ to the absorption characteristics of the QWs in the cavity allows the realization of high contrast ratio devices. Normally, we wish to design the bottom mirror reflectivity to be near unity, so that the loss from reflection off the back mirror is small compared to the minimum absorptive loss in the cavity from the QWs, simplifying operation and also minimizing insertion loss [153, 161]. Then, for a chosen operating wavelength and voltage swing, the front mirror reflectivity is the main design degree of freedom. Generally, the optimum choice for $R_f$ would be to match $(1 - \alpha_{\max})$ in the cavity, so that in the "off" state the cavity is on resonance and the reflectivity is zero (i.e., infinite contrast ratio). This condition requires that

$$R_f = R_b \exp(-2\alpha_{\max} L), \tag{6.1}$$

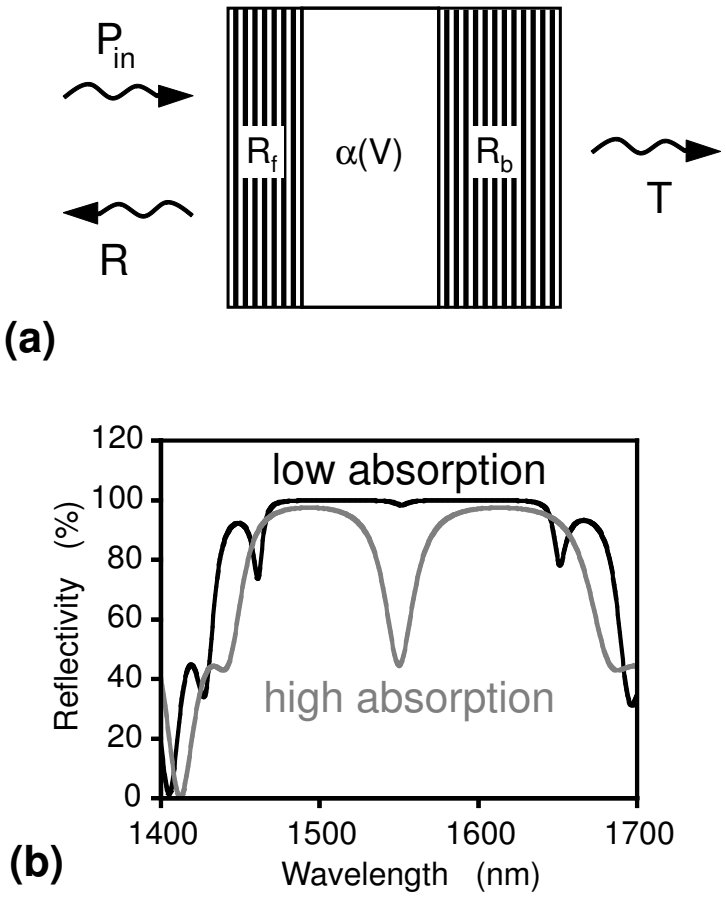


Figure 6.9: (a) Schematic of an asymmetric Fabry-Perot reflection modulator structure, where $R_f$ and $R_b$ refer to the front and back mirror (DBR) reflectivities, respectively; $R$ and $T$ denote the fraction of input optical power $P_{in}$ that is reflected and transmitted, respectively, by the device. A voltage-controlled loss in the cavity is represented by $\alpha(V)$. (b) Representative reflectivity spectra illustrating its operation, with the labels referring to the tunable absorption, or loss, in the cavity.

where $L$ is the interaction length through the QWs and $R_b$ is assumed to be 1. Generally, a higher $R_f$ will lead to lower insertion loss and a higher contrast ratio, but also a higher cavity finesse which undesirably reduces the optical bandwidth of the device, exacerbating its temperature sensitivity.

In the general case, the "matching condition" of Eq. (6.1) is not exactly satisfied, and there is a tradeoff between modulation ratio and insertion loss, and also the optical bandwidth of the device. Additionally, perfect matching is only possible for a single wavelength and incident angle, and incoming wavepackets always possess some bandwidth in wavelength, as well as a range of angles dependent on the degree of focusing. Moreover, index changes induced in the material through the Kramers-Kronig relation when the absorption is changed by the QCSE forbid maintaining the perfect matching condition during device operation, and infinite contrast ratio is not achieved in practice. Furthermore, optimization of the QW absorption characteristics and choice of operating wavelength affects this tradeoff. By maximizing the ratio $\alpha_{\max}/\alpha_{\min}$, the modulation ratio is improved while reducing the insertion loss. However, a large $\Delta\alpha$ and/or a shorter cavity leads to higher optical bandwidth as well as lower operating voltage. No attempt has been made in this work to optimize the QWs for maximum QCSE or contrast ratio, and better performance is expected by improving the absorption characteristics in Figs. 6.5 and 6.8 using techniques found in the literature [162, 163], such as using coupled asymmetric QWs.

The key parameters for device performance include the maximum and minimum values of $\alpha$ at the operating wavelength for a given voltage swing, the difference $\Delta\alpha = \alpha_{\max} - \alpha_{\min}$, and also the ratio $X = \alpha_{\max}/\alpha_{\min}$. The extraction of these parameters from the absorption data in Figs. 6.5 and 6.8 is shown more clearly by replotting the data in the traditional manner for electroabsorption, as in Fig. 6.10, where the spectra show the change in absorption coefficient at each bias point relative to the 0 V spectrum. To maximize contrast ratio and minimize insertion loss, a "fully

on" state is desired with $\alpha_{\min} \sim 0$, so operation at wavelengths slightly higher than the zero field absorption edge is favorable, as opposed to operation at the exciton peak, as discussed above.

The plots in Fig. 6.10 clearly show the suitability of GaInNAs and GaInNAsSb QWs for optical modulation at 1300 and 1550 nm, respectively, with operation in the favored long-wavelength lobe of the electroabsorption spectra. The figure also shows that the as-grown GaInNAsSb sample is suitable for modulation at wavelengths reaching beyond 1600 nm. For the annealed GaInNAs sample, the change in absorption coefficient at 1300 nm is $\Delta\alpha = 7135 - 1400 = 5735$ cm$^{-1}$ for a 0–5 V swing. For the annealed GaInNAsSb sample, $\Delta\alpha = 15,062 - 5868 = 9194$ cm$^{-1}$ at 1550 nm, while for the as-grown GaInNAsSb sample, $\Delta\alpha = 6945 - 383 = 6562$ cm$^{-1}$ at 1610 nm, both for a 0–6 V swing. The change in $\alpha$ near 1550 nm of almost 10,000 cm$^{-1}$ for the annealed GaInNAsSb, with applied bias of 6 V (63 kV/cm total field, or 43 kV/cm change in electric field from 0 V), is notably higher than typical InGaAs/InGaAsP active regions on InP [148, 150, 151]. Moreover, the QWs shown here were not specifically optimized to maximize the QCSE and improved performance should be possible by utilizing techniques described in the literature [162, 163].

From the values quoted above at the specified operating wavelengths, we can calculate the required $R_f$ values to fulfill the matching condition, as $R_f = 0.55$, 0.82, and 0.73, for the annealed GaInNAs at 1300 nm, as-grown GaInNAsSb at 1610 nm, and annealed GaInNAsSb at 1550 nm, respectively. The maximum on-state reflectivity ($R_{\text{on}}$) from the device is derived in Ref. [153] and is given by

$$R_{\text{on}} = \left( \frac{r_f - r_f^{1/X}}{1 - r_f^{1+1/X}} \right)^2 , \tag{6.2}$$

where $r_f$ is the front mirror electric field reflectivity ($R_f = r_f^* \cdot r_f$) and $X = \alpha_{\max}/\alpha_{\min}$.

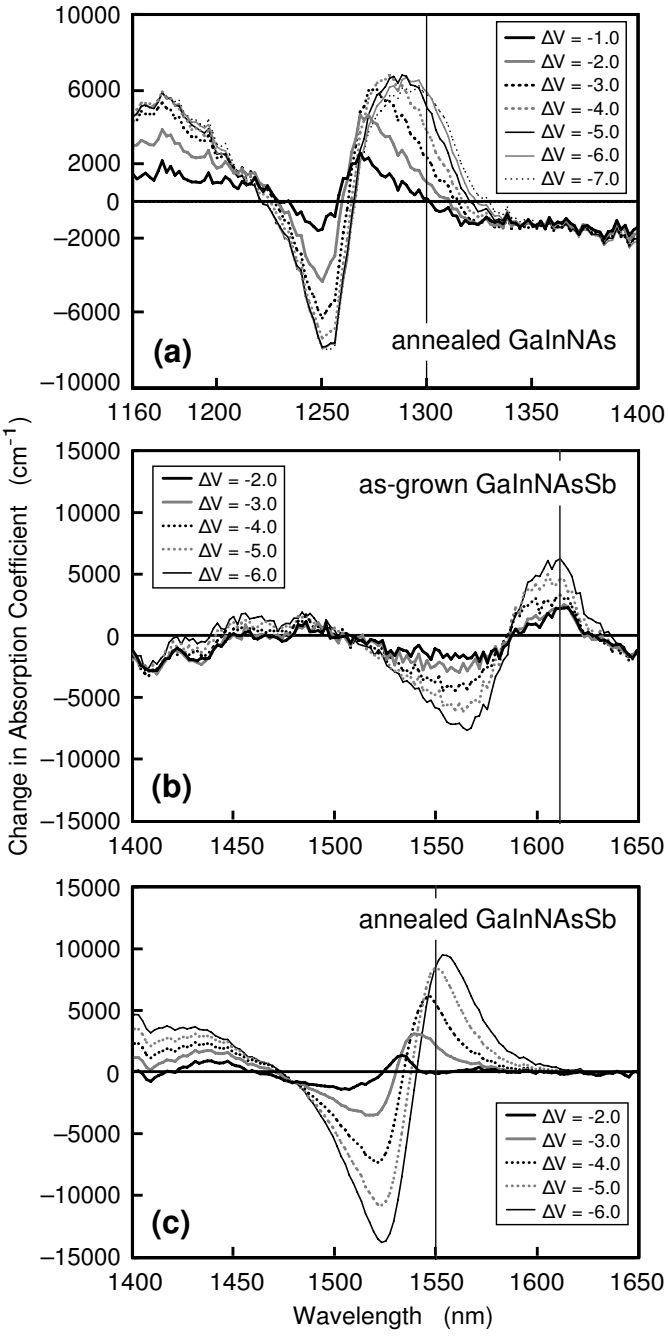


Figure 6.10: Electroabsorption characteristics of (a) GaInNAs/GaNAs QWs annealed at 720°C for 1 min, (b) GaInNAsSb/GaNAs QWs as-grown, and (c) GaInNAsSb/GaNAs QWs annealed at 800°C for 3 min, relative to the 0 V bias points.

The insertion loss ($IL$) of the device is then given by

$$IL = -10\log(R_{\text{on}}). \tag{6.3}$$

Plugging in the values above, we calculate expected insertion losses of 3.5 dB, 1 dB, and 7 dB, for the three devices, respectively. The 7 dB insertion loss for the annealed GaInNAsSb device at 1550 nm is somewhat high, due to the high required front mirror reflectivity and operation at a fairly low $X$, but still is reasonable. The calculated insertion losses for the other two devices are acceptably low by current standards.

The required $R_f$ for these GaInNAs(Sb) QWs, particularly the GaInNAsSb case at 1550 nm, is fairly high due to the short interaction length imposed by the ability to grow only a few highly strained QWs. The large $R_f$ creates a relatively high finesse cavity that compensates for the short interaction length by increasing the photon lifetime in the cavity. However the device performance (aside from insertion loss) is not strongly affected (see below), because the material exhibits very high values of absorption coefficient. Device performance is largely determined by the product of absorption coefficient with interaction length, $\alpha \cdot L$, so the GaInNAs(Sb) material system wins with its large absorption coefficient, although the interaction length is small due to strain-limited growth. Compared to current InGaAs(P)-based devices grown on InP, which suffer from a much smaller absorption coefficient, but which can be fabricated with a longer interaction length, the expected performance of the GaInNAs(Sb)-based devices on GaAs is similar due to the similar overall product $\alpha \cdot L$. Interestingly, in further comparison of the GaInNAs case with the GaInNAsSb case, we find that the smaller number of QWs that can be grown for the long-wavelength material is closely compensated by a correspondingly higher absorption coefficient.

A formula for the modulation ratio ($MR$) of the device [161], defined as the ratio

$R_{\mathrm{on}}/R_{\mathrm{off}}$, is also derived in Ref. [153] and is given by

$$MR = \left[ \frac{r_{\mathrm{on}} - r_{\mathrm{on}} r_f \left( \frac{r_{\mathrm{on}} + r_f}{1 + r_{\mathrm{on}} r_f} \right)^X}{\left( \frac{r_{\mathrm{on}} + r_f}{1 + r_{\mathrm{on}} r_f} \right)^X - r_f} \right]^2 , \tag{6.4}$$

where as above the lowercase $r$'s denote electric field reflectivities. Equation (6.4) yields an expected maximum device performance of ∼15 dB modulation ratio for the annealed GaInNAs device at 1300 nm (5 V swing across 0.5 $\mu$m intrinsic region), and also ∼15 dB modulation ratio for the as-grown GaInNAsSb device at 1610 nm (6 V swing across 0.5 $\mu$m intrinsic region). The very large absorption change for the annealed GaInNAsSb sample yields expected device performance of over 20 dB modulation ratio at 1550 nm (6 V swing across 0.5 $\mu$m intrinsic region). These values of modulation ratio are high enough for possible use even in analog systems, in addition to digital applications which generally require much lower modulation ratios as low as 2–3.

Finally, we can estimate the expected optical bandwidth of the devices to assess their performance over a range of wavelengths, as well as the sensitivity to wavelength drift and the temperature sensitivity of the devices. A formula to estimate the optical bandwidth ($\Delta\lambda$) from the half-width at half maximum of the Fabry-Perot resonance at the matching condition, taking into account the wavelength-dependent phase change from the distributed Bragg reflector mirrors, is given in Ref. [153] as

$$\Delta\lambda = \frac{\lambda_0}{2\pi m} \left[ \cos^{-1} \left( \frac{2R_f}{1 + R_f^2} \right) \right] \cdot \left( \frac{n_{\mathrm{hi}} - n_{\mathrm{lo}}}{n_{\mathrm{hi}} - n_{\mathrm{lo}} + \frac{n_{\mathrm{lo}}}{n_{\mathrm{hi}}}} \right) , \tag{6.5}$$

where $\lambda_0$ is the free space wavelength of the Fabry-Perot resonance, $m$ is order of the cavity (actually, the number of half-wavelengths that fit in the cavity, neglecting field penetration into the mirrors), and $n_{\mathrm{hi}}$ and $n_{\mathrm{lo}}$ are the high and low refractive indices,

respectively, of the alternating quarter-wave layers in the mirror stacks. The last term in parentheses accounts for the phase change from the mirrors and effectively corrects for the fictitious value of $m$ used in the formula. Applying Eq. (6.5) to the cases above, assuming the use of AlAs/GaAs DBRs and a 0.25 $\mu$m intrinsic region thickness, predicts optical bandwidths exceeding 20 nm full-width at half-maximum for the annealed devices and $\sim$15 nm for the as-grown GaInNAsSb device. These values of optical bandwidth are quite favorable.

In light of the very promising device characteristics predicted from the absorption measurements, progress is being made in our group toward fabrication and demonstration of high performance modulators operating at 1550 nm based on GaInNAsSb on GaAs. Section 6.4.2 below details the design of a 1550 nm asymmetric Fabry-Perot reflection modulator based on the measured QCSE characteristics in Fig. 6.8(d).

### 6.4.2 Design of a 1550 nm Asymmetric Fabry-Perot Reflection Modulator

The results and calculations of expected device performance presented above are very encouraging and motivate a continued effort to optimize our GaInNAsSb QWs and fabricate a high-performance asymmetric Fabry-Perot reflection modulator. A modulation ratio of 20 dB, if realized, would be useful for either analog or digital application, comparable to current devices fabricated in InGaAsP on InP [164]. A main issue would be to reduce the operating voltage to 1.0–1.5 V, for compatibility with CMOS. Simple voltage-doubling circuits are available that could double this voltage requirement as well. One simple way to reduce the operating voltage is to decrease the cavity length in the Fabry-Perot modulator, since in our case only a few QWs can be grown (or are required) in the active region anyway. In the design that follows, a 0.25 $\mu$m intrinsic region is utilized instead of the 0.5 $\mu$m intrinsic region of

the test devices discussed above, to minimize the required voltage for operation.

Figure 6.11 illustrates the designed device cross-section. The active region consists of 3 GaInNAsSb/GaNAs QWs (80 Å/200 Å) tuned for 1540 nm PL emission after annealing (nominally 800°C for 3 min) in the center of the 0.25 $\mu$m GaAs intrinsic region. The $p$- and $n$-doped regions surrounding the QWs act as spacers to create the half-wavelength cavity between the DBRs. The doping levels are $5\times10^{17}$ cm$^{-3}$ with carbon and $1\times10^{18}$ cm$^{-3}$ with silicon for the $p$ and $n$ regions, respectively. Since the device is reverse biased and does not draw significant current, constant doping throughout the DBR regions is acceptable, as opposed to "delta-doping" schemes necessary for high-performance VCSELs. The mirrors are fabricated from $Al_{0.87}Ga_{0.13}As$/GaAs layers to prevent device degradation from oxidation of high Al-content layers. The front mirror consists of 12.5 AlGaAs/GaAs pairs for $R_f = 0.76$, while the back mirror consists of 26.5 pairs for $R_b = 0.99$. AlGaAs layers are used for the first and last layers of both DBRs, as indicated, to place the maximum of the optical field at the location of the QWs in the center of the cavity. The thicknesses of all the layers are indicated on the figure. A conservative simulation of the expected device performance is shown in Fig. 6.12, where the absorption data for fully annealed 1550 nm GaInNAsSb QWs from Fig. 6.8(d) was used for the cavity loss characteristic. The "on" and "off" states correspond to the 2.0 V and 6.0 V data, respectively, giving a conservative estimate of the device performance. With a 0.25 $\mu$m intrinsic region, this would correspond to a 2 V swing (1–3 V) for the device operation. A contrast ratio of at least 2.5 is predicted, with an optical bandwidth of more than 5 nm (full-width at 90% of peak contrast ratio).

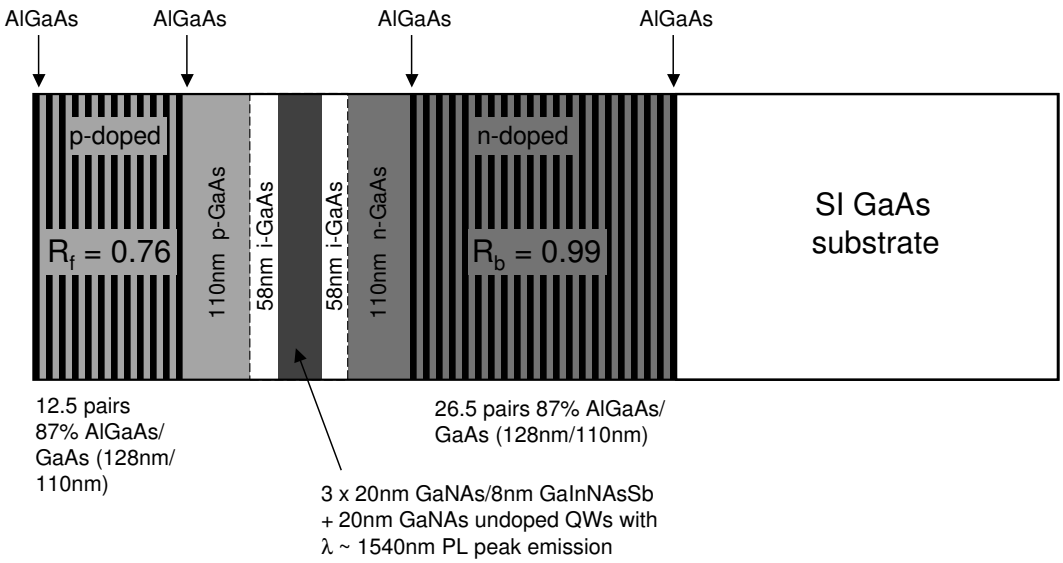


Figure 6.11: Epitaxial growth structure for designed 1550 nm asymmetric Fabry-Perot reflection modulator using GaInNAsSb/GaNAs QW active region.

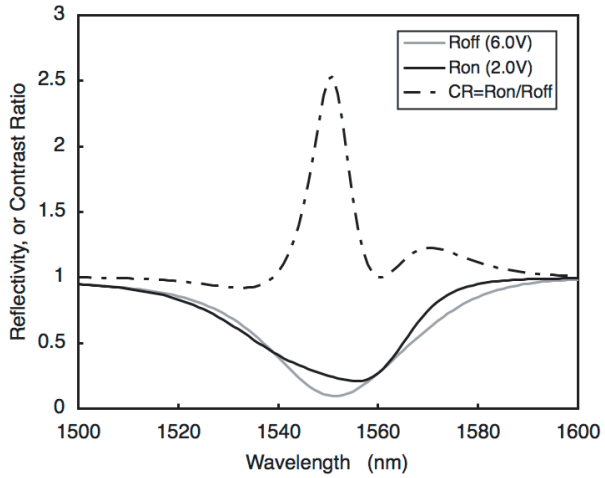


Figure 6.12: Conservative calculation of possible expected device performance for the structure shown in Fig. 6.11.

# Chapter 7

# Conclusions

The GaInNAs(Sb) material system offers great promise for use in optoelectronic devices operating in the 1300–1600 nm wavelength range. Lasers, detectors, and modulators operating in this range are important for telecommunications and optical interconnects. In the telecommunications arena, the use of GaInNAs(Sb) has the potential to offer a low-cost, high-volume solution to address current bottlenecks in the "last mile" of optical networks. For optical interconnects, the small band gap implies a low operating voltage. The cost advantage arises from the use of GaAs substrates and the availability of compatible DBR technology for the fabrication of inexpensive vertical-cavity devices. The possibility of fabricating vertical cavity devices presents further advantages for system architecture, such as allowing 2D arrays to be created. Inherent material advantages may also be significant, such as high differential gain and low temperature sensitivity. In addition, the existence of advanced integrated circuit technology on GaAs enables the on-chip integration of high-speed electronics with optical devices.

For this dissertation, a combined theoretical and experimental study was performed to understand the fundamental material properties of this unique semiconductor system in light of its band-edge optical transitions useful for optoelectronic

devices. A relationship between local atomic structure and variations of these properties was examined. In addition, the specific application of GaInNAs(Sb) quantum wells for optical modulators covering the 1300–1600 nm wavelength range was assessed.

*Ab initio* band structure calculations elucidated the nature of the sharp band gap lowering observed in dilute-nitride arsenide semiconductors with the addition of small amounts of N and further revealed some interesting properties of the band-edge optical transitions. A combined model was developed that links a phenomenological band-anticrossing model at very dilute N concentrations (∼0.1% N or less) with the formation of a "N-band" below the host Ga(In)As conduction band at higher N concentrations. The N-band originates from strong N–N (second and higher nearest neighbor) pair interactions that exist even in the dilute limit. The band-edge optical transitions in this material are dominated by the N-related states (particularly the N-band when the crystal includes appreciable N content), defining semi-localized transitions in space. However, except in very dilute limit, there is significant long-range interaction among N sites that leads to effectively homogenous properties for high-quality crystalline material. The local origin of the band-edge optical properties causes those properties to be quite sensitive to modification of the N-related states.

The properties of the N sites are dominated by the nearest neighbor atomic configuration, which can take one of five combinations of Ga and/or In bonding in its tetrahedral arrangement. The different possible local atomic configurations lead to a five-fold fine-splitting of the bands (and the band gap) on the order of 20–40 meV between states. The configurations with higher degrees of N–In bonding are thermodynamically favorable, although a random arrangement of atoms favors N–Ga bonding, for material compositions of technological interest. We found using x-ray absorption measurements that MBE-grown material has a nearly random atomic arrangement at the nearest neighbor level, preferring N–Ga bonding during the low-temperature

kinetic growth process. After thermal annealing, the local arrangement shifts to a thermodynamically-preferred structure dominated by N–In bonding. States with 0 and 1 In atom bonded to N are particularly unfavorable and deplete quickly upon annealing, leading to a final equilibrium structure containing some distribution of states having 2, 3, and 4 In atoms bonded to N. Analysis of the x-ray absorption data involved high accuracy *ab initio* calculations of partial local density of states, and was performed for both relaxed thick-film and biaxially compressively strained thin-film samples. The presence of strain in the films was found to modify somewhat the measured x-ray spectra, but did not significantly affect the N nearest neighbor distribution in the as-grown or annealed material.

With photoluminescence and electroreflectance spectroscopy, we were able to quantitatively measure the distribution of N–In nearest neighbor bonds in samples of as-grown and variously-annealed GaInNAs(Sb) QWs, demonstrating the nearest neighbor rearrangements upon annealing. The atomic reconfiguration was directly related to a large blueshift of the band gap that occurs during annealing and which was predicted from the band structure calculations. We further found that the reconfiguration of N–In nearest neighbor bonds during annealing leads to an improved optical transition matrix element, also consistent with our theoretical predictions. The enhanced matrix element after annealing leads to an increased absorption coefficient of the material of $\sim 2\times$, and also contributes to an increase in optical emission intensity, although most of the gain in spontaneous emission (photoluminescence) after annealing can be attributed to the removal of nonradiative defects incurred during the low-temperature growth. Furthermore, a Gaussian exciton lineshape was observed with photoluminescence and electroreflectance, as well as electroluminescence and photocurrent, even at temperatures as low as $\sim 15$ K. The Gaussian lineshape indicated strong exciton-phonon coupling in the material caused by the heavy electron effective mass (exciton effective mass), large exciton radius, and intrinsic lattice

defects in the material.

An important technological implication of the above results is that a protocol is developed for targeting a specific operating wavelength of devices, such as lasers and modulators, using GaInNAs(Sb) in the active region. In the past, targeting a specific wavelength by controlling the material composition had been difficult, due to poorly-controlled large shifts of the band gap of up to 100 nm or more during processing (i.e., thermal annealing). The wavelength shift is especially problematic for fabrication of vertical-cavity lasers, which require nm-level wavelength precision to match the resonant wavelength of the high-finesse cavity. The results of this dissertation indicate that performing a sufficiently long post-growth anneal will saturate the band gap shift when the equilibrium atomic configuration is attained. Thus, a relatively constant shift in wavelength can reliably be anticipated by design.

Finally, measurements of the absorption spectra of GaInNAs/GaNAs and GaInNAsSb/GaNAs QWs embedded in GaAs *p-i-n* diodes were performed using photocurrent, to assess the potential performance of optical modulators operating in the 1300–1600 nm wavelength range using GaInNAs(Sb) active regions. Very high peak band-edge absorption coefficients were measured ∼18,000 $cm^{-1}$ for GaInNAs/GaNas at 1250 nm and 35,000 $cm^{-1}$ for GaInNAsSb/GaNAs at 1525 nm. The value for GaInNAsSb is a record for any material in that wavelength range. By measuring absorption spectra with various applied reverse bias voltages across the diodes, excellent demonstration of the quantum confined Stark effect for GaInNAs(Sb) QWs at room temperature was accomplished. Sharp exciton resonances (FWHM ∼25 meV in the low-field limit) were observed in the spectra that persisted to relatively high electric fields over 70 kV/cm. These data represent the first measurements of the quantum confined Stark effect at such long wavelengths in this material system. The Gaussian exciton lineshape of these materials contributed beneficially to these results, giving the absorption edge a sharp tail. Estimated device performance for modulators using

an asymmetric Fabry-Perot reflection configuration and GaInNAs(Sb) QWs in the active region, obtained from the absorption measurement results, includes a 15–20 dB modulation ratio with optical bandwidths around 20 nm, comparable to existing state of the art devices using InGaAs(P) active layers on InP. We expect that high-speed, low-cost modulators can be fabricated using GaInNAsSb to address current bottlenecks in telecommunications and enable low-voltage optical interconnect technology. A design for a device operating at 1550 nm was presented.

# Chapter 8

# Future Work

Future effort is warranted in the growth, fabrication, and testing of a proof-of-principle optical modulator, as designed in Section 6.4.2. Growth calibrations are required to ensure a wavelength match between the resonant cavity and the GaInNAsSb active layer, although the tolerance is relatively loose compared to a VCSEL growth. An *in situ* check of the growth rates via the DBR reflectivity spectrum before the active layer growth would be sufficient. Device fabrication could mimic that described in Section 2.1.2 for simple test devices, or for high-speed devices a slight modification of the geometry would be required to optimize the device size (RC delay) and form high-speed, impedance-matching transmission line leads. In addition, current trends in optical interconnect technology and optical computing would warrant an effort to integrate GaInNAs(Sb) modulators on Si substrates, either with flip-chip bonding or with monolithic growth using SiGe buffer layers or compliant substrate layers.

Obtaining maximum performance from the optical modulator would benefit from further improvements in quantum well growth and optimization of the quantum wells for modulator application. Recent growth "tricks," such as the use of ion deflection plates at the N cell aperture, which were not employed for the samples in this study, may introduce an immediate improvement in the already very promising absorption characteristics. Additionally, standard techniques are described in the literature for

optimizing the quantum confined Stark effect for optical modulation, such as the use of coupled double quantum wells with differing thicknesses or engineering the strain in the wells [162, 163]. In fact, very little work has been done in our group to study GaInNAs(Sb) quantum wells with different thicknesses. A combinatorial study of alloy compositions and well thicknesses that achieve the appropriate operating wavelength with optimum absorption coefficient, sharpness of absorption onset, and interaction length would be useful. Comparison of the performance using different barrier compositions should also be undertaken.

In addition, to increase the interaction length of the GaInNAsSb QWs, a metamorphic growth on a graded buffer layer may be attempted. One might explore the use of AlInGaAs or AlInGaP buffer materials to ensure transparency at the operating wavelength. The buffer would be engineered to slowly grade the substrate lattice constant to an appropriate average value between those of the QW and barrier materials. If enough QWs can be grown in this way, DBRs may not be needed for the modulator, and an asymmetric cavity may be formed by depositing Au on the back side as a high reflector and using the air-semiconductor interface as the low-reflectivity front mirror.

In addition to the modulator application, GaInNAs(Sb) quantum wells may also find use as saturable absorbers in future monolithic mode-locked VCSELs [165]. Measurement of the saturation intensity and carrier escape times would allow direct assessment of the performance for this application [166, 167]. The saturation intensity and carrier escape times may also limit the maximum clock rate of free-space optical systems [168–171] that could utilize modulators with GaInNAs(Sb) active regions [167], so measurement of these parameters would have wider utility. The existing samples fabricated for this dissertation can be used directly for these measurements.

Furthermore, some follow-up materials studies are worthwhile to perform. Additional theoretical study of the band structure, especially of clustering effects, and

quantitative verification of the extracted values may be performed using more accurate methods, such as LDA+U or the GW method. Experimental validation of the calculations using angle-resolved photoemission spectroscopy [172] would be interesting, especially to positively identify the N-band. Also, detailed investigations of the N and In self-diffusion kinetics in GaInNAs(Sb) utilizing tracers and variations of As overpressure during growth to modify the As vacancy concentration would allow precise determination of the mechanism of nearest neighbor rearrangement during annealing. There have been conjectures that N may be very immobile in the crystal after growth and that most of the rearrangement is due to In diffusion via Group III vacancies, as presented in this dissertation. The degree of N diffusion may be affected, however, by the concentration of Group V vacancies. Finally, additional comparison between MBE-grown and OMVPE-grown GaInNAs material is warranted to elucidate the intricacies of the growth mechanism of these complex semiconductor alloys. The techniques described in this dissertation would be useful for some of this comparison.

# Appendix A

# VASP Files

This appendix lists some of the key VASP (Vienna *Ab Initio* Simulation Package) files used for the different types of *ab initio* simulation runs described in Chapter 3.

## A.1 INCAR Files

This section lists the INCAR files used to initiate the various types of runs. A detailed explanation of running VASP and the various switches shown below can be found in the VASP Guide [88].

### A.1.1 Atomic Relaxation and Total Energy INCAR File

```
ISTART=0
INIWAV=1
ICHARG=2

IALGO=48
ISMEAR=-5

NSW=25
ISIF=2
IBRION=1
POTIM=0.5
```

```
EDIFF=1.0E-5
EDIFFG=-0.01
LREAL=.FALSE.

NBANDS=268

NSIM=4
# NSIM=8      # used with many processors
NPAR=8

LWAVE=.FALSE.
LCHARG=.TRUE.
LELF=.TRUE.
```

### A.1.2 Self Consistent Charge Density and Partial Local Density of States INCAR File

```
ISTART=0
INIWAV=1
ICHARG=2

IALGO=48
ISMEAR= -5
WEIMIN=0

RWIGS=1.773 1.675 2.027 1.055   # adjusted for each model

IBRION=-1
NSW=0

NSIM=8
NPAR=1

NBANDS=300

EDIFF=1.0E-4

LWAVE=.FALSE.
LCHARG=.TRUE.
```

### A.1.3 Band Structure INCAR File

```
ISTART=0
INIWAV=1
ICHARG=11

ISMEAR=0
SIGMA=0.1
IALGO=48

IBRION=-1
NSW=0

NSIM=8
NPAR=4

NBANDS=300

NELM=40
NELMIN=6
NELMDL=0
EDIFF=1E-4
LREAL=.FALSE.

LWAVE=.FALSE.
```

### A.1.4 Fat Band Structure INCAR File

```
ISTART=0
INIWAV=1
ICHARG=11

ISMEAR=0
SIGMA=0.1
IALGO=48

IBRION=-1
NSW=0

RWIGS=1.773 1.675 2.027 1.055   # adjusted for each model
```

```
NSIM=8
NPAR=1

NBANDS=300

NELM=40
NELMIN=6
NELMDL=0
EDIFF=1E-4
LREAL=.FALSE.

LCHARG=.FALSE.
LWAVE=.FALSE.
```

### A.1.5 Band Offset (Local Potentials) INCAR File

```
ISTART=0
INIWAV=1
ICHARG=1

IALGO=48
ISMEAR=-5
WEIMIN=0

IBRION=-1
NSW=0

NSIM=8
NPAR=4

NBANDS=300

EDIFF=1.0E-4
LVTOT=.TRUE.

PREC=High

LWAVE=.FALSE.
LCHARG=.FALSE.
```

## A.2 Other Input Files

### A.2.1 Band Structure KPOINTS File

The following gives an example KPOINTS file, listing the typical 51 $k$-points used in band structure and fat band structure calculations. High symmetry points are indicated in the comments. The commented column labeled "x-axis" lists the corresponding "length" values for plotting the band structure in the traditional 1D fashion.

```
#kx       ky       kz              # x-axis
 0        0        0.5      # X    # -1
 0        0        0.4             # -0.8
 0        0        0.37            # -0.74
 0        0        0.33            # -0.66
 0        0        0.3             # -0.6
 0        0        0.27            # -0.54
 0        0        0.23            # -0.46
 0        0        0.2             # -0.4
 0        0        0.17            # -0.34
 0        0        0.13            # -0.26
 0        0        0.1             # -0.2
 0        0        0.07            # -0.14
 0        0        0.03            # -0.06
 0        0        0        # G    #  0
-0.015   -0.015   -0.015           #  0.051961524
-0.035   -0.035   -0.035           #  0.121243557
-0.05    -0.05    -0.05            #  0.173205081
-0.065   -0.065   -0.065           #  0.225166605
-0.085   -0.085   -0.085           #  0.294448637
-0.1     -0.1     -0.1             #  0.346410162
-0.115   -0.115   -0.115           #  0.398371686
-0.135   -0.135   -0.135           #  0.467653718
-0.15    -0.15    -0.15            #  0.519615242
-0.165   -0.165   -0.165           #  0.571576766
-0.185   -0.185   -0.185           #  0.640858799
-0.2     -0.2     -0.2             #  0.692820323
-0.25    -0.25    -0.25            #  0.866025404
-0.3     -0.3     -0.3             #  1.039230485
```

```
-0.35    -0.35    -0.35           #  1.212435565
-0.4     -0.4     -0.4            #  1.385640646
-0.45    -0.45    -0.45           #  1.558845727
-0.5     -0.5     -0.5     # L     #  1.732050808
 0.5      0.5      0.45           #  1.832050808
 0.5      0.5      0.4            #  1.932050808
 0.5      0.5      0.35           #  2.032050808
 0.5      0.5      0.3            #  2.132050808
 0.5      0.5      0.25           #  2.232050808
 0.5      0.5      0.2            #  2.332050808
 0.5      0.5      0.15           #  2.432050808
 0.5      0.5      0.1            #  2.532050808
 0.5      0.5      0.05           #  2.632050808
 0.5      0.5      0        # K     #  2.732050808
 0.45     0.45     0              #  2.873472164
 0.4      0.4      0              #  3.01489352
 0.35     0.35     0              #  3.156314876
 0.3      0.3      0              #  3.297736233
 0.25     0.25     0              #  3.439157589
 0.2      0.2      0              #  3.580578945
 0.15     0.15     0              #  3.722000301
 0.1      0.1      0              #  3.863421657
 0.05     0.05     0              #  4.004843014
 0        0        0        # G     #  4.14626437
```

### A.2.2 Lattice Constant Calculations

The following shell scripts illustrate how the runs were performed to determine the equilibrium lattice constant for each model. These scripts are specific for Longhorn at the Texas Advanced Computing Center. The general procedure involves initializing the run directory with the appropriate INCAR, KPOINTS, POSCAR, and POTCAR files for the current model. Then "`setup_dirs`" is edited to include the atomic positions from POSCAR and to choose the set of lattice constants for which to calculate total energies. Running the edited "`setup_dirs`" script then creates a series of run directories and submits the jobs to Longhorn's batch queue. (The "`setup_dirs`"

script includes an example of a run script for VASP on Longhorn.) Finally, when all the runs have completed, running "`extract_E`" generates a final output file named "`energies.out`" that contains a table of lattice constant values (`a0`) and corresponding total energies (`E`). A quadratic fit to the "`energies.out`" values gives the equilibrium lattice constant.

A similar procedure was used to determine the equilibrium out-of-plane lattice constant for strained calculations. The essential difference is that the length of lattice vectors in the $x$ and $y$ directions were set to the value for GaAs, while only the out-of-plane vector was varied from run to run.

**setup_dirs**

```
#!/usr/bin/sh

count=1
for a in 11.022062 11.00 10.95 11.10 11.20
do

cat >loadlev${count} <<!
#@ shell= /bin/csh
#@ initialdir = `pwd`/run${count}
#@ job_name = /paci/stanford/ux453298/vasp
#@ input = /dev/null
#@ output = `echo 'LL_out.$(jobid)'`
#@ error = `echo 'LL_err.$(jobid)'`
#@ job_type = parallel
#@ environment = COPY_ALL; MP_SHARED_MEMORY=yes
#@ resources = ConsumableCpus(1) ConsumableMemory(1024mb)
#@ node = 1
#@ tasks_per_node = 8
#@ class = normal
#@ wall_clock_limit = 0:10:00
#@ notify_user = vlordi@stanford.edu
#@ notification=error
#@ notification=complete
#@ queue
```

```
poe /paci/stanford/ux453298/vasp
!

cat >POSCAR${count} <<!
GaNAs_30unstr
 $a
     1.0000000000000000    0.0000000000000000    0.0000000000000000
     0.0000000000000000    1.0000000000000000    0.0000000000000000
     0.0000000000000000    0.0000000000000000    1.0000000000000000
    22  10  31   1    Ga  In  As  N
Direct
  0.0059997404574617  0.9970683696656693  0.9930861199740946
  0.0050910986309418  0.2470945645385143  0.2431123131231274
... (the remainder of the atomic positions) ...
  0.6309629356104125  0.3721051508329367  0.3681229211013317
!

mkdir run$count
cp INCAR run${count}/.
mv POSCAR${count} run${count}/POSCAR
cp POTCAR run${count}/.
cp KPOINTS run${count}/.
mv loadlev${count} run${count}/loadlev

echo Run $count: a0=$a Angs
echo $a > run${count}/a0

llsubmit run${count}/loadlev
echo

count=‘expr $count + 1‘
done
```

**extract_E**

```
#!/usr/bin/sh

echo "\c" > energies.out  # create a new file named energies.out
```

```
count=1
while [ -e run${count}/OSZICAR ]; do

E=‘grep E0 run${count}/OSZICAR‘
a=‘more run${count}/a0‘
echo $a $E >>energies.out
count=‘expr $count + 1‘
done

awk ’{ print $1, $6 }’ energies.out > energies.out_temp
mv energies.out_temp energies.out<
```

# Appendix B

# Strained Varshni Relation

The analysis of localization energy in Section 5.2 depends on the assumption that the peak in the PL spectrum corresponds to the band gap and that changes in the band gap directly correlate to changes in the peak energy. Here we will show through a basic analysis using an effective mass approximation including the effects of strain and quantum confinement that this assumption is valid. For illustration, we will consider $In_xGa_{1-x}As/GaAs$ QWs since the material parameters are well known [131] and a very large degree of strain can be imposed (mathematically).

We will begin with the assumption that the bulk band gap of the well and barrier material follow the Varshni form [126]

$$E_g(T) = E_g(0) - \frac{\alpha T^2}{T + \beta}, \tag{B.1}$$

and assume a 30% band offset in the valence band irrespective of temperature or composition. Then, for a given $In_xGa_{1-x}As$ composition and temperature $T$, we can construct the unmodified "bulk" potential profile of the QW (solid lines in Fig. B.1). The strain is then calculated from the lattice constants and elastic constants, using a linear interpolation of the parameters for InGaAs, and including the temperature variation through

$$a_0^i = A_a^i + B_a^i(T - 300\ K), \tag{B.2}$$

where $A_a$ and $B_a$ are constants and $i$ indexes the different materials. For convenience, the strain in the film can be divided into a volume term and an axial term given by [173]

$$\epsilon_{\text{vol}} = \left(\frac{a_w - a_b}{a_w}\right)\left[2\left(\frac{C_{12}}{C_{11}-1}\right)\right] \tag{B.3}$$

and

$$\epsilon_{\text{ax}} = \left(\frac{a_w - a_b}{a_w}\right)\left(\frac{2C_{12}}{C_{11}}+1\right), \tag{B.4}$$

where $a_w$ and $a_b$ are the lattice constants of the well and barrier, respectively, and $C_{11}$ and $C_{12}$ are the elastic constants. Then we can determine the strained band edges in the well by calculated the following corrections to the bulk band edges [173]:

$$\delta E_c = a_c(\epsilon_{xx} + \epsilon_{yy} + \epsilon_{zz}) = a_c\epsilon_{\text{vol}}, \tag{B.5a}$$

$$\delta E_{hh} = a_v(\epsilon_{xx} + \epsilon_{yy} + \epsilon_{zz}) - b_v\epsilon_{\text{ax}} = a_v\epsilon_{\text{vol}} - b_v\epsilon_{\text{ax}}, \tag{B.5b}$$

$$\text{and } \delta E_{lh} = a_v(\epsilon_{xx} + \epsilon_{yy} + \epsilon_{zz}) + b_v\epsilon_{\text{ax}} = a_v\epsilon_{\text{vol}} + b_v\epsilon_{\text{ax}}, \tag{B.5c}$$

where $a_c$ and $a_v$ are the hydrostatic deformation potentials in the conduction band and valence band, respectively, and $b_v$ is the shear deformation potential for strain in the [001] crystal direction that splits the HH and LH bands. Equations B.5 allow us to construct the strained QW band structure, as shown in Fig. B.1, which illustrates the meanings of the $\delta E_i$.

From the construction in Fig. B.1, we can essentially treat the QW potential as three separate particle-in-a-finite-box problems, one each for the electron, HH, and LH which have slightly different well depths. The quantized energy levels (we only require the first level in each band) can be found for these potentials by solving the transcendental equation

$$\sqrt{E}\tan\left[\frac{\pi}{2}\sqrt{\frac{E}{E^\infty}}\right] = \sqrt{\frac{m_w}{m_b}(\Delta E - E)}, \tag{B.6}$$

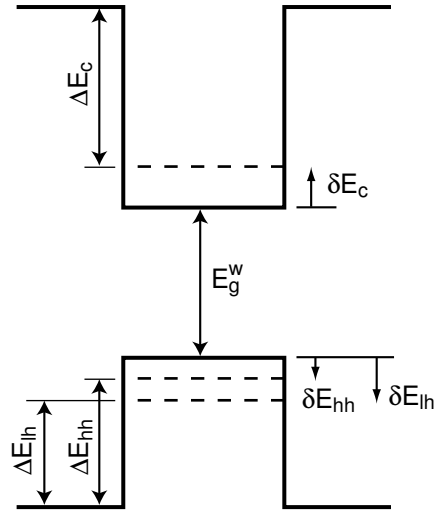


Figure B.1: The band edges in a strained quantum well can be calculated from corrections to the bulk band lineup, as illustrated.

where

$$E^{\infty} = \frac{\hbar^2 \pi^2}{2 m_w w}, \tag{B.7}$$

and $m_w$ and $m_b$ are the effective masses in the well and barrier, respectively, $\Delta E$ is the height of the potential well, and $w$ is the well width. Solving Eq. (B.6) for $E$ gives the spectrum of energy levels for the electrons, HH, and LH; we will label the first level in the respective bands $E_c$, $E_{hh}$, and $E_{lh}$. Finally, we obtain the strained band gaps at each $T$ from

$$E^{\ddagger}_{g,hh} = E^{w}_{g} + \delta E_c + \delta E_{hh} + E_c + E_{hh} \tag{B.8a}$$

$$E^{\ddagger}_{g,lh} = E^{w}_{g} + \delta E_c + \delta E_{lh} + E_c + E_{lh}, \tag{B.8b}$$

where $E^{w}_{g}$, the strain, and the band offsets are all functions of $T$ as well as $x$ and $w$. Here $E^{w}_{g}$ is the bulk band gap of the well material.

To explore the validity of Eq. (B.1) for analysis of PL data from strained thin-film

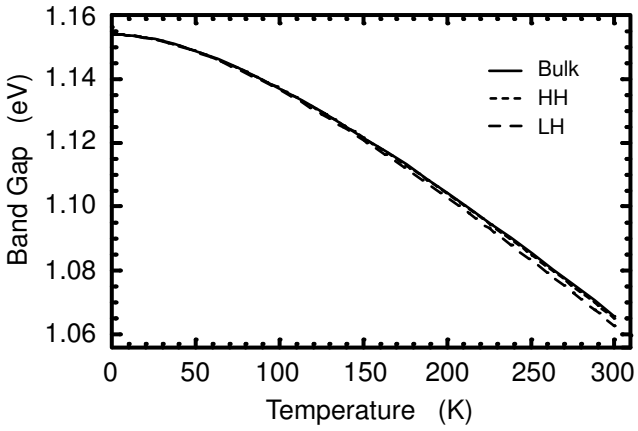


Figure B.2: The variation in band gap calculated using the simple Varshni equation for bulk material (solid line) and calculated including strain and quantum confinement for heavy holes (short dashed line) and light holes (long dashed line) in a 50 Å-thick $In_{0.25}Ga_{0.75}As/GaAs$ QW. The curves were shifted vertically to coincide at $T = 0$ to facilitate comparison of the curvatures.

samples, we can compare the temperature variation of $E_g^w$ with the true variation of the band gap from the smaller of Eqns. B.8. The results of this calculation for a 50 Å-thick, 25% In InGaAs/GaAs QW are shown in Fig. B.2. This case represents an extreme limit of large strain and high quantum confinement. The parameters used, as well as the interpolation procedure for InGaAs, were taken from Ref. [131]. The result shows very little difference in the change in band gap for the full calculation presented here and the simple application of Eq. (B.1). Quantum confinement gives approximately a constant shift of $E_g$ for all $T$. Thus, the band gap tracks the Varshni equation quite well even with large amounts of strain and quantum confinement in the well, and examining the variation of band gap measured from peak PL energy for strained thin-films using the Varshni equation is valid.

# Appendix C

# Calculating the Electric Field in a PnN Diode

For the quantum confined Stark effect measurements, it is desirable to know the value of electric field across the quantum wells for a given applied bias voltage, since electric field is the physical modulating parameter, while voltage is a more convenient external parameter. Since the quantum wells are in the center of a *p*-*i*-*n* diode, the built-in voltage of the diode must be taken into account in addition to any applied voltage. Furthermore, the molecular beam epitaxy growth technique tends to yield slightly *n*-type GaAs (on the order of $1\times10^{15}$ cm$^{-3}$) when nominally undoped material is desired. Then, calculation of the electric field profile in a biased PnN diode is required. This calculation is outlined below, assuming the depletion approximation. An example is provided that also shows that the electric field is homogeneous over the quantum wells, which comprise a relatively thin portion of the center of a wide "intrinsic" region in the devices fabricated for the work in this dissertation. Additionally, we find that the electric field across the quantum wells is insensitive to the background doping in the nominally intrinsic region, up to at least $1\times10^{17}$ cm$^{-3}$ doping. Also, the relatively low doping used in the *p*-layer of the test devices described throughout this dissertation results in a significant depletion width (and consequently band bending) in that layer, leading to "diminishing returns" in applied electric field as the voltage

is increased. Thus, for higher reverse bias voltages, the electric field across the wells is significantly lower than predicted by the simple calculation of voltage divided by intrinsic region thickness due to the band bending in the $p$-region.

We begin by assuming a one-dimensional PnN structure, with semi-infinite P and N layers and a nominally intrinsic region (the n layer) $I_{\text{width}}$ thick. The semi-infinite nature of the P and N layers can be verified after performing a calculation to be thicker than their corresponding depletion layer thicknesses. We also assume a fully-depleted n layer, which also can be checked, but is almost always the case. The doping concentrations in the P, n, and N layers are $P$, $I$, and $N$, respectively.

First, the quasi Fermi levels in the P and N regions are calculated by solving

$$P, N = \frac{1}{2\pi^2}\left(\frac{2m^* k_B T}{\hbar^2}\right)^{3/2}\int_0^\infty \frac{\sqrt{y}}{1+\exp(y - E_{\text{Fermi}}/k_B T)}dy, \tag{C.1}$$

where $m^*$ is the appropriate effective mass, $k_B$ is Boltzmann's constant, $T$ is the absolute temperature, and $E_{\text{Fermi}}$ is the quasi Fermi level relative to the appropriate band edge, with negative values being inside the band gap. Then, the built-in voltage is given by

$$V_{bi} = E_g + E_{\text{Fermi,N}} + E_{\text{Fermi,P}}. \tag{C.2}$$

The depletion widths in the P and N regions are found from

$$x_p = \frac{I_{\text{width}}(I-N) + \sqrt{\frac{N}{qP}\left(2K\epsilon_0(N+P)(V_{bi}+V_{\text{ext}}) + (N-I)(P+I)qI_{\text{width}}^2\right)}}{N+P} \tag{C.3}$$

and

$$x_n = \frac{x_p P - I_{\text{width}} I}{N}, \tag{C.4}$$

where $x_p$ and $x_n$ are the P and N region depletion widths, respectively, $K$ is the dielectric constant, $\epsilon_0$ is the permittivity of free space, $q$ is the electron charge, and $V_{\text{ext}}$ is the externally applied voltage to the diode. Poisson's equation can then be

solved for the electric field in each region:

$$E_p(x) = \frac{qP}{K\epsilon_0}(x_p + x), \qquad x < 0 \tag{C.5a}$$

$$E_i(x) = E_p|_{x=0} - \frac{qI}{K\epsilon_0}x, \qquad 0 < x < I_{\text{width}} \tag{C.5b}$$

$$E_n(x) = \frac{-qN}{K\epsilon_0}(x - x_n - I_{\text{width}}), \qquad x > I_{\text{width}} \tag{C.5c}$$

Finally, the potential in each region is found from:

$$V_p(x) = \frac{q}{2K\epsilon_0}P(x_p + x)^2, \qquad x < 0 \tag{C.6a}$$

$$V_i(x) = V_p|_{x=0} + \frac{q}{2K\epsilon_0}\left(-Ix^2 + 2Px_p x\right), \qquad 0 < x < I_{\text{width}} \tag{C.6b}$$

$$V_n(x) = V_i|_{x=I_{\text{width}}} + \frac{q}{2K\epsilon_0}N\left[x_n^2 - (x - x_n - I_{\text{width}})^2\right], \quad x > I_{\text{width}}. \tag{C.6c}$$

We can apply the equation above to the test devices discussed in this dissertation, which consisted of a 1.0 $\mu$m thick $1\times10^{18}$ cm$^{-3}$-doped N region, a 0.5 $\mu$m thick nominally intrinsic region ($1\times10^{15}$ cm$^{-3}$ $n$-type), and a 1.38 $\mu$m thick $5\times10^{17}$ cm$^{-3}$ P region. We find at 0 V external bias, a $p$-side depletion width of 0.28 $\mu$m, an $n$-side depletion width of 0.14 $\mu$m, a built-in voltage of 1.39 V, and an electric field across the center of the intrinsic region of 19.5 kV/cm (at 300 K). The corresponding band diagram is shown in Fig. C.1(a), where the homogeneous electric field across the center of the intrinsic region (0–0.5 $\mu$m) is apparent. Also shown in Fig. C.1(b) is the band diagram with 7 V applied reverse bias. In this case, significant band bending, especially in the P region, is observed, however the electric field through most of the intrinsic region is still quite uniform. Repeating the calculations with $1\times10^{17}$ cm$^{-3}$ unintentional $n$-type doping in the nominally intrinsic region reveals little effect, and the electric field across the QWs is still homogeneous even with such high background doping. Finally, Table C.1 lists the calculated values of electric field across the center of the nominally intrinsic region for various applied reverse bias voltages, and we

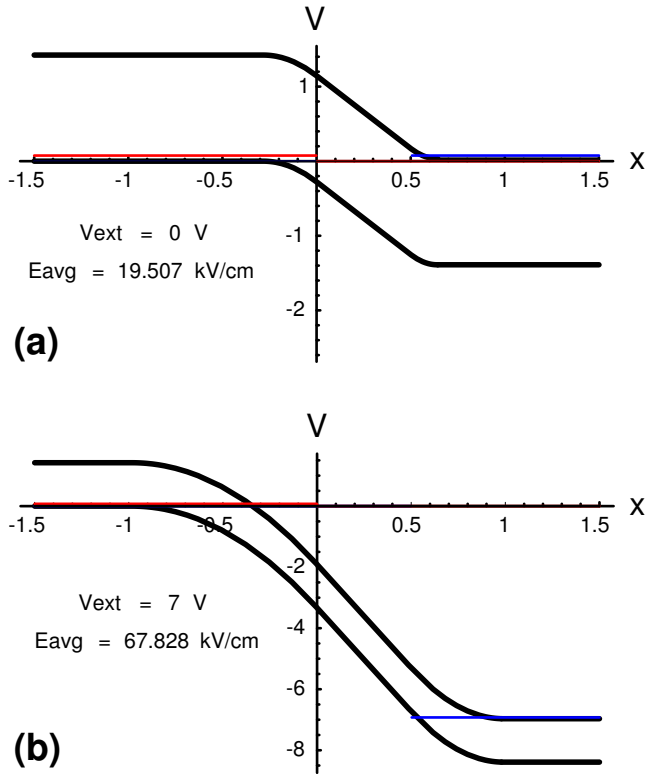


Figure C.1: (Color) GaAs *P-n-N* diode band diagrams with (a) 0 V and (b) 7 V applied external reverse bias. Quasi Fermi levels are shown as horizontal lines (blue in *n*-type region, red in *p*-type region).

notice the "diminishing returns" in applied electric field for high reverse bias voltages due to the excessive band bending in the relatively lightly doped P region.

Table C.1: Electric field in the center of the PnN diode for various applied reverse bias voltages.

| Applied Reverse Bias (V) | Electric Field (kV/cm) |
|---|---|
| 0.0 | 19.5 |
| 1.0 | 29.2 |
| 2.0 | 37.4 |
| 3.0 | 44.6 |
| 4.0 | 51.1 |
| 5.0 | 57.1 |
| 6.0 | 62.6 |
| 7.0 | 67.8 |
| 8.0 | 72.8 |
| 9.0 | 77.5 |
| 10.0 | 81.9 |

# References


[1] A. M. Odlyzko, in *Optical Transmission Systems and Equipment for WDM Networking II*, edited by B. B. Dingel, W. Weiershausen, A. K. Dutta, and K.-I. Sato (Proc. SPIE, 2003), vol. 5247, p. 1.

[2] J. S. Harris, Jr., *Semicond. Sci. Technol.* **17**, 880 (2002).

[3] J. S. Harris, Jr., *IEEE J. Sel. Topics Quantum Electron.* **6**, 1145 (2000).

[4] P. Kaiser, in *2001 Digest of LEOS Summer Topical Meetings: WDM Components* (Keystone, CO, 2001), p. 3.

[5] D. A. B. Miller, in *Semiconductor Quantum Optoelectronics: Proceedings of the Fiftieth Scottish Universities Summer School in Physics, St. Andrews, June 1998*, edited by A. Miller, M. Ebrahimzadeh, and D. M. Finlayson (Institute of Physics, Bristol, 1999), p. 433.

[6] J. W. Goodman, F. J. Leonberger, S.-Y. Kung, and R. A. Athale, *Proc. IEEE* **72**, 850 (1984).

[7] D. A. B. Miller, *Int. J. Optoelectron.* **11**, 155 (1997).

[8] D. A. B. Miller, *Opt. Lett.* **14**, 146 (1989).

[9] M. F. Feldman, S. C. Esener, C. C. Guest, and S. H. Lee, *Appl. Opt.* **27**, 1742 (1988).

[10] M. Kondow, K. Uomi, A. Niwa, T. Kitatani, S. Watahiki, and Y. Yazawa, *Jpn. J. Appl. Phys.* **35**, 1273 (1996).

[11] M. Kondow, K. Uomi, A. Niwa, T. Kitatani, S. Watahiki, and Y. Yazawa, *Jpn. J. Appl. Phys.* **35**, 1273 (1996).

[12] S. G. Spruytte, Ph.D. thesis, Stanford Univ. (2001).

[13] H. Riechert, A. Ramakrishnan, and G. Steinle, *Semicond. Sci. Technol.* **17**, 892 (2002).

[14] S. R. Bank, M. A. Wistey, L. L. Goddard, H. B. Yuen, V. Lordi, and J. S. Harris, *IEEE J. Quantum Electron.* **40**, 656 (2004).

[15] V. F. Gambin, Ph.D. thesis, Stanford Univ. (2003).

[16] J. S. Harris, Jr., in *Physics and Applications of Dilute Nitrides*, edited by I. Buyanova and W. Chen (Taylor & Francis, London, 2004).

[17] V. Gambin, W. Ha, M. Wistey, H. Yuen, S. R. Bank, S. M. Kim, and J. S. Harris, Jr., *J. Sel. Top. Quantum Electron.* **8**, 795 (2002).

[18] S. R. Bank, M. A. Wistey, L. L. Goddard, H. B. Yuen, V. Lordi, and J. S. Harris, *Electron. Lett.* **39**, 1445 (2003).

[19] S. R. Bank, H. B. Yuen, W. Ha, V. F. Gambin, M. A. Wistey, and J. S. Harris, in *Abstracts of the 45th Electronics Materials Conference* (Salt Lake City, UT, 2003), hH4.

[20] J. Massies and N. Grandjean, *Phys. Rev. B* **48**, 8502 (1993).

[21] E. Tournie, N. Grandjean, A. Trampert, J. Massies, and K. Ploog, *J. Cryst. Growth* **150**, 460 (1995).

[22] M. A. Wistey, S. R. Bank, H. B. Yuen, L. L. Goddard, and J. S. Harris, *Electron. Lett.* **39**, 1822 (2003).

[23] V. Lordi, H. Yuen, S. Bank, and J. S. Harris, *Appl. Phys. Lett.* **85**, 902 (2004).

[24] W. Ha, V. Gambin, S. Bank, M. Wistey, H. Yuen, V. Lordi, S. Kim, and J. S. Harris, Jr., *IEEE J. Quantum Electron.* **38**, 1260 (2002).

[25] P. Krispin, S. G. Spruytte, J. S. Harris, and K. H. Ploog, *J. Appl. Phys.* **88**, 4153 (2000).

[26] I. A. Buyanova, G. Pozina, P. N. Hai, W. M. Chen, H. P. Xin, and C. W. Tu, *Phys. Rev. B* **63**, 033303 (2000).

[27] R. Teissier, D. Sicault, J. C. Harmand, G. Ungaro, G. L. Roux, and L. Largeau, *J. Appl. Phys.* **89**, 5473 (2001).

[28] M. Hetterich, M. D. Dawson, A. Y. Egorov, D. Bernklau, and H. Riechert, *Appl. Phys. Lett.* **76**, 1030 (2000).

[29] R. Kudrawiec, H. B. Yuen, J. S. Harris, and J. Misciewicz (2004), to be published.

[30] J. S. Harris, Jr., M. Wistey, S. Bank, L. Goddard, V. Lordi, H. Bae, and H. Yuen, in *Dilute Nitride (III-V) Semiconductors: Physics and Technology*, edited by M. Henini (Elsevier, New York, 2005).

[31] S. G. Spruytte, C. W. Coldren, J. S. Harris, W. Wampler, P. Krispin, K. Ploog, and M. C. Larson, *J. Appl. Phys.* **89**, 4401 (2001).

[32] W. Ha, V. Gambin, S. Bank, M. Wistey, H. Yuen, V. Lordi, S. Kim, and J. S. Harris, Jr., *IEEE J. Quantum Electron.* **38**, 1260 (2002).

[33] S. G. Spruytte, M. C. Larson, W. Wampler, C. W. Coldren, H. E. Peterson, and J. S. Harris, *J. Cryst. Growth* **227–228**, 506 (2001).

[34] H. B. Yuen, S. R. Bank, M. A. Wistey, J. S. Harris, and A. Moto, *J. Appl. Phys.* **96**, 6375 (2004).

[35] M. A. Wistey, Ph.D. thesis, Stanford Univ. (2004).

[36] M. A. Wistey, S. R. Bank, H. B. Yuen, and J. S. Harris (2004), submitted to *J. Vac. Sci. Technol. B.*

[37] J. Stöhr, *NEXAFS Spectroscopy* (Springer-Verlag, New York, 1992).

[38] B. K. Teo, *EXAFS: basic principles and data analysis* (Springer-Verlag, New York, 1986).

[39] A. T. Young, V. Martynov, and H. A. Padmore, *J. Electron Spectrosc. Relat. Phen.* **101–113**, 885 (1999).

[40] A. T. Young, E. Arenholz, J. Feng, H. A. Padmore, S. Marks, R. Schlueter, E. Hoyer, N. Kelez, and C. Steier, *Surf. Rev. Lett.* **9**, 549 (2002).

[41] A. T. Young, J. Feng, E. Arenholz, H. A. Padmore, T. Henderson, S. Marks, E. Hoyer, R. Schlueter, J. B. Kortright, V. Martynov, et al., *Nucl. Instrum. Methods* **467–468**, 549 (2001).

[42] V. Lordi, V. Gambin, S. Friedrich, T. Funk, T. Takizawa, K. Uno, and J. S. Harris, *Phys. Rev. Lett.* **90**, 145505 (2003).

[43] S. Friedrich, T. Funk, O. Drury, S. E. Labov, and S. P. Cramer, *Rev. Sci. Instrum.* **73**, 1629 (2002).

[44] H. B. Bebb and E. W. Williams, in *Transport and Optical Phenomena*, edited by R. K. Willardson and A. C. Beer (Academic Press, New York, 1972), vol. 8 of *Semiconductors and Semimetals*, chap. 4, p. 181.

[45] R. H. M. Groeneveld and D. Grischkowsky, *J. Opt. Soc. Am. B* **11**, 2502 (1994).

[46] A. Othonos, *J. Appl. Phys.* **83**, 1789 (1998).

[47] H. C. Casey, Jr. and F. Stern, *J. Appl. Phys.* **47**, 631 (1976).

[48] C. H. Chen, M. Hargis, J. M. Woodall, M. R. Melloch, J. S. Reynolds, E. Yablonovitch, and W. Wang, *Appl. Phys. Lett.* **74**, 3140 (1999).

[49] H. B. Bebb and E. W. Williams, in *Transport and Optical Phenomena*, edited by R. K. Willardson and A. C. Beer (Academic Press, New York, 1972), vol. 8 of *Semiconductors and Semimetals*, chap. 4, p. 200ff.

[50] W. van Roosbroeck and W. Schockley, *Phys. Rev.* **94**, 1558 (1954).

[51] Y. Toyozawa, *Prog. Theor. Phys.* **20**, 53 (1958).

[52] J. S. Blakemore, *Semiconductor Statistics* (Pergamon Press, New York, 1962).

[53] M. G. A. Bernard and G. Duraffourg, *Phys. Status Solidi* **1**, 699 (1961).

[54] M. G. A. Bernard and G. Duraffourg, *J. Phys. Radium* **22**, 836 (1961).

[55] H. C. Casey, Jr. and M. B. Panish, *Heterostructure Lasers, Part A, Fundamental Principles* (Academic Press, San Francisco, 1978), p. 46 and 174ff, and references therein.

[56] D. A. B. Miller, personal communication.

[57] I. M. Catalano, A. Cingolani, M. Ferrara, and A. Minafra, *Physica Status Solidi B* **68**, 341 (1975).

[58] O. J. Glembocki and B. V. Shanabrook, in *Transport and Optical Phenomena*, edited by R. K. Willardson and A. C. Beer (Academic Press, New York, 1992), vol. 36 of *Semiconductors and Semimetals*, chap. 4, p. 221.

[59] M. Cardona, *Modulation Spectroscopy*, p. 219ff, in [60] (1969).

[60] M. Cardona, *Modulation Spectroscopy* (Academic Press, New York, 1969).

[61] B. O. Seraphin and R. B. Hess, *Phys. Rev. Lett.* **14**, 138 (1965).

[62] D. E. Aspnes and J. E. Rowe, *Phys. Rev. Lett* **27**, 188 (1971).

[63] D. E. Aspnes and J. E. Rowe, *Solid State Commun.* **8**, 1145 (1970).

[64] D. E. Aspnes, *Surf. Sci.* **37**, 418 (1973).

[65] H. Shen, P. Parayanthal, F. H. Pollak, M. Tomkiewicz, T. J. Drummond, and J. N. Schulman, *Appl. Phys. Lett.* **48**, 653 (1986).

[66] T. Mishima, M. Miura, S. Ozaki, and S. Adachi, *J. Appl. Phys.* **91**, 4904 (2002).

[67] H. Shen, S. H. Pan, F. H. Pollak, M. Dutta, and T. R. AuCoin, *Phys. Rev. B* **36**, 9384 (1987).

[68] D. S. Chemla, D. A. B. Miller, P. W. Smith, A. C. Gossard, and W. Wiegmann, *IEEE J. Quantum Electron.* **20**, 265 (1984).

[69] O. J. Glembocki and B. V. Shanabrook, *Superlattices and Microstructures* **3**, 235 (1987).

[70] B. V. Shanabrook, O. J. Glembocki, and W. T. Beard, *Phys. Rev. B* **35**, 2540 (1987).

[71] http://www.originlab.com.

[72] G. Kresse and J. Hafner, *Phys. Rev. B* **47**, 558 (1993).

[73] G. Kresse and J. Hafner, *Phys. Rev. B* **49**, 14251 (1994).

[74] G. Kresse and J. Furthmüller, *Comput. Mater. Sci.* **6**, 15 (1996).

[75] G. Kresse and J. Furthmüller, *Phys. Rev. B* **54**, 11169 (1996).

[76] W. Kohn and L. J. Sham, *Phys. Rev.* **140**, A1133 (1965).

[77] M. C. Payne, M. P. Teter, D. C. Allan, T. A. Arias, and J. D. Joannopoulos, *Rev. Mod. Phys.* **64**, 1045 (1992).

[78] D. Vanderbilt, *Phys. Rev. B* **41**, 7892 (1990).

[79] L. Hedin and B. I. Lundqvist, *J. Phys. C* **4**, 2064 (1971).

[80] D. Ceperley and B. Alder, *Phys. Rev. Lett.* **45**, 566 (1980).

[81] J. Perdew and A. Zunger, *Phys. Rev. B* **23**, 5048 (1981).

[82] E. D. Jones, N. A. Modine, A. A. Allerman, S. R. Kurtz, A. F. Wright, S. T. Tozer, and X. Wei, *Phys. Rev. B* **60**, 4430 (1999).

[83] H. J. Monkhorst and J. D. Pack, *Phys. Rev. B* **13**, 2339 (1976).

[84] A. K. Rappé, C. J. Casewit, K. S. Colwell, W. A. Goddard, and W. M. Skiff, *J. Amer. Chem. Soc.* **114**, 10024 (1992).

[85] C. J. Casewit, K. S. Colwell, and A. K. Rappé, *J. Am. Chem. Soc.* p. 10035 (1992).

[86] C. J. Casewit, K. S. Colwell, and A. K. Rappé, *J. Am. Chem. Soc.* **114**, 10046 (1992).

[87] A. K. Rappé, K. S. Colwell, and C. J. Casewit, *Inorg. Chem.* **32**, 3438 (1993).

[88] *The VASP Guide* (1999), URL `http://cms.mpi.univie.ac.at/vasp/`.

[89] http://www.webelements.com.

[90] O. Jepsen and O. K. Andersen, *Z. Phys. B* **97**, 35 (1995).

[91] C. G. Van de Walle and R. M. Martin, *Phys. Rev. B* **35**, 8154 (1987).

[92] R. Godby, M. Schluter, and L. Sham, *Phys. Rev. B* **37**, 10159 (1988).

[93] L. Fritsche and Y. M. Gu, *Phys. Rev. B* **48**, 4250 (1993).

[94] L. Fritsche, *Phys. Rev. B* **33**, 3976 (1986).

[95] V. I. Anisimov, J. Zaanen, and O. K. Andersen, *Phys. Rev. B* **44**, 943 (1991).

[96] V. I. Anisimov, I. V. Solovyev, M. A. Korotin, M. T. Czyzyk, and G. A. Sawatzky, *Phys. Rev. B* **48**, 16929 (1993).

[97] A. I. Liechtenstein, V. I. Anisimov, and J. Zaane, *Phys. Rev. B* **52**, R5467 (1995).

[98] S. L. Dudarev, G. A. Botton, S. Y. Savrasov, C. J. Humphreys, and A. P. Sutton, *Phys. Rev. B* **57**, 1505 (1998).

[99] D. Singh, *Planewaves, Pseudopotentials and the LAPW Method* (Kluwer Academic, Boston, 1994).

[100] C. Persson and A. Zunger, *Phys. Rev. B* **68**, 035212 (2003).

[101] Z. Pan, L. H. Li, Y. W. Lin, B. Q. Sun, D. S. Jiang, and W. K. Ge, *Appl. Phys. Lett.* **78**, 2217 (2001).

[102] M. Kondow, S. Fujisaki, S. Shirakata, T. Ikari, and T. Kitatani, in *International Symposium on Compound Semiconductors* (San Diego, CA, 2003), p. 76.

[103] C. Skierbiszewski, *Semicond. Sci. Technol.* **17**, 803 (2002).

[104] J. B. Heroux, X. Yang, and W. I. Wang, *J. Appl. Phys.* **92**, 4361 (2002).

[105] S. Kim, personal communication.

[106] J. Callaway, *Energy Band Theory*, p. 174, in [174] (1964).

[107] J. Callaway, *Energy Band Theory*, p. 31, in [174] (1964).

[108] W. Shan, W. Walukiewicz, J. W. Ager III, E. E. Haller, J. F. Geisz, D. J. Friedman, J. M. Olson, and S. R. Kurtz, *Phys. Rev. Lett.* **82**, 1221 (1999).

[109] A. Mascarenhas and Y. Zhang, *Curr. Opin. Solid. St. M.* **5**, 253 (2001).

[110] Y. Zhang, A. Mascarenhas, J. F. Geisz, H. P. Xin, and C. W. Tu, *Phys. Rev. B* **63**, 085205 (2001).

[111] H. Güning, L. Chen, T. Hartmann, P. J. Klar, W. Heimbrodt, F. Höhnsdorf, J. Koch, and W. Stolz, *Phys. Status Solidi B* **215**, 39 (1999).

[112] Y. Zhang, A. Mascarenhas, H. P. Xin, and C. W. Tu, *Phys. Rev. B* **61**, 7479 (2000).

[113] Y. Zhang and A. Mascarenhas, *Phys. Rev. B* **61**, 15562 (2000).

[114] P. R. C. Kent and A. Zunger, *Phys. Rev. Lett.* **86**, 2613 (2001).

[115] P. R. C. Kent and A. Zunger, *Phys. Rev. B* **64**, 115208 (2001).

[116] B. Silvi and A. Savin, *Nature* **371**, 683 (1994).

[117] B. K. Agrawal, P. S. Yadav, R. Srivastava, and S. Agrawal, *J. Phys.: Condens. Matter* **10**, 4597 (1998).

[118] K. Kim and A. Zunger, *Phys. Rev. Lett.* **86**, 2609 (2001).

[119] S.-H. Wei and A. Zunger, *Phys. Rev. Lett.* **76**, 664 (1996).

[120] S. Brennan, V. Lordi, and V. Gambin (2002), unpublished.

[121] W. D. Nix, *MSE353 Course Notes* (2001).

[122] Samples courtesy of K. Volz, W. Heimbrodt, F. Höhnsdorf, and W. Stolz, Philipps Universität Marburg, Germany.

[123] V. N. Strocov, P. O. Nilsson, T. Schmitt, A. Augustsson, L. Gridneva, D. Debowska-Nilsson, R. Claessen, A. Y. Egorov, V. M. Ustinov, and Z. I. Alferov, *Phys. Rev. B* **69**, 035206 (2004).

[124] H. Riechert, A. Ramakrishnan, and G. Steinle, *Semicond. Sci. Technol.* **17**, 892 (2002).

[125] D. A. B. Miller, D. S. Chemla, T. C. Damen, A. C. Gossard, W. Wiegmann, T. H. Wood, and C. A. Burrus, *Phys. Rev. B* **32**, 1043 (1985).

[126] Y. P. Varshni, *Physica (Amsterdam)* **34**, 149 (1967).

[127] M. A. Pinault and E. Tournie, *Appl. Phys. Lett.* **78**, 1562 (2001).

[128] A.Kaschner, T. Lüttgert, H. Born, A. Hoffman, A. Y. Egorov, and H. Riechert, *Appl. Phys. Lett.* **78**, 1391 (2001).

[129] J. Misciewicz, P. Sitarek, K. Ryczko, R. Kudrawiec, A. Fischer, M. Reinhardt, and A. Forchel, *Microelectron. J.* **34**, 737 (2003).

[130] S. R. Bank, M. A. Wistey, H. B. Yuen, V. Lordi, V. F. Gambin, and J. S. Harris, Jr. (2004), to be published.

[131] I. Vurgaftman, J. R. Meyer, and L. R. Ram-Mohan, *J. Appl. Phys.* **89**, 5815 (2001).

[132] M. A. Wistey, S. R. Bank, H. B. Yuen, and J. S. Harris (2004), submitted to *Appl. Phys. Lett.*

[133] S. R. Bank, M. A. Wistey, H. B. Yuen, V. Lordi, V. F. Gambin, and J. S. Harris, Jr. (2004), to be published in *J. Vac. Sci. Technol. B.*

[134] V. Lordi, H. Yuen, S. Bank, J. S. Harris, and S. Friedrich (2004), *Phys. Rev. B*, in publication.

[135] O. J. Glembocki and B. V. Shanabrook, in *Transport and Optical Phenomena*, edited by R. K. Willardson and A. C. Beer (Academic Press, New York, 1992), vol. 36 of *Semiconductors and Semimetals*, chap. 4, p. 251ff.

[136] V. Lordi, *TunnellingResonance$^{TM}$v2.1* software, unpublished (2000–2003).

[137] L. H. Li, V. Sallet, G. Patriarche, L. Largean, S. Bouchoule, K. Merghem, L. Travers, and J. C. Harmand, *Electron. Lett.* **39**, 519 (2003).

[138] K. Volz, V. Gambin, W. Ha, M. A. Wistey, H. B. Yuen, S. R. Bank, and J. S. Harris, *J. Cryst. Growth* **251**, 360 (2003).

[139] H. B. Yuen, personal communication.

[140] P. J. Klar, H. Grüning, J. Koch, S. Schäfer, K. Volz, W. Stolz, W. Heimbrodt, A. M. Kamal Saadi, A. Lindsay, and E. P. O'Reilly, *Phys. Rev. B* **64**, 121203(R) (2001).

[141] T. Kageyama, T. Miyamoto, S. Makino, F. Koyama, and K. Iga, *J. Cryst. Growth* **209**, 350 (2000).

[142] A. P. Young, L. J. Brillson, Y. Naoi, and C. W. Tu, *MRS Internet J. Nitride Sem. Res.* **5**, U679 (2000).

[143] M. A. Wistey, S. R. Bank, H. B. Yuen, H. Bae, and J. S. Harris, Jr. (2005), to be published in *J. Cryst. Growth*.

[144] M. A. Wistey, S. R. Bank, H. B. Yuen, and J. S. Harris (2004), submitted to *Appl. Phys. Lett.*

[145] S. Kurtz, J. Webb, L. Gedvilas, D. Friedman, J. Geisz, J. Olson, R. King, D. Joslin, and N. Karam, *Appl. Phys. Lett.* **78**, 748 (2001).

[146] P. Murugan and K. Ramachandran, *Diffus. Defect Data Pt. A Diffus. Forum* **171**, 61 (1999).

[147] J. F. Wager, *J. Appl. Phys.* **69**, 3022 (1991).

[148] M. Sugawara, T. Fujii, S. Yamazaki, and K. Nakajima, *Phys. Rev. B* **42**, 9587 (1990).

[149] Y. S. Jalili, P. N. Stavrinou, J. S. Roberts, and G. Parry, *Electron. Lett.* **38**, 343 (2002).

[150] I. Bar-Joseph, C. Klingshirn, D. A. B. Miller, D. S. Chemla, U. Koren, and B. I. Miller, *Appl. Phys. Lett.* **50**, 1010 (1987).

[151] T. Yakanaka, K. Wakita, and K. Yokoyama, *Appl. Phys. Lett.* **65**, 1540 (1994).

[152] N. C. Helman, J. E. Roth, D. P. Bour, and D. A. B. Miller, in *CLEO Spring 2004, San Francisco* (2004), cThH4.

[153] B. Pezeshki, Ph.D. thesis, Stanford Univ. (1991).

[154] M. Whitehead and G. Parry, *Electron. Lett.* **25**, 566 (1989).

[155] M. Whitehead, A. Rivers, G. Parry, J. S. Roberts, and C. Button, *Electron. Lett.* **25**, 984 (1989).

[156] R. H. Yan, R. J. Simes, and L. A. Coldren, *IEEE Photon. Technol. Lett.* **1**, 273 (1989).

[157] M. Whitehead, A. Rivers, G. Parry, and J. S. Roberts, *Electron. Lett.* **26**, 1588 (1990).

[158] B. Pezeshki, D. Thomas, and J. S. Harris, Jr., *Appl. Phys. Lett.* **58**, 813 (1991).

[159] B. Pezeshki, G. A. Williams, and J. S. Harris, Jr., *Appl. Phys. Lett.* **60**, 1061 (1992).

[160] J. A. Trezza, Ph.D. thesis, Stanford Univ. (1995).

[161] B. Pezeshki, D. Thomas, and J. S. Harris, Jr., *Appl. Phys. Lett.* **57**, 1491 (1990).

[162] S. Nojima and K. Wakita, *Appl. Phys. Lett.* **53**, 1958 (1988).

[163] R. K. Gug and W. E. Hagston, *Appl. Phys. Lett.* **74**, 254 (1999).

[164] K. Sato, I. Kotaka, W. Wakita, Y. Kondo, and M. Yamamoto, *Electron. Lett.* **29**, 1087 (1993).

[165] T. Jouhti, J. Konttinen, S. Karirinne, O. G. Okhotnikov, and M. Pessa, *IEE Proc.-Optoelectron.* **150**, 77 (2003).

[166] T. Sizer, II, T. K. Woodward, U. Keller, K. Sauer, T.-H. Chiu, D. L. Sivco, and A. Y. Cho, *IEEE J. Quantum Electron.* **30**, 399 (1994).

[167] A. M. Fox, D. A. B. Miller, G. Livescu, J. E. Cunningham, J. E. Henry, and W. Y. Jan, *Appl. Phys. Lett.* **57**, 2315 (1990).

[168] N. Streibl, K.-H. Brenner, and A. Huang, *Proc. IEEE* **77**, 1954 (1989).

[169] M. E. Prise, N. C. Craft, M. M. Downs, R. W. LaMarche, L. A. D'Asaro, L. M. F. Chirovsky, and M. J. Murdocca, *Appl. Opt.* **30**, 2287 (1991).

[170] F. B. McCormick, A. L. Lentine, R. L. Morrison, S. L. Walker, L. M. F. Chirovsky, and L. A. D'Asaro, *IEEE Photon. Technol. Lett.* **3**, 232 (1991).

[171] D. A. B. Miller, *Opt. Quant. Electr.* **22**, S61 (1990).

[172] F. J. Himpsel, *Adv. Phys.* **32**, 1 (1983).

[173] S. L. Chuang, *Phys. Rev. B* **43**, 9649 (1991).

[174] J. Callaway, *Energy Band Theory* (Academic Press, New York, 1964).